NANOSTRUCTURED VANADIUM OXIDES FOR ENERGY CONVERSION AND CONSERVATION

A Dissertation

by

KATE ELIZABETH PELCHER

Submitted to the Office of Graduate and Professional Studies of
Texas A&M University
in partial fulfillment of the requirements for the degree of

DOCTOR OF PHILOSOPHY

Chair of Committee,	Sarbajit Banerjee
Committee Members,	Marcetta Y. Darensbourg
	Janet Bluemel
	Jonathan Felts
Head of Department,	Simon North

December 2016

Major Subject: Chemistry

ABSTRACT

Increasing worldwide energy consumption has imposed strain on global natural resources. There are a number of sustainable approaches to meeting the energy needs, and many of them can be broadly classified into two main categories: energy conservation and energy conversion. Buildings consume a tremendous portion of the total energy used worldwide, and conserving some of this energy by using technological advancements, such as thermochromic films, holds promise for reducing energy footprints. There is also an urgent need to tap into renewable sources of energy. Solar energy, if harvested and stored appropriately, could easily meet the energy needs of the world's population. One route to solar energy conversion involves conversion of solar energy to chemical energy by splitting water to produce hydrogen and oxygen; hydrogen could then be stored and combusted to release the energy. Unfortunately, this has been a challenge for the scientific community since it requires the concerted transfer of four holes and four electrons.

In this work, we explore the use of vanadium oxides for both energy conservation and energy conversion applications. First, for energy conservation, vanadium dioxide (VO_2) has been explored for use within a dynamically switchable thermochromic thin film. VO_2 is able to block infrared light at high temperatures while allowing it to transmit at lower temperatures. Amorphous silica shells have been constituted around VO_2 nanowires using a modified Stöber method in order to embed

these films onto a glass matrix. By controlling particle size, it is possible to achieve significant modulation of near-infrared wavelengths of the electromagnetic spectrum.

Addressing energy conversion, a tunable platform has been developed with the intent of harvesting solar energy. Heterostructures linking CdSe/β-$Pb_xV_2O_5$ and CdS/β-$Pb_xV_2O_5$ have been synthesized through two different methods, linker-assisted assembly and successive ionic layer adsorption and reaction. Hard X-ray photoelectron spectroscopy and transient absorption spectroscopy studies show thermodynamic alignment of the energy levels and suggest hole transfer from the photoexcited semiconductor quantum dots to the mid-gap states of β-$Pb_xV_2O_5$. The CdS heterostructures show an improved alignment of their valence band with the mid-gap state of β-$Pb_xV_2O_5$. The tunable heterostructure platform holds promise for water splitting photocatalysts.

DEDICATION

This thesis is dedicated first to my parents, Dan and Sharon, who always believed I could do anything I wanted to and have supported me throughout my life. Also to my husband, Rob, and my dogs, Belle and Cobalt, whose unconditional love and support were vital to my success. Finally, to my friends and family, who are too many to name, who will never know how encouraging their love and support was; thank you.

ACKNOWLEDGEMENTS

First, I would like to thank my advisor, Prof. Sarbajit Banerjee, for the years of mentorship, patience, and teaching. His passion for his research is contagious and has caused my own passion to grow. He has given me multiple opportunities to travel and expand my skillsets and always had the utmost confidence in my performance. I am well prepared for my career and that is due to his leadership and encouragement.

I would also like to thank my committee members, Prof. Marcetta Y. Darensbourg, Prof. Janet Bluemel, and Prof. Jonathan Felts, for their guidance and support throughout the course of this research. Thank you to the office staff in the Chemistry department, especially Sandy Horton, who made my transfer easier.

Thanks also go to my friends, colleagues, and the department faculty and staff at the University at Buffalo where I was fortunate enough to study for the beginning of my graduate studies. The strong background I gained there brought about my success at Texas A&M University. I would especially like to thank Prof. David Watson and Dr. Chris Milleville who I collaborated with extensively and learned so much from.

To my undergrad Chemistry professor, Prof. Brian Vogt, without whom I would have never applied to graduate school, thank you for pushing me to be better.

Finally, to the Banerjee group members, past and present, for their support and insight, not only as researchers but as friends.

TABLE OF CONTENTS

Page

Page

LIST OF FIGURES

Page

Page

Page

Page

Page

Page

LIST OF TABLES

Page

CHAPTER I

INTRODUCTION*

Vanadium oxides constitute a versatile group of solid-state compounds, and are crystallized in a number of different structural motifs by dint of their variable oxidation states (ranging from +2 to +5) and different local coordination environments (tetrahedral, square pyramidal, octahedral).[1–3] Several V_xO_y frameworks constituted from vanadium-centered polyhedra accommodate a wide variety of intercalating species yielding ternary and more complex vanadium oxide bronzes that are often tolerant of a wide range of stoichiometries of the intercalating cations (Figure I. 1). The facile accessibility of different oxidation states and the ability to stabilize structures across broad compositional ranges make these systems particularly interesting for fundamental

---

* Part of the data reported in this chapter is reprinted with permission from "Transformers: The Changing Phases of Low-Dimensional Vanadium Oxide Bronzes" by P. M. Marley, G. A. Horrocks, K. E. Pelcher and S. Banerjee, *Chem. Commun.*, 2015, **51**, 5181–5198. Reproduced by permission of the Royal Society of Chemistry.
Part of the data reported in this chapter is reprinted with permission from "Distinctive Finite Size Effects on the Phase Diagram and Metal–Insulator Transitions of Tungsten-Doped Vanadium(iv) Oxide" by L. Whittaker, T.-L. Wu, C. J. Patridge, G. Sambandamurthy and S. Banerjee, *J. Mater. Chem.*, 2011, **21**, 5580. Reproduced by permission of the Royal Society of Chemistry.
Part of the data reported in this chapter is adapted with permission from "Charge Disproportionation and Voltage-Induced Metal–Insulator Transitions Evidenced in β-$Pb_xV_2O_5$ Nanowires" by P. M. Marley, A. A. Stabile, C. P. Kwan, S. Singh, P. Zhang, G. Sambandamurthy and S. Banerjee, *Adv. Funct. Mater.*, 2013, **23**, 153–160. Copyright 2013 Wiley Periodicals, Inc.
Part of the data reported in this chapter is adapted with permission from "Electron Lone Pair Distortion Facilitated Metal-Insulator Transition in β-$Pb_{0.33}V_2O_5$ Nanowires" by L. Wangoh, P. M. Marley, N. F. Quackenbush, S. Sallis, D. A. Fischer, J. C. Woicik, S. Banerjee and L. F. J. Piper, *Appl. Phys. Lett.*, 2014, **104**, 182108. with the permission of AIP Publishing.

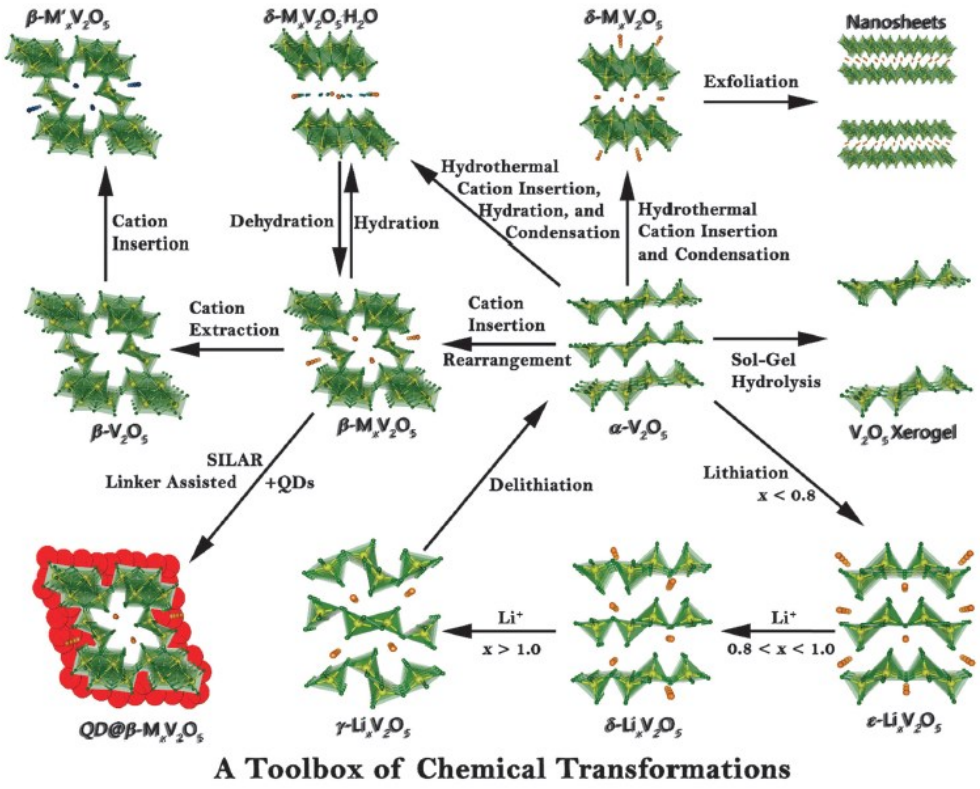

Figure I. 1 Intercalation-induced phase transitions, structural rearrangements, and low-temperature routes to modify the structure of ternary vanadium oxide bronzes.[3]

explorations of structure—property—function correlations, especially given the importance of electron—electron correlations in these compounds. The interest in vanadium oxides is not purely intellectual; the distinctive electronic and optical properties of these compounds, make them relevant for real-world applications, such as for catalysis, electronics, energy storage, and bolometry.[4–11] This work will focus on the study and design of two specific sets of compounds: the binary vanadium dioxide VO_2 and the ternary vanadium oxide bronze β-$Pb_xV_2O_5$. The potential applications of these compounds for energy conservation and conversion is explored.

Vanadium dioxide, VO_2, was discovered in 1959 by Morin and, since that discovery, has been extensively studied due to its remarkable characteristic reversible thermally driven insulator—metal transition.[12] This first-order solid—solid metal—insulator transition is most well-known for the accompanying orders-of-magnitude change in optical transmittance and electrical conductivity. Indeed, the change in electrical conductivity accompanying the insulator—metal transition can approach five orders of magnitude and is unparalleled in solid state chemistry.[10,13–16] Amongst the legion of materials exhibiting metal—insulator transitions, VO_2 occupies a special place since the metal-to-insulator transition occurs in close proximity to room temperature for the bulk material (at ca. 68°C).[13,16–18] A monoclinic to tetragonal structural transition is often considered to be the basis for the electronic phase transition; however, significant research has been devoted to determining if the transition is fundamentally a Peierls' transition driven by electron—phonon coupling or a Mott—Hubbard transition underpinned by electron—electron correlations.[14,15,19–21] When considering the structural transformation, the phase transition converts VO_2 from a low-temperature insulating monoclinic phase (M1, $P2_1/c$) to a high-temperature tetragonal rutile phase (*R*, $P4_2/mnm$) (Figure I. 2A, B).[13] In the monoclinic phase, the V—V bond lengths alternate with short and long bonds that are 2.65 and 3.13Å, respectively, along the *c* axis; this structural motif is thus characterized by "dimerization" of the adjacent vanadium cations. During the structural transition, these dimers transform to a uniform V—V bond length of 2.85Å, resulting in an increase in symmetry and a reduction of the unit cell parameter by one-half (Figure I. 2A, B).[22] Additionally, the dimerization in the M1 phase causes the

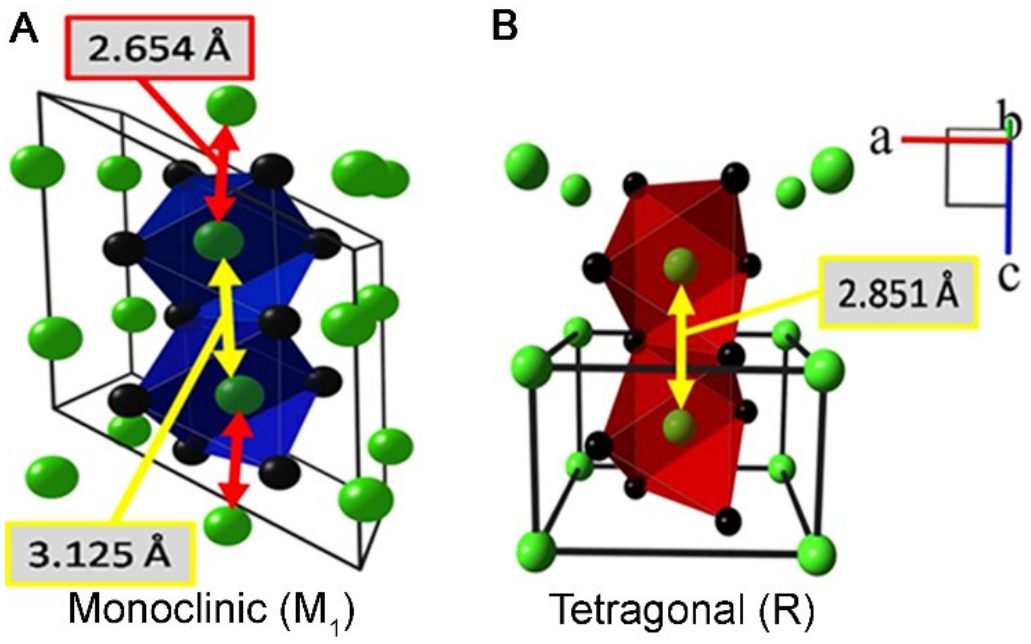

Figure I. 2 A) Low-temperature monoclinic phase of VO_2; B) High-temperature tetragonal phase of VO_2.[23]

V—V chains to form a zigzag configuration that is canted along the *c*-axis, whereas the V—V chains in the R phase are arrayed along a linear geometry.[13] The slightly distorted monoclinic phase possesses states derived from V d orbitals that are split, causing a bandgap of 0.5—0.6 eV to open up at the Fermi level; in contrast, the rutile phase has no bandgap.[13] As expected, the first-order transition, though entirely reversible upon application and removal of external stimuli, has a marked hysteresis. Years of research has brought about general agreement that both electron—phonon and electron—electron correlations contribute to the transition,[16,19,21] though the exact roles of electron-phonon coupling and electron correlations is yet to be conclusively revealed.[13,14,19–21,23]

Despite the mechanistic origin of the phase transition of VO_2 remaining unknown, the switchability of the MIT permits the use of this material in several

applications including thermochromic films, ultra-fast switches, transistors, and optical modulators.[24–29] As mentioned earlier, the crystal structure change is accompanied by a pronounced change of IR reflectivity. Below the bulk transition temperature of 68°C, infrared light passes through the material since VO_2 has a bandgap of ca. 0.6 eV in the low-temperature phase.[26] As VO_2 transforms to the high-temperature rutile phase (on a timescale quicker than 300 fs), the bandgap closes and the material becomes reflective to infrared light as a result of massive increase in carrier density.[30]

The heating of the interiors of buildings, oftentimes called solar heat gain, occurs principally due to the infrared wavelengths of the solar spectrum.[26] The metallic high-temperature phase of VO_2 thus could prevent the heating of interiors at high ambient temperatures; however upon cooling, incident solar radiation could be harnessed to heat interiors at lower ambient temperatures when the VO_2 is transformed to the insulating phase.[28] Figure I. 3 illustrates the operation of a thermoresponsive "smart window", which is equipped with the ability to block transmission of infrared radiation at high

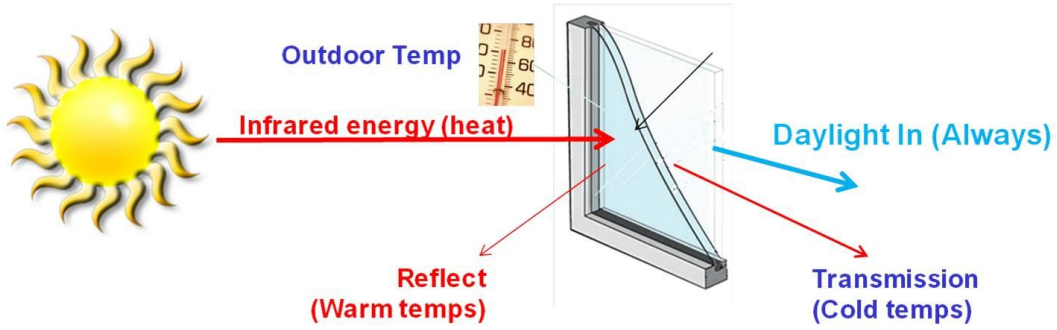

Figure I. 3 Schematic of a "smart" window.

temperatures while allowing transmission of infrared light at low temperatures, all while maintaining transparency in the visible region of the electromagnetic spectrum.

Though these interesting properties of VO_2 have been well-known for over 50 years, practical device application has been stunted due to the high transition temperature as well as cracking that frequently occurs upon thermal cycling. Previous studies have shown that the temperature of the phase transition of VO_2 can be controlled over a substantial temperature range by scaling to nanoscale dimensions and through substitutional doping.[13,22,28] Indeed, an adequate degree of control of the phase transition temperature has been established such that individual formulations for deployment of thermochromic films in a multitude of climate zones is thought to be feasible. For bulk or vapor-deposited thin films, the issue of cracking as they cycle through the MIT arises from the structural change between the two phases of VO_2. The unit cell diminishes by one-half as the crystal structure changes from monoclinic to rutile, and then increases by the same amount in the reverse transition. The substantial inhomogeneous strain resulting from this volume change thus results in crack formation and delamination in single-crystalline films. In contrast, upon nanostructuring, VO_2 is able to relax the mechanical strain through deformation instead of delamination, allowing the material to be cycled thousands of times without fracture or pulverization. Some films have been grown *via* the high-temperature methods discussed previously, but form nanostructured polycrystalline films rather than single-crystalline films.[31,32] These films show promise but the high-temperature methods used are not desirable. Furthermore, physical vapor deposition does not permit for control over grain size. As an alternative approach,

thermochromic films can be prepared by embedding nanocrystals within a softer polymeric matrix wherein the strains accompanying structural deformation can be better accommodated. Freestanding powders of nanostructured VO_2 can be grown *via* low-temperature hydrothermal methods.[18] The solution processability of the high-purity freestanding powders produced hydrothermally allows for significant versatility in the coating method used, ranging from spray coating to roller applications and further allows for the scalability required for high-volume deployment.

In this dissertation, we seek to address two remaining materials problems that are impediments to the integration of the VO_2 nanowires within functional thermochromic coatings. First, increased chemical and thermal stability is desirable for the coating materials since they can readily be oxidized to V_2O_5, which represents somewhat of a thermodynamic sink in the binary V—O system. Although, most envisioned glazing applications would place the VO_2 nanowire coatings on the interior surface of double-paned insulating glass units, increased chemical and thermal stability would help make these materials consonant with the stringent 20 year warranties offered by most insulating glass unit manufacturers. A second problem is that as-prepared VO_2 nanowires do not adhere well to glass surfaces. Consequently, for lasting adhesion to glass panes, the surfaces of the nanowires need to be appropriately modified. Chapter II discusses the growth of amorphous silica shells on VO_2 nanowires, which protects the wires from oxidation and allows them to adhere to glass substrates. The silica shells on the VO_2 nanowires have been characterized by scanning electron microscopy (SEM) and transmission electron microscopy (TEM) before and after annealing. Differential

scanning calorimetry (DSC) and Raman experiments are further used to demonstrate that the silica coating does not change the transition temperature of the nanowires, and indeed suggest that the coatings protect the nanowires from oxidation. This coating method has further been used to prepare a composite coating of the VO_2@SiO_2 nanowires on the surfaces of glass substrates.

Addressing mechanical integrity and ensuring thermal stability of the VO_2 films is of course only one piece of the puzzle, as the films must first and foremost demonstrate excellent thermochromic modulation. In the case of nanostructured composite films, the size, morphology, and dispersion of the nanoparticles has a great effect on the extent of infrared modulation. Calculations have shown that such films could achieve as much as a 50% decrease of transmission in the infrared region of the electromagnetic spectrum.[33] Chapter III endeavors to understand the effects of particle size by investigating four different sizes of VO_2 nanostructures (coated with a SiO_2 shell) and their infrared modulation in polymer composite films. The as-synthesized nanoparticles have been characterized by TEM and the composite films have been studied through IR spectroscopy to elucidate finite size effects on the modulation of transmission in the infrared region and the transmission of visible light. This chapter describes viable thermochromic films constituted from 10±4 nm VO_2@SiO_2 nanocrystals embedded within an acrylate matrix.

The second half of this work, which focuses on ternary vanadium oxide bronzes, came to fruition as a means of attempting to solve one of the most vexing challenges with solar energy conversion. Based on the trends of population and economic growth,

sustainable energy production has emerged as an urgent imperative.[34] Only solar and nuclear energy can meet the long-term energy requirements of the global population without bringing about catastrophic climate change.[35–39] Given the safety ramifications of the latter, harnessing solar energy has become a necessity. However, two major problems need to be addressed to ensure an increased role for solar energy conversion in meeting the earth's energy needs: harvesting the energy and storing the harvested energy. Many materials have been developed that can efficaciously harvest solar energy, although improvements in photon conversion efficiencies remain much sought after, especially for cost-effective photovoltaic constructs such as dye-sensitized and bulk heterojunction solar cells.[36,40] Given the intermittent nature of solar energy, developing viable storage options has proven to be extremely necessary, but is a more difficult challenge. Water splitting, or the disproportionation of H_2O into H_2 and O_2, represents one of the most promising strategies for production of solar fuels that can subsequently be stored and then combusted to generate energy.[41–43]

Though arguably the most promising strategy, water-splitting is extremely challenging due to the necessity of the concerted transfer of four electrons and four protons:

$$4H^+ + 4e^- \rightarrow 2H_2 \qquad E°_R(H^+/H_2) = 0 \text{ V vs. NHE} \qquad \text{(I.1)}$$

$$2H_2O \rightarrow O_2 + 4H^+ + 4e^- \qquad E°_R(O_2/H_2O) = +1.23 \text{ V vs. NHE} \qquad \text{(I.2)}$$

There is an urgent need to design viable photocatalysts, which can facilitate *all* the following processes: (1) absorption of visible/near-IR light to yield electrons at

potentials more negative than $E°_R(H^+/H_2)$ and holes at potentials more positive than $E°_R(O_2/H_2O)$, (2) separation of photogenerated electrons and holes and accumulation at catalytic sites, (3) generation *and* separation of H_2 and O_2, and (4) transport of four equivalents of H^+ from the oxidation half to the reduction site.[44] It seems increasingly unlikely that a single material or molecule will be able to meet all these stringent requirements. Consequently, a promising strategy is to develop hybrid modular platforms wherein different components perform the various functions required to split water, akin to natural photosynthetic systems.[36,43] Semiconductor-based photoelectrochemical cells (PECs) and dispersed photocatalysts have been studied for decades; however, real-world water-splitting applications have been stunted by poor light harvesting, inefficient redox catalysis, criticality and low abundance of constituent elements, long-term instability, and high cost.[37,45]

The potential of the water-oxidation half reaction is so high that semiconductors used must have a wide-bandgap, which normally results in poor harvesting of visible light. The need for semiconductors that can deliver photogenerated holes at potentials only minimally positive of the water-oxidation potential has become increasingly evident in recent years and is the primary focus of the second part of the dissertation. Chapters IV—VI of this dissertation describe the synthesis, structural characterization, and electronic structure of heterostructures interfacing β-$M_xV_2O_5$ nanowires characterized by mid-gap states that lie between valence and conduction band edges) with II-VI semiconductor quantum dots wherein the bandgaps are amenable to tuning as a function of composition and dimensional confinement (below the Böhr radius).[46,47]

Figure I. 4 depicts a flowchart representing the experimental design and iterative integration of synthesis, measurement, and modeling used to fabricate these tunable heterostructures. Namely, density functional theory calculations in conjunction with experimental studies of the electronic structure of several ternary vanadium oxide bronzes has provided initial indications of structures that are stable and have characteristic mid-gap states that can be utilized for hole transfer.[48,49] Subsequently, a library of quantum dots has been examined to determine which combination of β-$M_xV_2O_5$ and quantum dots will allow for the optimal alignment necessary to drive hole

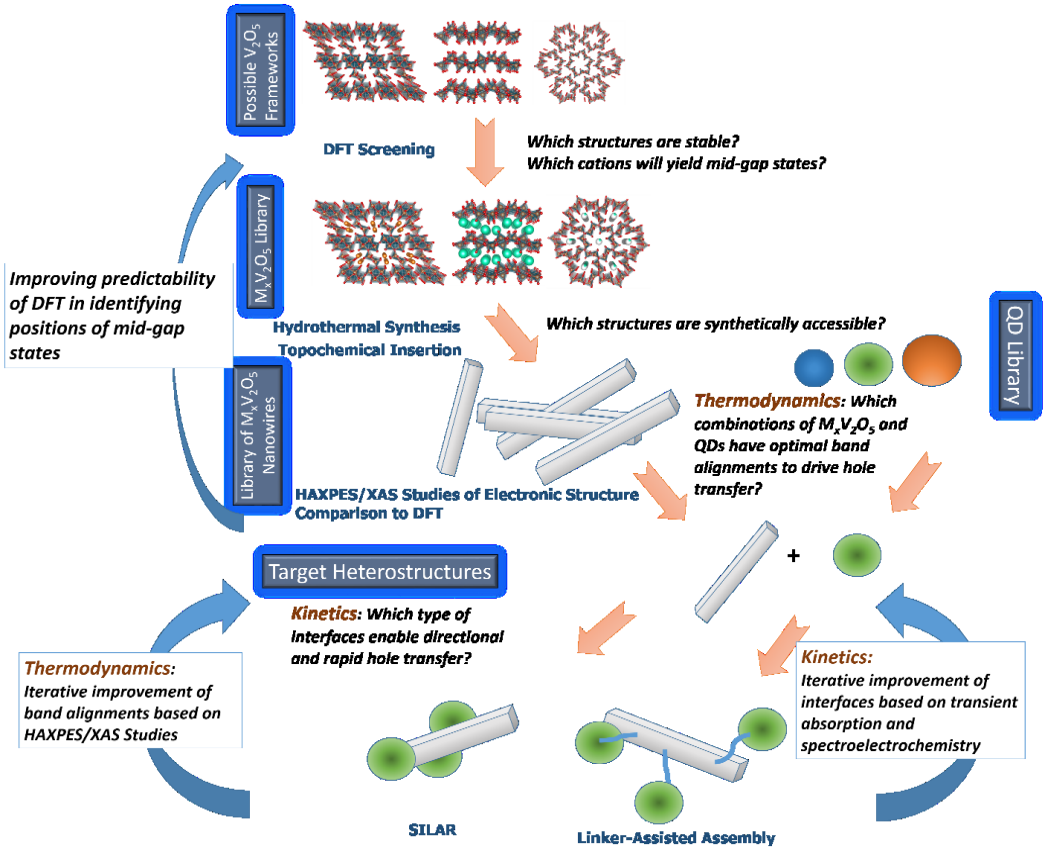

Figure I. 4 Flowchart illustrating our approach for the rational design of the QD/β-$M_xV_2O_5$ heterostructures.

transfer. Lastly, a first generation of heterostructures has been synthesized and thermodynamic alignment of energetic offsets and kinetics of hole transfer have been systematically examined using spectroscopic methods. A next generation of catalysts with improved energetic offsets have been devised based on the mechanistic understanding obtained from spectroscopic studies of first-generation CdSe/β-$Pb_{0.33}V_2O_5$ quantum dot structures.

Ternary vanadium oxide bronzes with the formulation $M_xV_2O_5$, (M: main group or transition metal cations; *x* represents the stoichiometry, which is variable based on the specific cation and the crystal structure), are a versatile set of compounds with properties tunable as a function of the size, charge, and polarizability of the intercalated cation (Figure I. 1).[6,48,50–56] To fully understand the crystal structure of these bronzes, we first consider the layered crystal structure of the parent compound V_2O_5, which adopts an orthorhombic open framework based on the edge-sharing of layers of VO_5 square pyramids (Figure I. 1).[1,57] This open framework can incorporate varying amounts of interstitial cations between the layers, although intercalation of specific cations can profoundly alter the structure of the V_2O_5 framework by inducing transformations to two-dimensional double-layered δ or one-dimensional tunnel-like β geometries.[1,56,58] These frameworks can accommodate a large range of cation stoichiometries and contain the cations either ordered along quasi 1D-tunnels or layered between 2D sheets of the V_2O_5 parent framework. A partial reduction of the framework vanadium atoms is induced through the ordered cations and the resulting charge ordering motifs are specific to the specific cation M and the stoichiometry *x*. To maintain charge neutrality, the

intercalation of cations inevitably results in partial reduction of a fraction of the V^{5+} sites to V^{4+}.[51,56,59,60] Carrier transport is then confined through the tunnel or sheet frameworks due to the structural anisotropy. In the low concentration limit, charge transport occurs

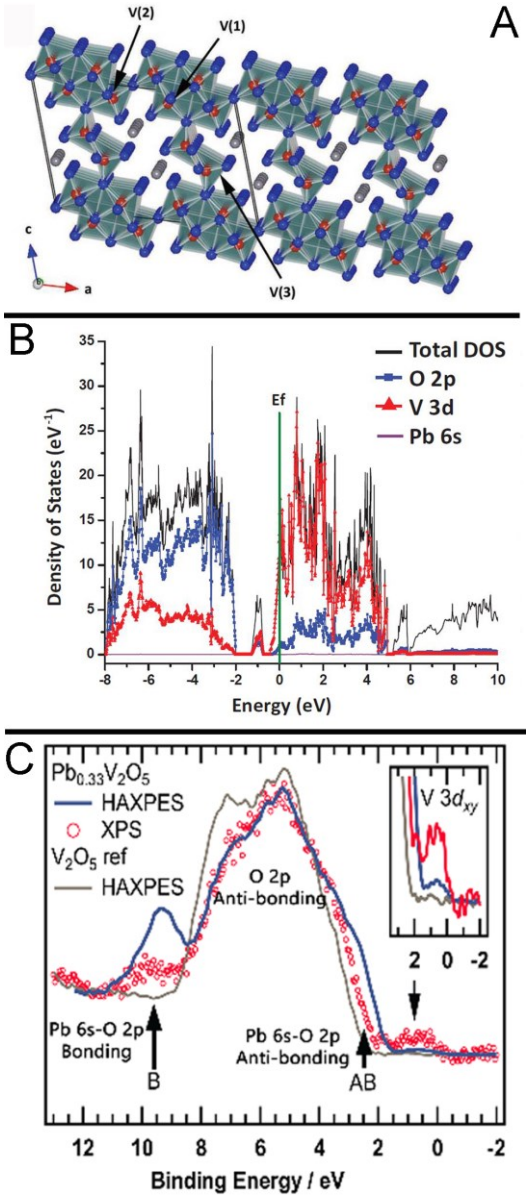

Figure I. 5 A) Crystal structure of β-$Pb_{0.33}V_2O_5$; B) Density of states derived from first principles calculations of β-$Pb_{0.33}V_2O_5$, and C) HAXPES results comparing the valence bands of β-$Pb_{0.33}V_2O_5$ and V_2O_5.[48,49]

via small polaron hopping but with increasing concentration of cations charge delocalization and metallization is observed.

In Wadsley-type bronzes, interstitial cations reside within a tunnel constituted by three crystallographically unique vanadium atoms and their oxygen-coordinated polyhedra.[61] Smaller cations such as Li^+ and Cu^+ give rise to a β' crystal structure, whereas larger cations occupy a separate set of larger interstitial sites to yield the β phase.[54,62] Figure I. 5A depicts the crystal structure of β-$Pb_xV_2O_5$, illustrating the tunnel sites occupied by Pb^{2+} cations, showing the location of the steroactive Pb $6s^2$ lone pairs, which induce a pronounced distortion of the tunnel; the tunnel is constituted from two interlinked [VO_6] octahedra and one [VO_5] square pyramid in each unit cell.[48]

In recent work, we have developed a hydrothermal synthetic route to stabilize phase-pure β-$M_xV_2O_5$ nanowires (NW) with precise ordering of cations in interstitial sites.[48,50,54] Confining a material to nanoscale dimensions provides an opportunity for "self-healing" of structural imperfections since defects incorporated during growth can readily be eliminated upon migration to nearby surfaces, thereby providing access to very high crystal quality material with careful control of stoichiometry and cation **o**rdering.[48,60] Density of states calculations of β-$Pb_{0.33}V_2O_5$ (Figure I. 5B) indicates the presence of a mid-gap state between the valence and conduction bands, which is derived from the hybridization of Pb 6s and O 2p states.[48] These calculations represent the first step in the flowchart shown in Figure I. 4. In the following step, confirmation of the existence of a mid-gap state has been obtained from hard X-ray photoelectron spectroscopy (HAXPES) measurements of these NWs (Figure I. 5C). These

measurements, which probe the bulk electronic structure, and were performed at the National Synchrotron Light Source reveal that the state derives from anti-bonding Pb 6s-O 2p interactions.[49] Most interestingly, the location of the mid-gap states of β-$Pb_{0.33}V_2O_5$ suggests that they are optimally aligned for hole transfer to the oxidation potential of water.[43,48] This energy range does not have a lot of accessible states and as such makes β-$Pb_{0.33}V_2O_5$ a viable choice for water-splitting applications. The ability to change the M cation in these ternary vanadium oxide bronzes indicates a modular platform where mid-gap states can be systematically changed as a function of cation composition and stoichiometry. In addition, because these mid-gap states do not arise from defects,[63] but rather through interstitial doping, there is a uniformity of the electronic structure throughout the nanowires.

While the mid-gap states of β-$Pb_{0.33}V_2O_5$ are ideal for hole transfer to water oxidation catalysts, the NWs are poor light harvesters. Arguably the most well-known light harvesters are quantum dots (QDs), intermediate gap semiconductors such as II-VI chalcogenides, which are commonly used in photochemical and electrochemical reactions.[64–66] These photocatalytic materials offer high molar absorptivity in the visible spectrum and have been extensively explored for construction of hybrid photovoltaic architectures.[67] Nanocrystalline forms of the semiconductors have been intensely studied in recent decades since their band gaps, redox potentials, and absorption spectra can all be tuned by controlling a single parameter: the size of the semiconductor nanocrystals.[68–70] The tunability of electronic characteristics such as the bandgap and the relative energy positioning of the valence and conduction bands makes II-VI nanocrystalline

semiconductors ideal for interfacing with β-$M_xV_2O_5$ nanowires to explore a reconfigurable platform for photocatalysis.

Chapter IV describes first generation heterostructures wherein the light-harvesting components are CdSe QDs; these were selected as the initial starting point in the design of heterostructures owing to their ability to absorb visible light, the placement of their valence band-edge edges that should facilitate hole transfer to β-$Pb_{0.33}V_2O_5$ mid-gap states, and their facile accessibility by multiple synthetic routes.[65,66] Figure I. 6 depicts the desired energy alignments that we hope to exploit in our heterostructured platform. In the proposed cascade of charge transfer reactions, CdSe QDs will harvest visible light resulting in the excitation of an electron from the valence band to the conduction band. The hole created at the conduction band will be injected to the

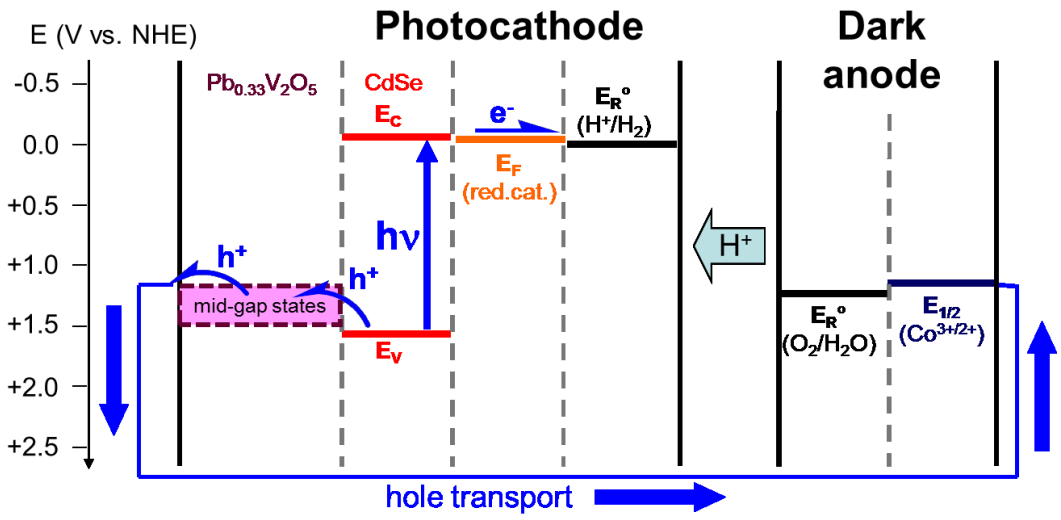

Figure I. 6 Schematic depicting the desired design of the photoelectrochemical cell consisting of β-$Pb_{0.33}V_2O_5$ and CdSe**.**

optimally positioned (occupied) mid-gap states of β-$Pb_{0.33}V_2O_5$ wherein they can be propagated and delivered to a dark photocatalyst (such as a Co^{3+}/Co^{2+} catalyst) at a potential only slightly more positive than the water oxidation catalyst.[37,41,44,71] Water will be oxidized as per Equation I.2 to generate molecular oxygen and protons. The electrons excited to the conduction band of CdSe quantum dots will further be delivered to a reduction catalyst (such as Pt) at an appropriate potential to reduce protons generated in the oxidation half-reaction to molecular hydrogen as per Equation I.1. In order to form an efficacious photocatalytic heterostructure, the nature of the interface between the β-$M_{0.33}V_2O_5$ nanowires and II-VI semiconductor nanocrystals is of paramount importance. Consequently, Chapter IV discusses a scalable solution-based synthetic route based on the successive ionic layer adsorption and reaction (SILAR) method. This approach, a variation of chemical bath deposition techniques,[72–74] requires the immersion of a substrate within the desired cation solution followed by immersion into anion solutions in order to form a thin film. SILAR techniques have found widespread applicability for the deposition of nanocrystalline semiconductors on thin film substrates and have further been elaborated to obtain doped quantum dots and core—shell structures.[75] In addition, linker-assisted assembly (LAA), where bifunctional ligands tether the QDs to the nanowires have also been examined. Two different synthetic routes have been explored since the interface between two semiconductors can profoundly alter the kinetics of charge transfer, especially when considering nanomaterials, where the surface-to-volume ratios are much higher than for bulk materials.[39]

While the thermodynamic band alignments depicted in Figure I. 6 are necessary for the desired charge transfer cascade, they are not in themselves sufficient. The kinetics of charge transfer essentially determine whether an interfacial structure can serve as a viable component of a photoelectrochemical cell. Figure I. 7 depicts the possible charge transfer pathways for the proposed QD/$M_xV_2O_5$ heterostructures each of which will have its distinct rate constant. Steps A-E show the desired pathways where an electron is excited to the conduction band of the QD after absorbing light (A); next, the remaining hole is then transferred to the mid-gap state of the nanowire (B). Following this transfer, the hole is then used to oxidize water to O_2 and $4H^+$ (C). Meanwhile, the generated electron transfers to a hydrogen evolution catalyst (D) and reduces H^+ (aq.) to H_2 (E). There are several competing pathways that could prevent these desired charge transfer reactions and these are depicted schematically as 1-5 in Figure I. 7. Simple recombination of the electron—hole pair immediately after photoexcitation (1), transfer of the photogenerated electron from the conduction band edge of the QD to the mid-gap state of the nanowire (2), transfer of the electron from the catalyst to the valence band of the QD (3) or the mid-gap state (4), and finally, transfer of the electron from the conduction band of the QD to the conduction band of the nanowire (5) are all alternative

deleterious pathways. Transient absorption spectroscopy has been utilized to study the dynamics of excited state charge transfer in the synthesized CdSe/β-$Pb_{0.33}V_2O_5$ heterostructures and is discussed in Chapter V. Based on HAXPES examination of the energetic offsets and transient absorption spectroscopy studies of the dynamics of interfacial charge transfer, the valence band edge of CdSe QDs was measured to lie ca. 0.7 eV higher in energy than the highest-energy mid-gap states of β-$Pb_{0.33}V_2O_5$ nanowires.

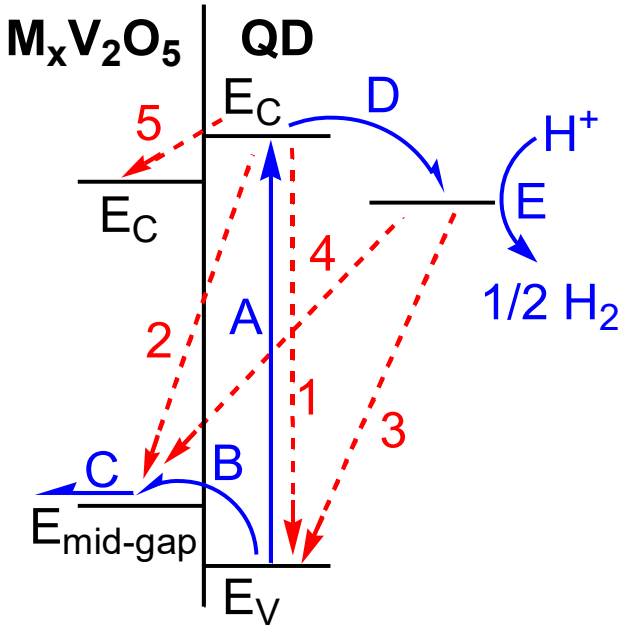

Figure I. 7 Possible charge transfer pathways in the synthesized heterostructures. The solid blue arrows represent desired pathways while the red dashed arrows show competing undesirable pathways.

Consequently, second-generation catalysts were designed based on another iteration of the tunable platform (Figure I. 4) exemplified through CdSe/ β-$Pb_{0.33}V_2O_5$. Chapter VI describes CdS/ β-$Pb_{0.33}V_2O_5$ heterostructures that were synthesized and studied using XPS, which indicated the shifting of the valence band to more positive energies, i.e., closer to the mid-gap state of β-$Pb_{0.33}V_2O_5$. A ca. 0.40 eV decrease in the thermodynamic barrier for hole injection has been realized in these structures.

CHAPTER II

SILICA-SHELL ENCAPSULATION AND ADHESION OF VO_2 NANOWIRES TO GLASS SUBSTRATES: INTEGRATING SOLUTION-DERIVED VO_2 NANOWIRES WITHIN THERMALLY RESPONSIVE COATINGS*

II.1 Introduction

The dramatic first-order solid—solid metal—insulator transition of the binary vanadium oxide VO_2 has few parallels in solid state chemistry and is most famously characterized by an abrupt change in optical transmittance and electrical conductivity that can span five orders of magnitude.[10,13–18] A structural transition is often seen to underpin the electronic phase transition although substantial controversy still rages regarding the Peierl's versus Mott—Hubbard mechanistic origin of the transition.[14,15,19–21] In essence, the first-order structural phase transition transforms the material from a tetragonal rutile (R, $P4_2/mnm$) phase stable at high temperatures to a low-temperature monoclinic (M1, $P2_1/c$) phase.[76] During this structural transition, the uniform V—V bond length of 2.85Å along the crystallographic *c* axis is altered to create alternating short and long bond distances of 2.65 and 3.13Å, respectively, which can be viewed as "dimerization" of adjacent vanadium cations and results in doubling of the unit cell

*Reprinted with permission from "Silica-Shell Encapsulation and Adhesion of VO_2 Nanowires to Glass Substrates: Integrating Solution Derived VO_2 Nanowires within Thermally Responsive Coatings" by K. E. Pelcher, M. R. Crawley and S. Banerjee, *Mater. Res. Express*, 2014, **1**, 035014.

parameter.[22] In addition, the alternating V—V chains adopt a zigzag configuration in the M1 phase that is substantially canted from the linear geometry of the V—V chains in the rutile phase.[13] The phase transition is entirely reversible upon heating albeit with a pronounced hysteresis as expected for a first-order phase transition. While the precise roles of electron-phonon coupling and strong electronic correlations remains to be conclusively elucidated,[13,14,19–21] the emerging consensus in the discipline appears to support a role for both driving forces.[13,16,19]

Regardless of the precise mechanistic origin of the phase transition, the dramatic temperature-induced switchability of the optical transmittance of VO_2 lends itself to useful practical applications such as in dynamically switchable thermochromic spectral mirrors.[26–29] Below 67°C, VO_2 has a bandgap of ca. 0.8 eV and is transparent to infrared light. Above this temperature, it transforms on a timescale quicker than 300 fs to a metallic phase and reflects infrared light, thereby serving as a heat mirror.[13,30] While the "chameleon-like" dynamically switchable properties of VO_2 have long been known, practical device implementation has been hindered by the high switching temperature and the tendency of the material to crack upon cycling. In recent work, we have demonstrated substantial control over the phase diagram of VO_2 between -19 and 68°C through scaling to nanoscale dimensions and the introduction of dopant species.[13,18,23,77–79] From the perspective of dynamically switchable mirrors, this implies that distinctive formulations can be identified and implemented for specific technological applications. Also, unlike in the bulk, VO_2 nanostructures can be cycled thousands of times without degradation in properties (cracking or fracture) due to the facile relaxation of mechanical

strain as a result of the finite size of the materials. Finally, the materials prepared by our synthetic route are available as free-standing solution-dispersible high-purity powders, allowing them to be coated by a variety of standard glass-coating methods such as spray coating, powder coating, and roller application.

In this article, we seek to demonstrate the adhesion of VO_2 nanowires to glass surfaces mediated by a silica matrix and further explore the dynamic spectral switching of the coated glass substrates. Synthetic routes have been developed both for growing discrete SiO_2 shells encapsulating the VO_2 nanowires as well as for embedding VO_2 nanowires in a SiO_2 matrix bonded to glass. The core-shell nanostructures as well as the integrated coatings have been characterized by electron microscopy. Differential scanning calorimetry (DSC) and Raman spectroscopy have been further used to demonstrate that the silica coating does not change the transition temperature of the nanowires. The SiO_2 shell/matrix is observed to enhance the thermal stability of the VO_2 nanowires towards oxidation in addition to facilitating excellent adhesion to glass. The thermally induced dynamic switching of the near-infrared transmittance of the coatings is also examined.

II.2 Experimental

II.2.1 Synthesis of VO_2 Nanowires

VO_2 nanowires were synthesized using a stepwise hydrothermal approach. First, hydrated V_3O_7 nanowires were synthesized by the hydrothermal reduction of V_2O_5 by oxalic acid. This reaction was performed at 210°C in a Teflon-lined acid digestion vessel

(Parr). Briefly, 300 mg of bulk V_2O_5 (Sigma-Aldrich) and 75 mg of oxalic acid (J.T. Baker) were mixed with 16 mL of water, sealed within an autoclave, and allowed to react for 72 h. The reaction was stopped at 24 h intervals and the reactants were mechanically agitated. In the next step, VO_2 nanowires were formed by the low-pressure solvothermal reduction of V_3O_7 nanowires using a 1:1 mixture of 2-propanol and water. This reaction was also performed in a Teflon-lined acid digestion vessel at 210°C. The collected powder was washed with copious amounts of water and annealed under argon at 450°C for at least 1 h.

II.2.2 Silica Coating of VO_2 Nanowires

A modified Stöber Method was used to coat the VO_2 nanowires with an amorphous silica shell. Ethanol and DI water were used as solvents. Tetraethylorthosilicate (TEOS, Alfa Aesar) and NH_4OH (28%-30%, JT Baker) were used as received. In a typical reaction, 24 mg of VO_2 nanowires were ultrasonicated in a solution of 32 mL of ethanol and 8 mL of water. After 5 min, 400 µL of NH_4OH solution was added dropwise to this dispersion. NH_4OH acts as a catalyst and maintains the hydroxide concentration in solution.[80] After ca. 10 min, 200 µL of TEOS was added dropwise to the solution. The solution was then allowed to react for different periods of time to control the shell thickness. To terminate the reaction, the solution was centrifuged and the collected powder was washed, redispersed in ethanol, and then centrifuged again to collect the powder. A total of 4-6 centrifugation cycles were performed for each sample. The collected powder was allowed to dry under ambient conditions and annealed under appropriate ambients to evaluate thermal stability.

II.2.3 Adhering VO_2 Nanowires onto Glass Substrates

Glass slides were cleaned with a piranha solution (150 mL concentrated H_2SO_4 in water and 50 mL of 30% aqueous solution of H_2O_2) for 12-24 h and then washed with DI water. The reaction mixture used for the previously described Stöber growth process, containing the VO_2 nanowires, TEOS, and NH_4OH dispersed within a water:ethanol mixture was used as the solution that was spray-coated onto the glass slides. The nanowire dispersions were spray-coated using a Master airbrush (G79) with nozzle diameter of 0.8 mm utilizing an air compressor with output pressure of 40 psi. This process was repeated several times to obtain a homogeneous coating on the slides. The glass substrates were annealed under various ambients as described below. For comparison, core—shell VO_2@SiO_2 nanowires prepared as described above were dispersed in isopropanol using ultrasonication for 10 min. An aliquot of the solution was then removed and sprayed onto the freshly cleaned glass substrate.

II.2.4 Characterization

The VO_2@SiO_2 core-shell nanowires were characterized using a variety of methods. The surface morphologies of the coatings and nanowires were examined using scanning electron microscopy (SEM, Hitachi SU-70 operated at 5 kV and equipped with an energy dispersive X-ray spectroscopy detector). The nanowire/silica shell interfaces were further examined using high-resolution transmission electron microscopy (HRTEM) (JEOL-2010, operated with an accelerating voltage of 200 kV and a beam current of 100 mA). The samples for HRTEM were prepared by dispersing the coated VO_2 nanowires in ethanol and placing the solution on a 300-mesh copper grid coated

with amorphous carbon. The grid was then allowed to dry under ambient conditions. Raman spectra were obtained using a Jobin-Yvon Horiba Labram HR800 instrument coupled to an Olympus BX41 microscope using the 514.5 nm laser excitation from an Ar-ion laser. The laser power was kept below 10 mW to avoid photo-oxidation. Differential scanning calorimetry (DSC, Q200 TA instruments) measurements under flowing argon atmosphere in a temperature range from -50°C to 150°C were used to determine the transition temperature of the prepared nanowires.

Adhesion testing was performed using the American Society for Testing Materials (ASTM) Test 3359. Briefly, a grid was defined on the coated substrate using the designated tool. Tape was then applied to the substrate and peeled. The coating was then classified (0B to 5B) according to the standards prescribed for this ASTM method. FTIR measurements were performed between 25 and 105°C using a Bruker Vertex 70 instrument using a MCT detector, a LaTGS detector, and a thermal stage. The samples were allowed to equilibrate at each temperature for 30 min prior to acquiring a spectrum.

II.3 Results and Discussion

Figure II. 1A shows an indexed powder X-ray diffraction (XRD) pattern of the as-prepared VO_2 nanowires indicating that they are stabilized in the M1 monoclinic crystal structure. Figure II. 1B indicates a panoramic SEM image of the nanowires attesting to the high purity of the synthetic process. The nanowires range in diameter from 20 to 250 nm and can span tens of micrometers in length. To enhance the thermal stability of the VO_2 nanowires and to ensure improved adhesion to glass substrates, we

have sought to encapsulate the nanowires within a SiO_2 shell. SiO_2 is optically transparent in the visible region of the electromagnetic spectrum and is not expected to deleteriously impact the visible light transmittance of the prepared coatings. Furthermore, the SiO_2 shells can be readily functionalized to bind to hydrophilic or hydrophobic surfaces.[81] Figure II. 2 illustrates the two approaches developed here for (a) encapsulating VO_2 nanowires within a SiO_2 shell; and (b) embedding the VO_2 nanowires within a SiO_2 matrix bonded to glass.

Both approaches are based on a modified Stöber method involving the hydrolysis of a substituted silane (Figure II. 2). Subsequent to hydrolysis of TEOS, the condensation of silicic acid moieties results in the formation of a Si—O—Si linkage (Steps 1 and 2 of Figure II. 2). Continued condensation results in creation of amorphous silica.[82] Under conditions favoring homogeneous nucleation, SiO_2 nanoparticles are obtained, whereas heterogeneous nucleation onto other surfaces induces the formation of conformal silica shells.[83–86] For covalent attachment of the silica shells to other metal oxides, the presence

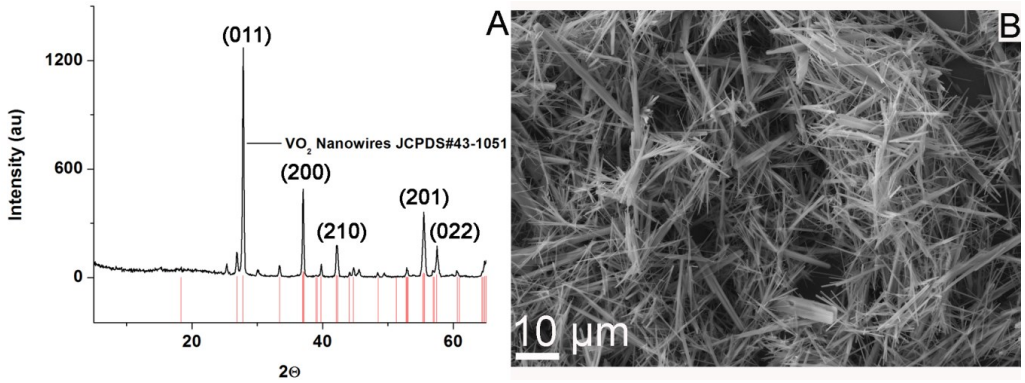

Figure II. 1 A) XRD pattern of as-prepared VO_2 nanowires indexed to the monoclinic M1 crystal structure B) SEM image of as-prepared VO_2 nanowires

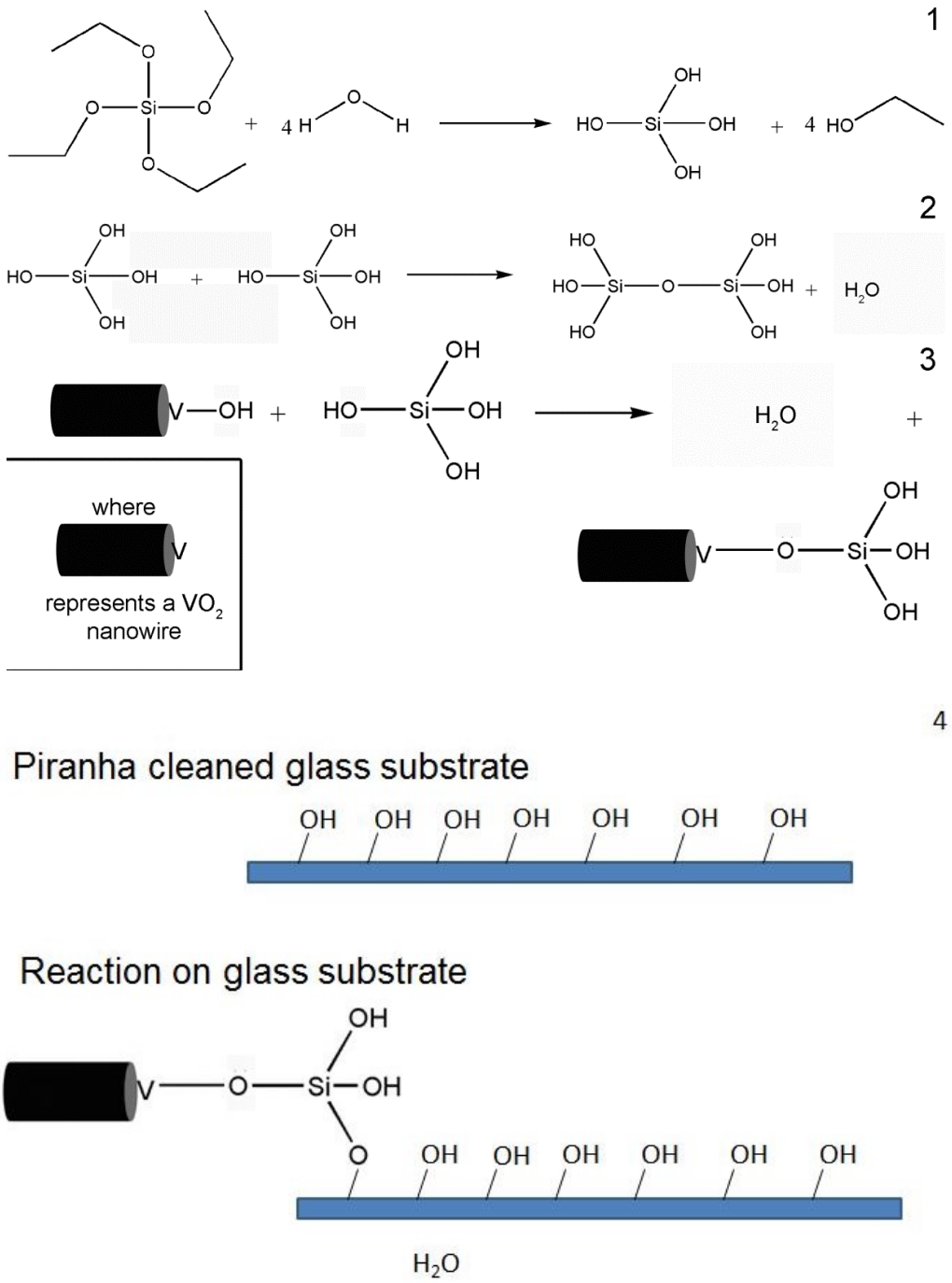

Figure II. 2 Steps 1—3 illustrate the hydrolysis of TEOS to form silanols that can be subsequently be condensed with pendant hydroxyl groups on the surfaces of the VO_2 nanowires to nucleate the SiO_2 shell. Step 4 illustrates the method used to bond the VO_2 nanowires to glass.

of accessible hydroxyl groups on the metal oxide surfaces is required; these functional groups can condense with the silicic acid moieties to form, in this case, Si—O—V linkages.[87,88] Further condensation and polymerization gives rise to the amorphous SiO_2 shell around the VO_2 nanowires (as schematically illustrated in Step 3 of Figure II. 2).[89] In addition, Step 4 of Figure II. 2 illustrates the covalent attachment of VO_2 nanowires to cleaned glass substrates. The piranha solution hydroxylates the surface of the glass substrate. The exposed –OH functional groups then condense with the silicic acid moieties linked to the VO_2 nanowires (Step 4 of Figure II. 2). Further condensation results in a matrix of amorphous SiO_2 enveloping VO_2 nanowires and strongly adhering these materials to the glass substrate.

The stabilization of VO_2@SiO_2 core-shell nanowires has been attempted using reaction times of 15, 30, and 60 min. The surface morphologies of the nanowires have been examined by SEM and TEM, as exemplified in Figure II. 3. Discontinuous precipitates are observed by TEM on the surfaces of the VO_2 nanowires after reaction for 15 min (Figure II. 3B). After 30 min of reaction, a complete shell is observed to encapsulate the nanowires and is discernible in SEM images as an amorphous coating on the nanowire surfaces (Figure II. 3C, inset). The shell appears to further thicken upon prolonging the reaction time to 60 min (Figure II. 3D). The shell is noted to be rough and has a wavy profile as expected for an amorphous layer, which is in stark contrast to the cleanly faceted surfaces of the crystalline VO_2 nanowires. The shell further exhibits a much lower electron density contrast, which is explicable considering the relatively low density of amorphous SiO_2 and

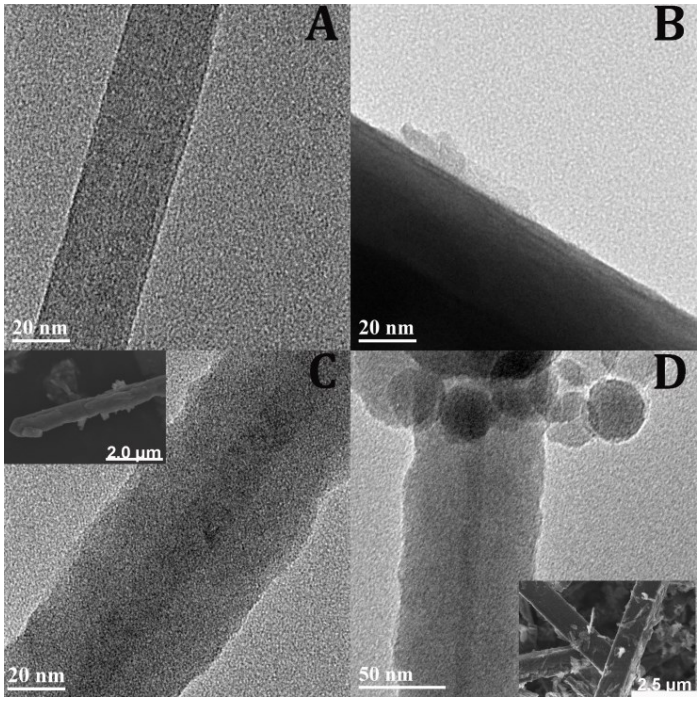

Figure II. 3 TEM images for A) VO_2 nanowires without a silica shell; B) VO_2 nanowires after reaction with TEOS for 15 min; C) VO_2 nanowires after reaction with TEOS for 30 min; and D) VO_2 nanowires after reaction with TEOS for 60 min. The insets to C) and D) indicate SEM images of the core-shell nanowires.

the higher atomic mass of the VO_2 core. Indeed, energy dispersive X-ray spectroscopy (Figure A. 1) indicates the presence of Si on the nanowire surfaces.

In order to evaluate the effectiveness of the SiO_2 shell in protecting the VO_2 nanowires from thermal oxidation, different annealing procedures have been attempted for VO_2 nanowires that are covered with continuous SiO_2 shells of at least 20 nm thickness. The core—shell structures have been annealed at 300°C in a tube furnace either under a flowing Ar ambient or in a muffle furnace under an air ambient. Figure II. 4 shows SEM and TEM images of VO_2 nanowires reacted with TEOS for 30 min after

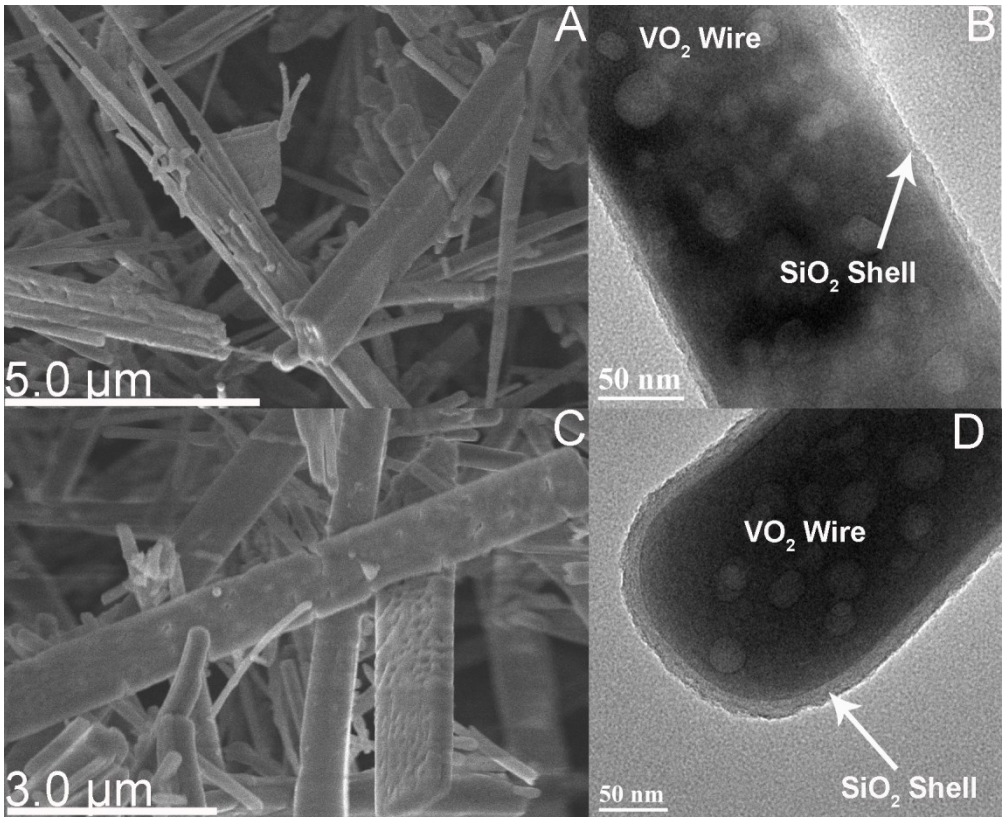

Figure II. 4 A) SEM and B) TEM images of VO_2@SiO_2 core-shell nanowires reacted with TEOS for 30 min and then annealed in air for 60 min at 300°C. C) SEM and D) TEM images of VO_2@SiO_2 core-shell nanowires reacted with TEOS for 30 min then annealed in Ar ambient for 60 min at 300°C.

annealing at 300°C under air and Ar ambients. Annealing appears to induce some agglomeration of the nanowires, perhaps as a result of increased dehydration and crosslinking between nanowires through inter-nanowire Si-O-Si linkages, although the nanowires are observed to retain their intrinsic 1D morphology. Figure II. 4C shows the characteristic roughness of the surface of the SiO_2 shell. No appreciable change in Si concentration is evidenced by energy-dispersive X-ray spectroscopy. The TEM images for these samples depicted in Figure II. 4B and D also suggest a slight decrease in the

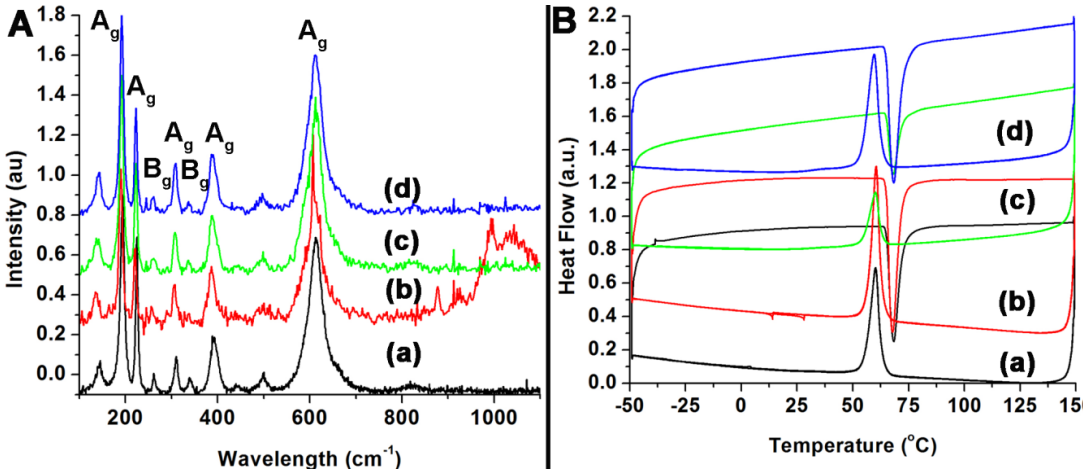

Figure II. 5 A) Raman spectra and B) DSC plots contrasted for the following samples: (a) VO_2 nanowires without a silica shell; (b) VO_2 nanowires after reaction with TEOS for 30 min; (c) VO_2@SiO_2 nanowires reacted for 30 min then annealed in Ar at 300°C; and (d) VO_2@SiO_2 nanowires reacted for 30 min then annealed in air at 300°C. The assignments to the Raman active modes of monoclinic VO_2 are noted in (A). The valleys in (B) are ascribed to the endothermic transition from M1→R phases, whereas the peaks are attributed to the exothermic R→M1 transitions.

thickness of the SiO_2 shells, which further appear to be better defined. Notably, we have not observed any lattice fringes for the SiO_2 shells before or after annealing attesting to their amorphous nature.

Notably, prolonged annealing of uncoated VO_2 nanowires in air at 300°C results in oxidation of these materials to V_2O_5.[10] Raman microprobe studies have been performed to evaluate the structural integrity and phase purity of the coated VO_2 nanowires. The M1 phase of VO_2 corresponds to the $P2_1/c$ (C_{2h}^3) space group and indeed group theory analysis predicts the existence of 18 distinctive modes: 9 of A_g symmetry and 9 with B_g symmetry.[90,91] Figure II. 5A indicates the Raman spectra of the annealed samples. The A_g and B_g modes are observed to be retained for the annealed samples,

including upon annealing in air, confirming that the coating and annealing process does not alter the crystal structure of VO_2 nanowire cores.[76] Upon deposition of the SiO_2 shell, the broad band centered at ca. 980 cm^{-1} can be ascribed to Si-OH vibrations.[92] Once the coated VO_2 nanowires are annealed, the Si-OH band is no longer observed. The elimination of the Si-OH modes further suggests that annealing the nanowires results in dehydration of the silica shell and increased cross-linking between nanowires. Notably, no bands characteristic of the M2 phase, thought to be stabilized as a result of strain,[24] are observed upon deposition of the shell or subsequent annealing, suggesting that the conformal amorphous SiO_2 shells do not induce significant strain at room temperature. The SiO_2 shells are thus observed to increase the robustness of the nanowires towards thermal oxidation.

To further evaluate whether the deposition of a SiO_2 shell and subsequent annealing alters the functionality of the VO_2 nanowires, DSC measurements have been used to examine the structural transition temperatures of the core—shell materials (Figure II. 5B). As noted above, the M1→R structural transformation is first-order in nature and thus associated with a latent heat of reaction. The bond distortions and the abrupt change in the entropy of the conduction electrons across the phase transition give rise to distinct features in DSC plots.[18,78,93] As the nanowires are heated, an endothermic transformation from the monoclinic to the tetragonal phase is visible as a valley in the DSC plot. Subsequently, as the sample is cooled, a pronounced peak corresponding to the exothermic tetragonal→monoclinic transformation is evidenced (Figure II. 5B). Indeed, encapsulation by a SiO_2 shell and subsequent annealing do not appreciably affect

the critical transition temperatures of the VO_2 cores, suggesting that the shells can enhance thermal robustness of the VO_2 nanowires without interfering with their functionality. Notably, the amorphous character of the SiO_2 shell implies that it is not epitaxially matched with the crystalline VO_2 nanowire cores, and is further likely to be able to accommodate substantial strain given that the amorphous SiO_2 lattice is not close packed. The ability to coat VO_2 nanowires without subjecting them to deleterious strain effects or adventitious doping that can shift the transition temperature represents a significant advantage for these materials.[94]

Next, we have pursued the integration of VO_2 nanowires onto glass substrates.

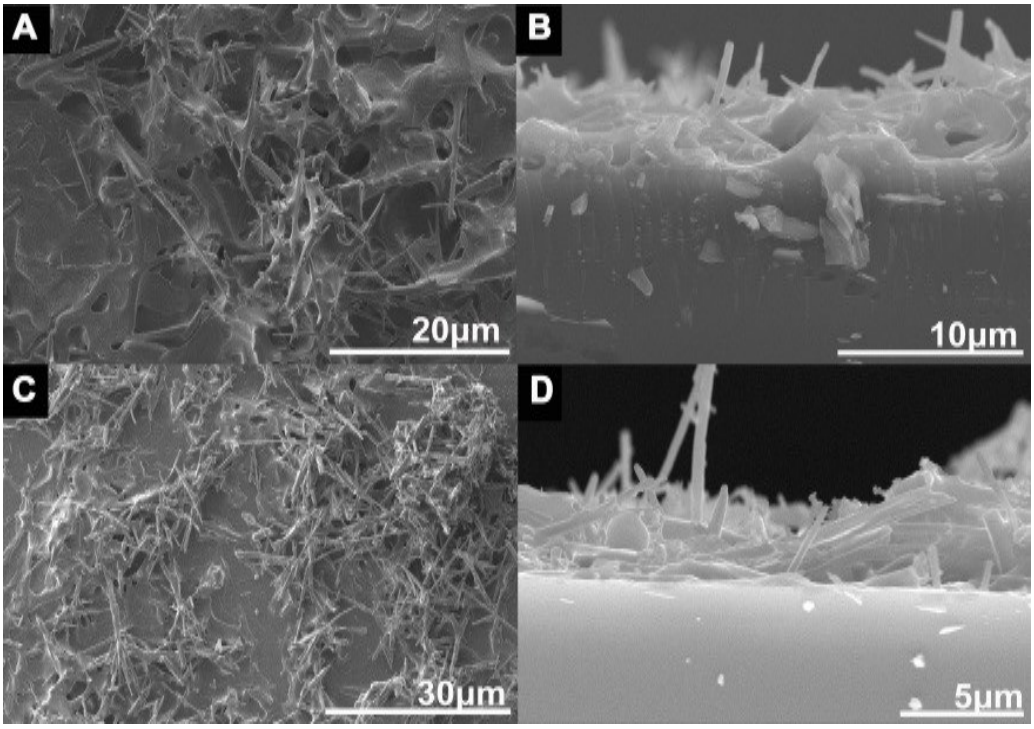

Figure II. 6 A) Top-view and B) Cross-sectional view SEM images of VO_2 nanowires embedded in an amorphous SiO_2 matrix bonded to glass. The coatings shown in (C) and (D) were annealed at 100°C in air for 60 minutes.

Two separate methods for depositing VO_2@SiO_2 nanowires onto glass have been explored. In the first approach, the core—shell nanowires have been spray-coated onto the glass substrates from 2-propanol dispersions. In a second approach, the reaction mixture used for the modified Stöber growth process has been used as the precursor solution for spray-coating. Aliquots of the solution are continually sprayed to achieve the desired thickness. The former does not yield adequate adhesion to the glass substrates (*vide infra*) and thus the latter method is described in more extensive detail. Figure II. 6 shows

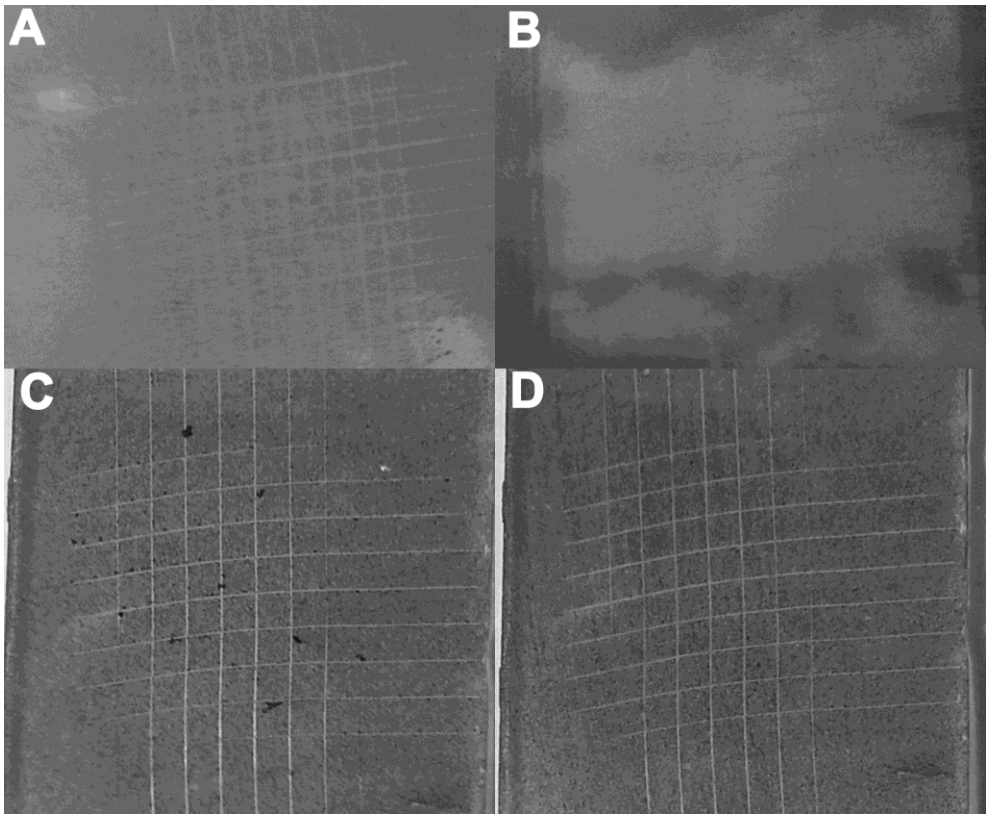

Figure II. 7 A), B) Spray-coated VO_2 nanowires on a glass surface before and after ASTM test 3359. Significant flaking is observed and the peeled sample is assigned a grade of 0B. C), D) The VO_2/SiO_2 coatings exhibit excellent adhesion and are classified as 5B.

top-view and cross-sectional SEM images of VO_2 thin films embedded in a SiO_2 matrix bonded to glass (as per Step 4 of Figure II. 2). The nanowires are seen to be enrobed in amorphous SiO_2 analogous to the core-shell motifs described above. The thickness of the silica matrix is substantially decreased after annealing as shown in comparing the cross-sectional SEM images. Coated substrates that are ca. 2-5 μm in thickness have been further evaluated in adhesion tests and for near-infrared switching.

ASTM D3359 has been used to test the adhesion of the nanowires onto glass. As per ASTM standards, the coatings are classified in the range between 5B (strongly adhered, where the coating is not visibly removed upon peeling the tape) to 0B (corresponding to removal of greater than 65% of the coating). While VO_2 or core—shell VO_2@SiO_2 nanowires spray-coated onto glass are readily removed by applying an adhesive tape to the substrate (Figure II. 7A, B), the VO_2/SiO_2 samples show excellent adhesion with or without annealing and can be classified as 5B, the strongest adhering category by this test. Annealing to 100°C does not appear to significantly increase the extent of adhesion as per this method of categorization.

Figure II. 8 shows the infrared transmittance measured for the VO_2/SiO_2 coatings adhered onto glass. The sharp decrease in transmittance with increasing temperature is consistent with transition to a metallic (infrared-reflective) phase and is entirely reversible upon cooling. The thermally induced infrared switching realized for the silica-embedded glass substrates provides a practical means of modulating infrared gain for optoelectronic or thermochromic glazing applications.

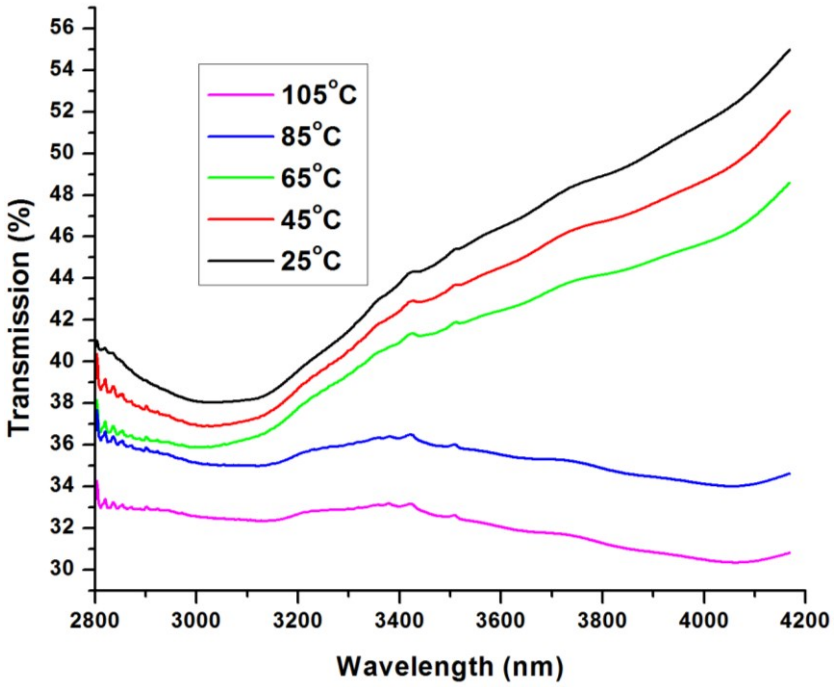

Figure II. 8 NIR transmittance in the range between 2800 and 4200 nm indicating the transmittance is sharply decreased with increasing temperature with a pronounced discontinuity evidenced at the phase transition temperature of 67°C. There is a slight change in the transmittance before and after the phase transition temperature due to the variation in the dimensions of the nanowires, causing slightly different transition temperatures.

II.4 Conclusion

In summary, we have shown that a SiO_2 shell can be constituted around VO_2 nanowires using the modified Stöber process. The thickness of the shell can be varied by changing the reaction time. Reaction times of 30 and 60 min result in formation of continuous conformal shells around the nanowires as evidenced by electron microscopy observations. The SiO_2-encapsulated VO_2 nanowires exhibit increased robustness to thermal oxidation. The crystal structure and functionality of the VO_2 core is retained

upon encapsulation with the SiO_2 shell and no appreciable modification of the phase transition temperature has been evidenced. A method for obtaining excellent adhesion of the nanowires to glass substrates has been developed based on dispersing VO_2 nanowires within an amorphous SiO_2 matrix. Indeed, the coatings exhibit excellent attenuation of infrared transmittance upon heating past the phase transition temperature. Future work will focus on examining coatings constituted from W- and Mo-doped VO_2 nanowires with phase transition temperatures in close proximity to room temperature.

CHAPTER III

PARTICLE-SIZE-DEPENDENT MODULATION OF THE THERMOCHROMIC PROPERTIES OF NANOCOMPOSITE VO_2 THIN FILMS

III.1 Introduction

Buildings consume an inordinately large amount of energy across the planet and are often static structures that interact little with their outside environment.[95] A recent report from the United Nations estimates that 30—40% of primary energy usage across the world occurs within buildings.[95] In the United States, the Department of Energy estimates that 41% of the total energy consumption occurs within buildings.[96,97] Much of the energy consumed within buildings goes towards space cooling, space heating, lighting, and ventilation. Incorporating responsive elements that can adapt to external stimuli (e.g., external temperature and humidity) within structural elements has been proposed as a potential means of reducing the energy footprint of buildings.[26,98] Fenestration elements such as windows, doors, and skylights, play an important role in determining the solar heat gain of a building. Such elements must balance the competing needs of enabling interiors to be lighted using natural daylight while modulating solar heat gain to acceptable levels. Consequently, there is great interest in spectrally selective glazing and thin films that allow for transmission of visible light but exhibit dynamically tunable infrared transmittance.[26,28,29,98–101] Such thin films are expected to bring about substantial energy savings by reflecting infrared light during periods of high ambient temperature (thereby reducing the need for space cooling) but permitting transmittance

of infrared light during periods of low ambient temperature when the solar heat gain can be harnessed to reduce heating costs.

Dynamically tunable glazing requires stimuli-responsive modulation of optical transmittance, which can be achieved variously by means of thermotropic or lyotropic phase transitions in polymers or hydrogels, electric-field-induced ion intercalation in redox-active host materials, reversible amorphous to crystalline transitions in phase-change materials, electric-field-induced change of polarization of liquid crystals, or electronic solid—solid phase transitions.[3,5,7,11,57,98,101,102] Thermochromic transitions are particularly important as a facile means of developing dynamically switchable glazing that does not require external voltage control.[4] Compounds that exhibit pronounced modulations of optical transmittance as a result of electronic transitions wherein the intrinsic electronic conductivity (carrier concentration and/or mobility) is dramatically altered are particularly attractive.[3,7,16,103] However, there exists only a relatively sparse set of compounds characterized by large thermally induced modulations of electrical conductance; such electronic phase transitions are underpinned typically by either electron correlation or electron—phonon coupling.[3,16,103–106] The binary vanadium dioxide (VO_2) is notable in having an electronic phase transition that occurs in close proximity to room temperature.[16,107] In the bulk, the metal—insulator transition of VO_2 is observed at ca. 67°C but can be depressed through either size control and/or doping.[4,12,13,23,107] The underlying origin of the transition remains hotly contested given that the transition has both electronic (Mott—Hubbard) and structural (Peierls') attributes.[12,16,17,91,108] The latter derives from the accompanying structural

transformation from a low-temperature monoclinic M1 phase to a more symmetric tetragonal phase.[17] Regardless of the fundamental origin of the transition, the dramatic modulation of optical transmittance and electrical conductivity observed at the phase transition makes VO_2 a useful material for practical applications.

For deployment of VO_2 within thermochromic thin films, wherein it can be integrated within various parts of the building envelope,[29,32,101] three compelling needs must be addressed: (a) the visible light transmittance must be maintained as high as possible while maximizing thermochromic modulation in the near-infrared region of the electromagnetic spectrum; this requires mitigation of light scattering through identification of optimal crystallite dimensions. (b) The thin film must be thermally cyclable without strain-induced pulverization; the substantial lattice strain accompanying the structural phase transformation renders the deployment of continuous thin films rather difficult and instead nanostructures embedded within suitable matrices are better able to accommodate such strain. [31,109,110] (c) The nanocrystallites need to be well dispersed within the host matrix to prevent light scattering and to ensure retention of mechanical integrity of the film across multiple thermal cycles. It is thus expected that a viable thermochromic thin film will comprise high-crystalline-quality VO_2 nanocrystals of the optimal particle size embedded within the appropriate host matrix.[111]

Previous work has shown that high-crystalline quality VO_2 nanocrystals are accessible through low-temperature hydrothermal methods.[13,18,23,112] Such methods provide substantial control over particle size and dopant incorporation; the obtained nanostructures can be thermally cycled without pulverization. In past work, we have

incorporated hydrothermally grown VO_2 nanowires within an amorphous silica matrix utilizing a modified Stöber method.[113] The silica matrix permits adhesion to glass substrates and provides protection against oxidation. VO_2 particles has further been used in other studies to prepare films using polymer-assisted deposition and through mixing with an acrylic resin.[114,115] However, the first and third of the two problems noted above: optimal particle size and good dispersion remain to be adequately resolved. Here, we contrast the visible light transmittance and infrared modulation obtained for different particle sizes of VO_2 embedded within a commercially available methacrylic acid/ethyl acrylate copolymer, Acrysol ASE-60. The rheology of this matrix enables the use of draw-down coating for the preparation of nanocomposite VO_2 thin films. Films formulated with four different sizes of VO_2 nanocrystals at various mass loadings have been examined underscoring the need for nanoscale dimensions and good dispersion to obtain high degrees of thermochromic modulation.

III.2 Experimental

III.2.1 Synthesis of VO_2 Nanowires

VO_2 nanowires were synthesized through a variation of the one-step hydrothermal method reported in our previous work.[13] Briefly, stoichiometric amounts of micron-sized V_2O_5 powder (Sigma-Aldrich, 98%) were placed in a polytetrafluoroethylene cup with deionized water (ρ=18.2MΩ/cm, Barnstead Water Purification System) and a reducing agent (either 2-propanol or acetone). The cup was then sealed in an autoclave and heated at 210°C for 18—72 h. The synthesized powder

was then vacuum filtered and washed with 2-propanol, acetone, and/or water. The powders were subsequently annealed at 550°C under inert Ar atmosphere for several hours to obtain pure VO_2 nanocrystals crystallized in the M1 phase upon cooling.

III.2.2 Hexane Milling of VO_2 Nanowires

VO_2 nanowires synthesized hydrothermally *via* reduction with 2-propanol were milled in hexanes to reduce the particle size. The material was milled with yttrium-stabilized zirconia balls after first dispersing VO_2 nanocrystals at a concentration of 100 mg/mL in hexanes. The samples were milled for a total of 90 min at 30 min intervals using a SPEX SamplePrep 510 Mixer Mill.

III.2.3 Synthesis of Ultra-small VO_2 Nanocrystals

Ultra-small VO_2 nanocrystals were synthesized *via* a two-step reaction developed based on the literature.[116,117] The first step involved the precipitation of $VO(OH)_2$ from the reaction of NH_4VO_3 and H_2NNH_2 at 80°C in deionized water (ρ=18.2MΩ/cm, Barnstead Water Purification System). The $VO(OH)_2$ precipitate was then placed within a hydrothermal vessel and heated at 210°C for 24—72 h. The product was finally isolated through centrifugation and used without further annealing or milling.

III.2.4 Deposition of a SiO_2 Shell and Preparation of VO_2@SiO_2 Nanocrystals

An amorphous silica shell was deposited onto nanoparticles using a modified Stöber method as previously reported.[113] Briefly, VO_2 nanocrystals (24mg to 240mg) were sonicated in a 4:1 ethanol:water solution until well-dispersed. Ammonium hydroxide was added as a catalyst followed by addition of tetraethylorthosilicate. The

reaction proceeds for 25 min and the VO_2@SiO_2 nanocrystals were collected by centrifugation.

III.2.5 Acrysol Dispersions

VO_2@SiO_2 core—shell nanocrystals were dispersed in 10 mL of an alkali water solution (pH of ca. 11.3) in a glass vial by ultrasonication. The dispersion was then gently stirred and Acrysol ASE-60 (Dow Chemical Company) was introduced at 1 wt.% relative to water (adjusted to account for Acrysol ASE-60's solid content being around 28%). The solution was stirred more vigorously as the solution thickened to further homogeneously disperse the nanocrystals within the polymeric formulation. When all of the Acrysol ASE-60 had dissolved (ca. 20 min), the dispersion was allowed to stand and used for casting thin films.

III.2.6 Film Casting

Nanocomposite thin films of VO_2@SiO_2 were cast onto borosilicate glass substrates using 1.25 mL of the Acrysol/VO_2 dispersion with various loadings of VO_2 nanocrystals (4—8 mg of VO_2@SiO_2 dispersed in 10 mL of the acrylate aqueous solution). The dispersion was placed on the glass slide and drawn down using a BYK film casting knife set to a wet thickness of 1 mm. The films were then allowed to dry overnight in an air ambient. The dry thickness of the films was on the order of ca. 20 μm.

III.2.7 Characterization

High-resolution transmission electron microscopy (HR-TEM) images of VO_2 and VO_2@SiO_2 nanocrystals were obtained using a JEOL JEM-2010 instrument operated at

200 kV with a beam current of 100 mA. Samples for HRTEM were prepared by dispersing the VO_2 nanoparticles in 2-propanol or ethanol and dropping the dispersion onto 300 mesh copper grids coated with amorphous carbon. The grid was then allowed to dry under ambient conditions. Absorbance spectra of VO_2@SiO_2/Acrysol dispersions in water were obtained using a Hitachi U-4100 UV-Vis-NIR spectrophotometer. UV-visible/near-infrared (UV-Vis-NIR) transmission spectra of all nanocomposite films were obtained using a multi-wavelength Bruker Vertex-70 FTIR spectrometer. The films were heated using a Pike Technologies temperature stage and allowed to equilibrate for 10 min prior to acquiring high-temperature measurements. All transmission spectra were corrected for the transmission of Acrysol ASE-60 by taking the ratio of the VO_2 films to an Acrysol-ASE 60 film cast by the same method using equation III.1:

$$([T_{VO2+acrysol}/T_{acrysol}]*100\%) \qquad \text{(III.1)}$$

III.3 Results and Discussion

The use of nanoparticles instead of continuous thin films provides several key advantages. First, as noted above, strain induced delamination and pulverization of continuous thin films resulting from the lattice mismatch at the monoclinic—tetragonal structural phase transition can be mitigated.[13] Secondly, nanocrystals embedded within thin films serve as retrofittable solutions that can be deployed onto existing buildings without requiring replacement of insulating glass units. Finally, nanocrystals can be prepared in high crystalline quality by scalable solution-phase methods and do not

require high-vacuum apparatus necessary for physical vapor deposition of VO_2.[112] However, as noted above this leads to a new set of challenges associated with

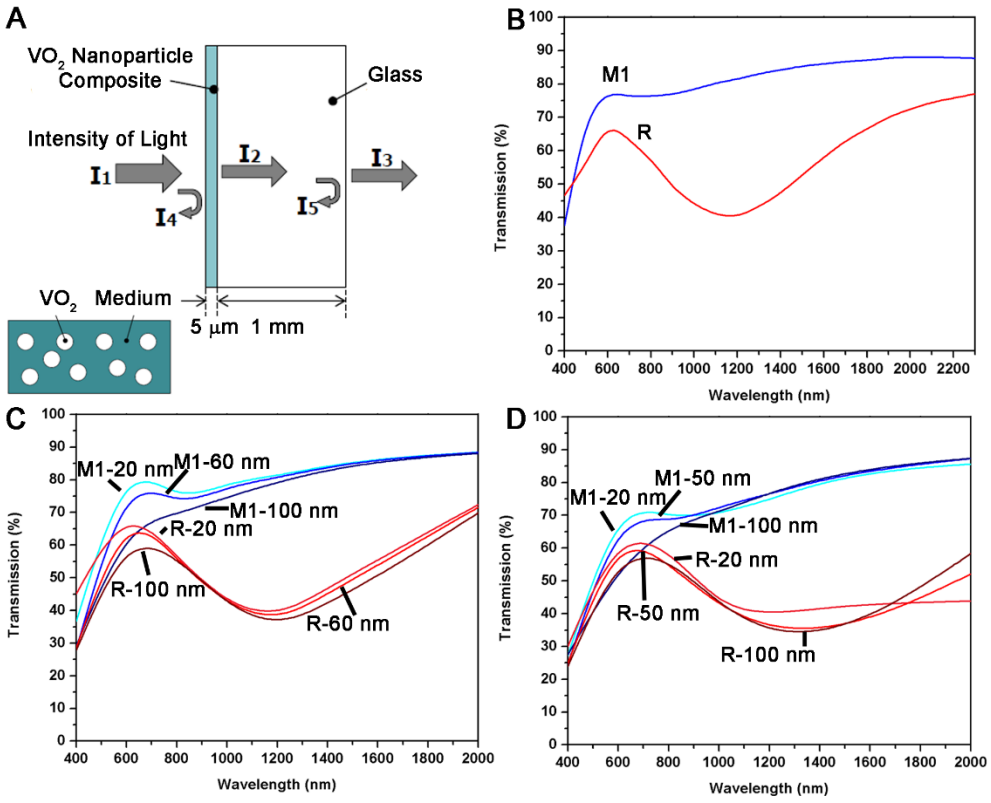

Figure III. 1 A) The transmission of VO_2 nanoparticles embedded within a 5 μm thickness polymeric film cast onto a 1 mm thick glass substrate is simulated using EMM and FEA+GO methods. I_1 is the incident light, whereas I_3 is the transmitted intensity and I_4 is the reflected intensity. Bulk optical constants for the insulating and metallic phases of VO_2 are used as described in the text. B) Transmittance spectrum simulated based on the effective medium model for spherical nanoparticles of insulating and metallic VO_2. C) Transmittance spectra simulated based on the FEA+GO approach for a nanocomposite with spherical VO_2 nanoparticles of varying diameters (as labeled in the plot) in the insulating and metallic phase. D) Transmittance spectra simulated based on FEA+GO for a nanocomposite with 100 nm length VO_2 nanowires of varying diameters (as labeled in the plot); spectra have been modeled for VO_2 in the insulating and metallic phase. All composites have a thickness of 5 μm and a fill factor of 3.7 wt.%. A temperature-invariant refractive index of 1.5 is assumed for the host polymeric matrix.

determining the optimal particle size and ensuring good dispersion of VO_2 nanocrystals within matrices.

Li *et al* have suggested a pronounced size dependence for the optical transmittance and near-infrared modulation of VO_2 nanocrystals embedded within a dielectric matrix.[33] These authors have found that films constituted by dispersing spherical and elliptical shaped VO_2 nanocrystals present several advantages over continuous thin films of VO_2. First, the spectral transmittance of the insulating phase of VO_2 is predicted to be much higher for films with VO_2 nanocrystals dispersed within a matrix as compared to continuous thin films. In addition, the near-infrared modulation for the particulate thin films was further found to be substantially greater than that of the continuous thin films.

In order to elucidate the particle size dependence of the optical properties, simulations have been performed using two models: the effective medium model (EMM) and finite element analysis + geometrical optics (FEA+GO). The simple EMM approach assumes that the nanoparticle has a single refractive index (n) and extinction ratio (k), and assumes that the particles are uniformly distributed throughout a low-refractive-index medium (Figure III. 1A). The simulated spectrum (Figure III. 1B) predicts a dramatic modulation of ca. 40% in the near-IR region of the electromagnetic spectrum using the optical constants of bulk VO_2 in the monoclinic (M1) and tetragonal phases.[33,118] The simulation assumes a constant refractive index of ca. 1.5, which is typical of polymeric media.[119] These results underscore the need for a uniform distribution of particles within a low-refractive-index matrix to achieve the desired NIR

modulation. The FEA+GO simulations allow for a more detailed elucidation of particle-size-dependent optical properties. Spectra have been simulated for a composite with a fill factor of 3.7 wt.% of spherical VO_2 nanoparticles of varying diameters again assuming a temperature-independent refractive index of 1.5 for the polymeric media and the bulk optical constants for the insulating and metallic phases. As the diameter increases from 20 to 100 nm, the near-infrared modulation is observed to remain constant at ca. 40% (Figure III. 1C). However, the visible light transmittance (at 680 nm) decreases from 80 to 68% for the low-temperature phase. When considering a composite of 100 nm long VO_2 wires with varying diameters, the 50 nm and 100 nm diameter wires show a variation of ca. 45% in the near-infrared, whereas the 20 nm wires show a modulation of ca. 40% (Figure III. 1D). Although the NIR modulation is slightly diminished for the 20 nm diameter nanowires, they retain superior visible light transmittance. The substantial diminution in visible light transmittance with increasing particle size is derived from the scattering background contributed by larger particles. Agglomeration of particles will to first order mimic the effects of having larger particles. These simulations indicate that the viability of utilizing VO_2 nanocrystals for effective thermochromic modulation will depend sensitively on their dimensions and their extent of dispersion.

In order to experimentally study the effects of particle size on the optical spectra of the nanocomposite films, VO_2 nanocrystals have been synthesized using different hydrothermal methods, as detailed in the experimental section.[13,116,117] Four different particle sizes are examined here: Sample **I** are nanowires prepared by the hydrothermal

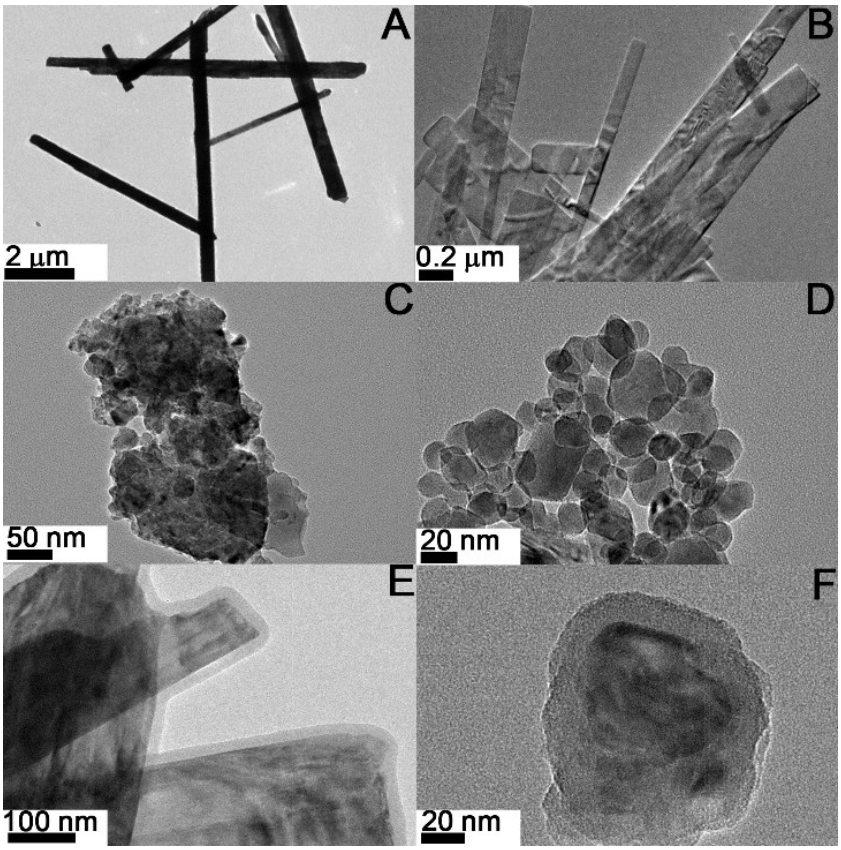

Figure III. 2 TEM images of VO_2 nanocrystals grown *via*: A) Hydrothermal reduction of V_2O_5 by 2-propanol (Sample I); B) Hydrothermal reduction of V_2O_5 by acetone (Sample A); C) Hydrothermal reduction of V_2O_5 by 2-propanol followed by wet-milling with yttria-stabilized ZrO_2 balls in hexanes media (Sample I-BM); and D) Precipitation of $VO(OH)_2$ followed by hydrothermal crystallization (Sample US). TEM images of VO_2 nanocrystals coated with an amorphous SiO_2 shell for E) Sample I and F) Sample US

reduction of V_2O_5 by 2-propanol and span 300±130 nm in diameter and range tens of microns in length as shown in Figure III. 2A.[112] The use of acetone as a reducing agent yields nanowires that again span several micrometers in length but with substantially reduced diameters of 110±70 nm. These samples are referred to as Sample **A**; Figure III. 2B shows TEM images of these nanowires. To reduce the longitudinal dimensions, the

nanowires of Sample **I** have been wet-milled with yttria-stabilized zirconia balls in hexanes media to obtain Sample **I-BM** (Figure III. 2C). Ball milling greatly diminishes the particle size to 49± 27 nm but a relatively large size distribution is observed and the nanocrystals are observed to be highly agglomerated. Finally, to achieve "ultra-small" nanocrystals with an approximate size distribution of 10±4 nm, $VO(OH)_2$ is first precipitated using sol—gel techniques, followed by hydrothermal crystallization (referred to as Sample **US**, Figure III. 2D).[116,117] The four samples examined here serve as effective test beds for elucidating particle size effects on visible light transmittance and near-infrared modulation.

In previous work, we have illustrated the importance of protecting the VO_2 nanocrystals from oxidative degradation by deposition of amorphous silica shells.[113] The silica shells do not alter the magnitude or phase transition temperature but passivate the surfaces of VO_2, endow stability up to temperatures of 300°C, and allow for much improved dispersion in aqueous media. In the absence of a SiO_2 coating, VO_2 nanocrystals dispersed in aqueous media are rapidly degraded to green substoichiometric vanadium oxides and orange V_2O_5. All four samples noted above have been coated with SiO_2 using a modified Stöber approach.[113] Figure III. 2E and F depict representative TEM images of silica-coated VO_2 nanocrystals indicating an average shell thickness of 20 nm.

In order to devise a scalable process for casting thin films of VO_2 nanocrystals, Acrysol ASE-60, a polyacrylic medium is used as a dispersant and thickener. Acrysol ASE-60 is typically stored under acidic conditions; upon titration of a base, methacrylic

acid groups within the copolymer become deprotonated and take on an anionic charge.[120] Charge repulsion between anionic groups induces swelling of the copolymer changing

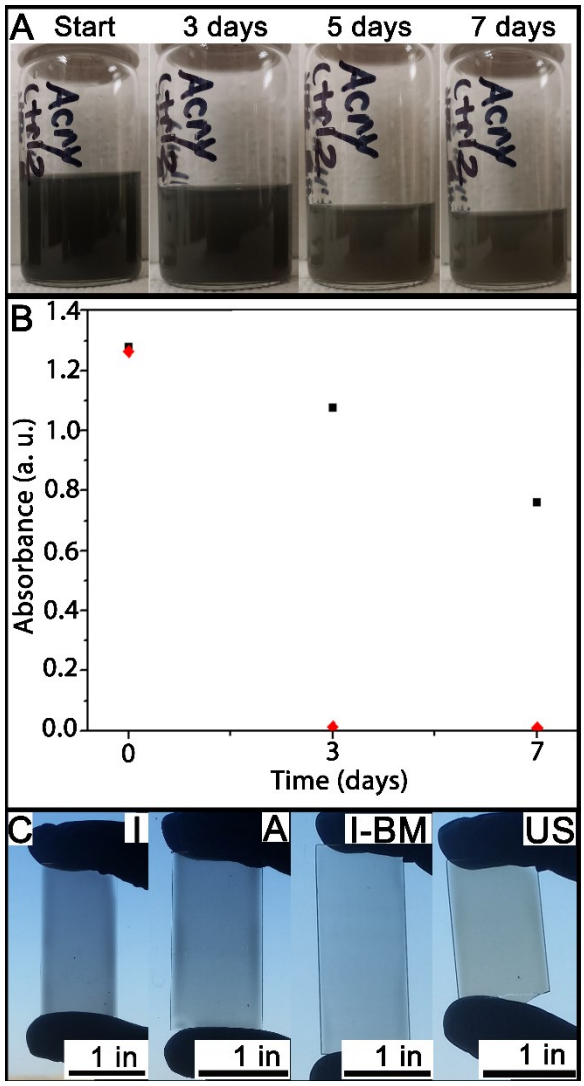

Figure III. 3 A) Digital photographs of aqueous dispersions of VO_2@SiO_2 nanocrystals dispersed using Acrysol ASE-60; B) Sedimentation plot of ball-milled VO_2@SiO_2 nanowires dispersed in deionized water (red diamonds) and in deionized water with the addition of 1 wt% Acrysol ASE-60 (black squares); C) Films cast for the four VO_2@SiO_2 samples with varying particle size (Samples I, A, I-BM, and US) from Acrysol ASE-60 aqueous solutions. In each case, the films have concentrations of 0.6 mg VO_2@SiO_2/mL solution.

the rheology and allowing for stabilization of colloidal dispersions of VO_2@SiO_2 nanocrystals. Figure III. 3A illustrates Acrysol-ASE-60 dispersions of VO_2@SiO_2 nanocrystals allowed to stand for up to 7 days after mixing. Figure III. 3B contrasts the stability of the VO_2@SiO_2 colloidal dispersions in deionized water and Acrysol-ASE-60 aqueous media (0.3 mg VO_2@SiO_2/mL solution) as a function of time clearly illustrating the decreased sedimentation obtained for the latter. The viscous acrylic dispersions have been used to form VO_2 nanocomposite coatings by a facile straight-edge knife casting

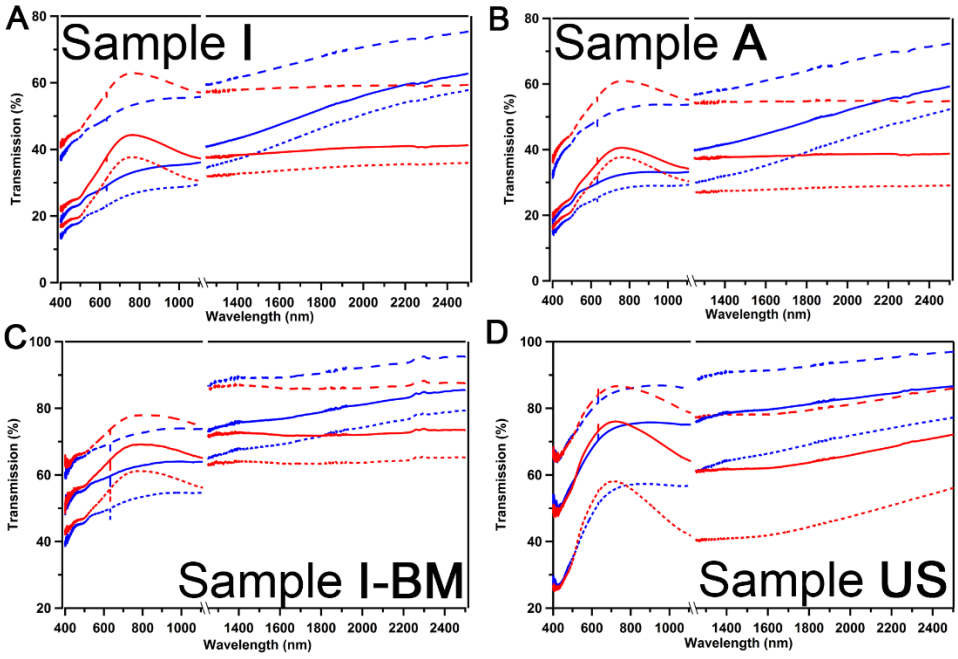

Figure III. 4 UV-Vis-NIR transmission spectra acquired for nanocomposite VO_2@SiO_2/Acrysol thin films prepared from dispersions prepared at nanocrystal loadings of 4 mg/10 mL (dashed lines), 6 mg/10 mL (solid lines), and 8 mg/10 mL VO_2 (dotted lines). In each case, blue spectra have been acquired at 35°C, whereas red spectra have been acquired at 85°C after equilibration for 10 min. A) Sample I at different nanocrystal loadings; B) Sample A at different nanocrystal loadings; C) Sample I-BM at different nanocrystal loadings; and D) Sample US at different nanocrystal loadings. The discontinuity at 1110-1250 nm corresponds to a change of the detector from Si Diode detector to a DLaTGS detector.

process. The obtained films are visually transparent and smooth as shown in Figure III. 3C. For the same VO_2 nanocrystal loading (0.6 mg VO_2@SiO_2/mL solution), it is clear that the nanowire samples with larger dimensions (Samples **I** and **A**) present a darker appearance as compared to the smaller nanocrystals (Samples **I-BM** and **US**).

UV-visible-NIR transmission spectra of nanocomposite films prepared using the four VO_2@SiO_2 samples are shown in Figure III. 4. Three different nanocrystal loadings have been contrasted in each instance. All the spectra show a clear divergence of the high-temperature (red) plots from the low-temperature (blue) plots. The insulating phase of VO_2 has a bandgap estimated to be ca. 0.8 eV whereas with closing of the gap and sharp increase in carrier density upon metallization, the reflectance is greatly increased and the transmittance is greatly diminished in the NIR region of the electromagnetic spectrum. Considering Figure III. 4A, for Sample **I**, the visible light transmittance is diminished and the NIR modulation is increased with increased particle loading. A similar trend indeed holds across all of the samples (Figure III. 4 and Table III. 1). Intriguingly, Sample **I-BM** shows the least amount of NIR modulation, which is substantially lower than that of the other three samples at comparable nanocrystal loadings. The poor performance of the hexane-milled samples, despite their small crystallite dimensions, is attributed to the loss of crystallinity induced by the harsh milling process. Indeed, X-ray diffraction data plotted in Figure A. 2 indicates an increased amorphous background. This amorphization diminishes the magnitude of the phase transition resulting in a much decreased modulation of NIR transmittance. The **I-BM** and **US** samples that have the smallest dimensions (49±27 and 10±4, respectively)

clearly show much greater visible light transmittance as compared to the **I** and **A** samples as a result of a reduced scattering background. The **US** sample with the smallest nanocrystal dimensions exhibits the best combination of high NIR modulation and visible light transmittance (Table III. 1).

Table III. 1. Collated data summarizing maximum NIR modulation, maximum transmittance in the visible spectrum, and onset of NIR modulation for the four different size distributions of VO_2 nanocrystals encapsulated within SiO_2 shells for various particle loadings dispersed in an acrylate matrix.

Sample	**Maximum NIR Modulation (%)**			**Maximum Transmittance in the Visible Spectrum (%)**			**Onset of NIR Modulation (nm)**		
	4 mg/ 10 mL	6 mg/ 10 mL	8 mg/ 10 mL	4 mg /10 mL	6 mg/ 10 mL	8 mg/ 10 mL	4 mg/ 10 mL	6 mg/ 10 mL	8 mg/ 10 mL
I	16.0	21.5	21.8	62.9	44.3	37.7	1250	1250	1250
A	18.5	20.5	23.2	61.0	40.6	37.7	1250	1250	1250
I-BM	8.0	12.0	14.1	77.9	69.2	61.2	1250	1250	1250
US	13.2	17.7	24.8	86.7	76.0	58.2	800	800	785

Notably, it is not just the extent of NIR modulation but also the onset of the modulation that will determine the efficacy of the nanocomposite in bringing about effective modulation of the solar heat gain. The onset of NIR modulation at relatively shorter wavelengths implies the ability to dynamically adjust transmittance for a relatively greater region of the solar spectrum.[121] For both Samples **I** and **A,** the onset of NIR modulation does not begin until ca. 1250 nm and the maximum NIR modulation is observed only at ca. 2500 nm, where the solar flux is rather weak. In contrast, for the **US** samples, the onset of the drop is blue-shifted to ca. 800 nm and much more rapidly reaches a maximum at ca. 1700 nm. Notably, NIR modulation below 700 nm is not

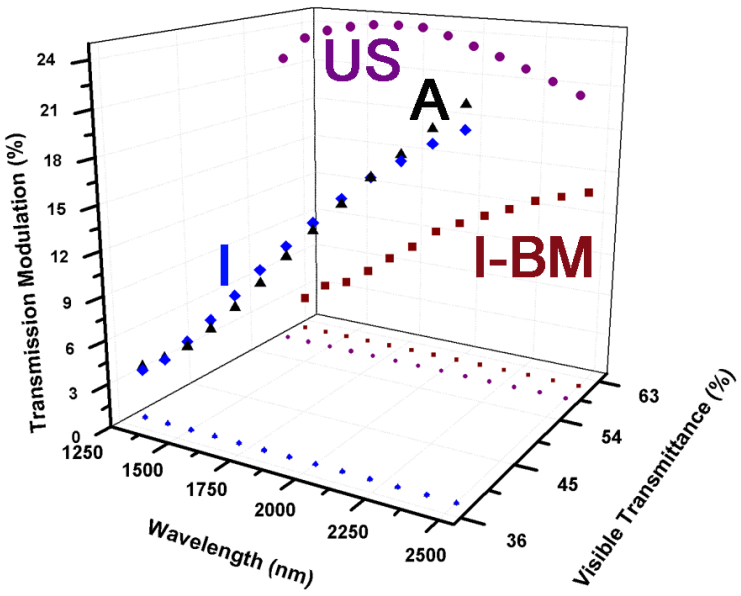

Figure III. 5 3D plot of the NIR modulation *versus* wavelength *versus* visible transmittance for the four sets of samples; **I** (blue diamonds), **A** (black triangles), **I-BM** (red squares), and **US** (purple circles). All samples shown here were at a concentration of 0.8 mg VO_2@SiO_2/mL solution.

desirable since that will bring about a pronounced change of the visible appearance of the film. Figure III. 5 contrasts the NIR modulation and visible light transmittance of the four different nanocrystallite sizes at a loading of 8 mg/10 mL and clearly indicates the vastly greater visible light transmittance and higher NIR modulation observed for the **US** sample with optimal nanocrystal dimensions. For the **I**, **A**, and **I-BM** samples, the modulation at 1300 nm is less than 5% and then sharply increases with increasing wavelength. The relatively diminished NIR modulation results from a pronounced scattering background for the larger particle sizes (the **I-BM** sample has agglomerates and some larger particles). In sharp contrast, the **US** sample maintains a modulation of ca. 20% across all wavelengths.

III.4 Conclusion

In conclusion, thermochromic modulation of NIR solar flux represents an attractive route for controlling solar heat gain based on the ambient temperature without deleteriously impacting the visible light transmittance of fenestration units. The pronounced near-room-temperature metal—insulator transition of VO_2 provides a means to modulate solar heat gain in a spectrally selective manner. Nanocrystals provide distinct advantages over continuous thin films in being able to better accommodate strains arising from thermal cycling and in affording a higher visible light transmittance. However, the use of nanocrystals requires elucidation of optimal crystallite dimensions and the appropriate dispersion of the nanocrystals within a low-refractive-index medium. EMM and FEA+GO optical simulations indicate a pronounced size dependence of the visible light transmittance for VO_2 nanocomposite thin films. Four different sizes of VO_2@SiO_2 nanocrystals have been synthesized and contrasted for thermochromic modulation and visible light transmittance after dispersed in an aqueous acrylate system and solution casting onto glass substrates. Ball-milling yields appropriate crystallite dimensions but results in considerable agglomeration and degradation of crystalline quality, which is reflected in a diminished NIR modulation. The smallest particle dimensions (10±4 nm, Sample **US**) appear to provide the best combination of visible light transmittance and NIR modulation (up to ca. 25%) with an onset of NIR modulation in the range of 785 nm. This latter system represents a viable thermochromic element that is entirely solution processed and deployable at large scales.

CHAPTER IV

INTEGRATING β-$PB_{0.33}V_2O_5$ NANOWIRES WITH CDSE QUANTUM DOTS: TOWARD NANOSCALE HETEROSTRUCTURES WITH TUNABLE INTERFACIAL ENERGETIC OFFSETS FOR CHARGE TRANSFER*

IV.1 Introduction

Tuning interfaces between disparate semiconductors, between molecules and semiconductor surfaces, and between semiconductors and metals remains of paramount importance for electronics, optoelectronics, photocatalysis, photovoltaics, and electrochemical energy storage.[39,122–124] Interfaces assume special significance for nanostructures given their high surface-to-volume ratios. Nanoscale heterostructures are of particular interest for photocatalysis owing to the tunability of the energies of the valence and conduction band edges of semiconductors as a function of finite size and doping, which allows for different components performing discrete functions to be assembled within modular platforms to facilitate sequential light-harvesting, charge transfer, and catalytic processes.[39,125] To enable programmable cascades of directional charge transfer reactions, heterostructures need to be designed keeping in mind several considerations such as the nature of the interface, the thermodynamics of band

---

* Reprinted with permission from "Integrating β-$Pb_{0.33}V_2O_5$ Nanowires with CdSe Quantum Dots: Toward Nanoscale Heterostructures with Tunable Interfacial Energetics Offsets for Charge Transfer" by K. E. Pelcher, C. C. Milleville, L. Wangoh, S. Chauhan, M. R. Crawley, P. M. Marley, L. F. J. Piper, D. F. Watson and S. Banerjee, *Chem. Mater.*, 2015, **27**, 2468–2479. Copyright 2015 American Chemical Society.

alignments between different components, and the kinetics of charge transfer. In this work, we have sought to design nanoscale heterostructures to exploit the availability of mid-gap states energetically positioned between the valence and conduction bands of a transition metal oxide; these states are derived from the stereoactive lone pairs of a post-transition metal cation and define a reconfigurable pseudo-gap. Two distinct synthetic routes are demonstrated for interfacing β-$Pb_{0.33}V_2O_5$ nanowires with CdSe quantum dots (QDs); we further show that the mid-gap states of the former are energetically situated in close proximity to the valence band edge levels of the latter and provide spectroscopic evidence for excited-state hole transfer from CdSe QDs to β-$Pb_{0.33}V_2O_5$ nanowires.

The primary objective of our interfacial design approach is to access the unusual "mid-gap" states of a mixed-valence ternary vanadium oxide bronze, β-$Pb_{0.33}V_2O_5$ to promote directional charge transfer within a nanoscale heterostructure. Mixed-valence ternary vanadium oxide bronzes with a composition of $M_xV_2O_5$, where M is a main-group or transition-metal cation and *x* describes the cation stoichiometry (variable with the specific cation and crystal structure), have been the subject of interest for many years owing to their various intriguing structural and electronic properties.[48,55] Recent attention has focused on the unusual low-dimensional charge transport pathways in these materials, which result from their highly anisotropic crystal structures and distinctive intercalant-dependent charge and spin-ordering motifs.[6,51–53,56,60] Specifically, electronic instabilities in these intrinsically anisotropic materials can be modulated to induce colossal metal—insulator transitions above room temperature and to stabilize superconducting states at high pressure.[6,53,56] Both the specific cation and its

stoichiometry can be readily tuned through variation of synthetic parameters, which provides a means to systematically modulate the extent of electron correlation and the overall electronic structure.

In recent work, we have developed a hydrothermal synthetic route to stabilize phase-pure β-$Pb_xV_2O_5$ nanowires.[48] Density of states calculations predict the presence of mid-gap states, located at intermediate energy between the conduction and valence band, for β-$M_{0.33}V_2O_5$ (where M is a cation such as Pb^{2+} characterized by a stereoactive lone pair of electrons).[52,60] Experimental evidence for these states has also emerged from recent variable-photon energy photoemission experiments that furthermore suggest that these states are primarily derived from anti-bonding Pb 6s—O 2p interactions and are positioned immediately below the lower Hubbard bands derived from splitting of V 3d states as expected in a strongly correlated picture.[49] As a result of these intercalating cations, a pseudo-bandgap is defined between the mid-gap states and the conduction band edge; an activation energy of 85—110 meV has been experimentally determined for the β-$Pb_xV_2O_5$ nanowires.[48] The energies and occupancies of these mid-gap states are thought to be tunable *via* choice of intercalating cation and the cation stoichiometry. Based on the bandgap (2.2 eV) and valence band edge potential of V_2O_5 (+2.2 to +2.6 eV with respect to the normal hydrogen electrode),[8,126–128] the mid-gap states of β-$Pb_xV_2O_5$ are postulated to lie at potentials slightly less positive relative to the valence bands of typical II-VI QDs, indicating that the transfer of photogenerated holes from QDs to the mid-gap states is thermodynamically favorable.[38,129] To the best of our knowledge, such lone-pair-derived states that are potentially reconfigurable have not

thus far been deployed for band engineering within heterostructures. Recent work involving chromophore-functionalized p-type semiconductor photocathodes provides precedent for charge separation *via* excited-state hole transfer to semiconductor substrates.[130,131]

In order to form photocatalytic heterostructures, we have paired β-$Pb_xV_2O_5$ nanowires with CdSe QDs. QDs, with size-dependent bandgaps and band-edge potentials and large oscillator strengths, have generated immense interest for light-harvesting applications.[39,68,132] Quantum confinement within semiconductor QDs allows for tunability of bandgaps, with the bandgap varying inversely with particle size.[133] The size- and composition-dependent energetics of semiconductor QDs is advantageous for preparing heterostructures with desirable band alignment and tunable driving forces for excited-state interfacial electron-transfer. Several approaches have been reported for functionalizing metal oxides with QDs, such as hot-injection and colloidal synthesis. These methods provide substantial control over QD size and the nature of the interface.[134,135] Here, we demonstrate the successful fabrication of novel nanoscale heterostructures by depositing CdSe QDs onto β-$Pb_xV_2O_5$ nanowires through distinct routes involving linker-assisted assembly and successive ionic layer adsorption and reaction (SILAR).

Linker-assisted assembly of QDs, involves tethering QDs to metal oxide surfaces *via* bifunctional linker molecules.[136–138] As an example, mercaptoalkanoic acids (MAAs) have been used to tether cadmium chalcogenide QDs to TiO_2 with charge transfer rates tunable by the length of the alkyl chain.[138] Photoanodes of QD-sensitized solar cells

with impressive power-conversion efficiencies (5-7%) have recently been prepared by linker-assisted assembly. [139,140] Alternatively, SILAR, a modification of chemical bath deposition methods,[72–74] involves the alternating immersion of a substrate into different solutions containing cationic and anionic precursors of QDs in order to form a thin film.[141,142] SILAR provides several advantages including generalizability to arbitrary substrates, easy control over film thickness by variation of the number of immersion cycles, and facile control over composition of the deposited overlayers by variation of synthetic parameters.[143] SILAR can further be elaborated to obtain doped QDs and core—shell structures.[75]

The heterostructures comprising CdSe QDs and β-$Pb_xV_2O_5$ nanowires are characterized by electron microscopy, electron diffraction, energy dispersive X-ray spectroscopy, and Raman spectroscopy. X-ray photoemission spectroscopy indicates substantial energetic overlap between the valence band of CdSe QDs and the mid-gap states of β-$Pb_{0.33}V_2O_5$ nanowires. Finally, spectroscopic measurements provide evidence for the transfer of photogenerated holes from CdSe to β-$Pb_{0.33}V_2O_5$. The specific selected systems – β-$Pb_xV_2O_5$ nanowires and CdSe QDs – serve to demonstrate the electronic coupling of valence band edges of QDs to the mid-gap states derived from stereoactive lone pairs of post-transition-metal intercalants with potential applicability to a diverse range of configurations of heterostructures with interfacial energetic offsets tunable by the specific intercalating cation and the size of the QDs.

IV.2 Experimental

IV.2.1 Materials

Commercially-available reagents and their sources are as follows: sodium sulfite, L-cysteine, vanadium pentoxide (Aldrich); electrochemical grade tetrabutylammonium perchlorate, selenium, selenium dioxide, cadmium sulfate octahydrate, cadmium nitrate tetrahydrate, 3-mercaptopropionic acid (Alfa Aesar); sodium hydroxide, sodium borohydride, and methanol (Fisher); lead acetate trihydrate (Fluka); anhydrous dichloromethane (EMD). All reagents were used as received without further purification. Glass slides coated with indium-doped tin oxide (ITO) were obtained from Delta Technologies, Limited (Loveland, CO 80537).

IV.2.2 Synthesis of β-$Pb_xV_2O_5$ and V_2O_5 Nanowires

β-$Pb_xV_2O_5$ nanowires were prepared using a one-step hydrothermal reaction as reported previously.[48] Briefly, stoichiometric amounts of $Pb(CH_3COO)_2{\cdot}3H_2O$ and V_2O_5 were placed in a polytetrafluoroethylene-lined acid digestion vessel (Parr) along with 16 mL of deionized (DI) water. The vessel was sealed in an autoclave and heated at 250°C for 72 h. The product was isolated by vacuum filtration, washed with copious amounts of water, and allowed to dry in air. V_2O_5 nanowires used as a control for spectroscopic experiments were prepared by the oxidation of hydrothermally grown $V_3O_7{\cdot}xH_2O$ nanowires as reported in previous work.[144]

IV.2.3 Synthesis of CdSe QDs

Cysteinate(2-)-capped CdSe (Cys-CdSe) QDs were synthesized by adaptation of the method reported by Park et al.[145,146], as reported previously.[147] Sodium selenosulfate

was prepared by refluxing an aqueous solution (42 mL) of selenium powder (0.17 g, 2.15 mmol) and sodium sulfite (0.8 g, 6.35 mmol) overnight (12-16 h). The cadmium precursor was an aqueous solution (18 mL) of cadmium sulfate octahydrate (42 mM in Cd^{2+}) and cysteine (180 mM). The pH of the solution was titrated to 12.5 – 13.0 with solid NaOH. The hot sodium selenosulfate solution (7.5 mL) was added to the cadmium precursor with stirring. The reaction was quenched with methanol after 30 minutes, resulting in the flocculation of QDs. Typical concentrations of cadmium, selenium, and Cys in the reaction mixture were 30, 15, and 113 mM, respectively. Dispersions of Cys-CdSe QDs were purified by solvent-nonsolvent washing to remove excess reagents. Methanol (30 mL) was added to 10 mL of an aqueous dispersion of as-synthesized QDs, resulting in the flocculation of QDs. The flocculate was removed *via* centrifugation and re-dispersed in 5 mL of deionized (DI) H_2O. This process was repeated once for a total of two purification cycles. Mercaptopropionate-capped CdSe (MP-CdSe) QDs were synthesized and purified by a similar procedure, except that the cadmium precursor solution contained MP (125 mM) instead of Cys.

IV.2.4 Functionalization of β-$Pb_xV_2O_5$ Nanowires with CdSe QDs by SILAR

SILAR was performed by adaptation of published methods.[148] A Na_2Se solution was prepared by reducing SeO_2 with $NaBH_4$. A 50 mM solution of SeO_2 in ethanol was stirred and degassed with argon on a Schlenk apparatus. Subsequently, 3 mmol of $NaBH_4$ was added to the solution, and the reaction was stirred under an argon ambient for 2 h. The cadmium precursor was a 100 mM solution of $Cd(NO_3)_2{\cdot}4H_2O$ in ethanol. β-$Pb_xV_2O_5$ nanowires (50 mg) were dispersed in 15 mL of ethanol through

ultrasonication. The dispersed nanowires and the cadmium and selenide precursor solutions were transferred to an argon-filled glove bag to prevent oxidation of selenide. To initiate the SILAR deposition of CdSe onto the β-$Pb_xV_2O_5$ nanowires, the solution of $Cd(NO_3)_2$ and the dispersion of nanowires were mixed, bringing the concentration of $Cd(NO_3)_2$ to 50 mM. The reaction was allowed to proceed for 30 s. The nanowires were removed from the reaction mixture by centrifugation at 4000 rpm for 90 s. The nanowires were then washed by mixing with ethanol (10 mL) for 30 s. The resulting dispersion of nanowires was then centrifuged for 90 s, and the supernatant was discarded. The freshly prepared 50 mM Na_2Se solution was then added to the nanowires and allowed to react for 30 s. The nanowires were then isolated by centrifugation at 4000 rpm for 90 s and washed with ethanol (10 mL). This final washing step marked the completion of one SILAR cycle. The number of SILAR cycles was varied to control the thickness of the CdSe layer deposited on the β-$Pb_xV_2O_5$ nanowires.

IV.2.5 Functionalization of β-$Pb_xV_2O_5$ Nanowires with CdSe QDs by Linker-Assisted Assembly

β-$Pb_xV_2O_5$ nanowires (5 mg) were dispersed in DI H_2O (10 mL) in a 20 mL scintillation vial. The dispersion was sonicated for 20 min to maximize the amount of dispersed nanowires. An aqueous dispersion of as-synthesized Cys-CdSe QDs or MP-CdSe QDs (1 mL) was added to the dispersion of β-$Pb_xV_2O_5$ nanowires and allowed to equilibrate overnight (12-16 h). QD-functionalized nanowires were recovered *via* centrifugation, then rinsed with DI H_2O to remove excess QDs. CdSe-functionalized β-$Pb_xV_2O_5$ nanowires were dried at room temperature before characterization.

IV.2.6 Characterization Methods and Instrumentation

UV/Vis absorption spectra of dispersions of QDs were obtained with an Agilent 8453 diode array spectrophotometer. Dispersions of QDs were housed in a 1 cm cuvette. Scanning electron microscopy (SEM) was performed with a Hitachi SU-70 instrument operated at 5 kV and equipped with an energy dispersive X-ray spectroscopy detector. Samples were prepared for SEM by spreading powdered samples on carbon tape stubs; samples were then carbon coated to ensure a conductive contact to prevent charging. High-resolution transmission electron microscopy (HRTEM), selected area electron diffraction (SAED) measurements, and energy dispersive X-ray spectroscopy (EDS) were performed using a JEOL-2010 instrument operated at 200 kV with a beam current of 100 mA and a FEI TECNAI G2 F20 FE-TEM operated at 200 kV. Samples for HRTEM were prepared by dispersing functionalized β-$Pb_xV_2O_5$ nanowires in ethanol and depositing the dispersion onto a 300-mesh copper grid coated with amorphous carbon. The grid was then allowed to dry under ambient conditions. Raman spectra of solid-phase powders of uncoated and CdSe-coated β-$Pb_xV_2O_5$ nanowires were obtained with a Jobin-Yvon Horiba Labram HR800 instrument coupled to an Olympus BX41 microscope using the 514.5 nm laser excitation from an Ar-ion laser. The laser power at the sample was kept below 10 mW to minimize photooxidation. Hard X-ray photoemission spectroscopy (HAXPES) measurements of the solid heterostructures were performed at the National Institute of Standards and Technology (NIST) bending magnetic beamline X24 of the National Synchrotron Light Source of Brookhaven National Laboratory. Measurements were performed at a ca. 4 KeV photon energy with

a pass energy of 500 eV and a Gaussian instrumental broadening of 0.45 eV. The higher excitation of HAXPES circumvents serious charging issues that are common to UV and soft x-ray photoelectron spectroscopy.[149] We note that no evidence of charging was observed during our measurements. The HAXPES spectra are energy aligned to the Fermi level of a gold foil reference in electrical contact with our samples, unless stated otherwise. To mitigate further energy alignment shifts from beam drift the Au reference scans were measured before and after each spectrum.

IV.2.7 Photoluminescence Experiments

Photoluminescence measurements were performed on mixed dispersions containing Cys-CdSe QDs and either β-$Pb_xV_2O_5$ or V_2O_5 nanowires. Dispersions of nanowires were prepared by adding β-$Pb_xV_2O_5$ or V_2O_5 nanowires (1 mg) to DI H_2O (10 mL) and sonicating for 30 min. Fresh dispersions of Cys-CdSe QDs were synthesized (as described above) immediately before combining with nanowires. Mixed dispersions were prepared in septum-sealed cuvettes and consisted of dispersed Cys-CdSe QDs (0.1 mL), dispersed β-$Pb_xV_2O_5$ or V_2O_5 nanowires (0.25 mL), and DI H_2O (4.65 mL). A diluted dispersion of Cys-CdSe QDs (0.1 mL of purified Cys-CdSe QDs in 4.9 mL DI H_2O) was also prepared. Samples were purged with Ar for 5 min to minimize quenching of emission by dissolved O_2 (g). UV/Vis absorption spectra, steady-state emission spectra and time-resolved emission data were acquired approximately every 15 min during the first 3 h after the mixed dispersions were prepared, then approximately every 45 min for an additional 2.5 h. Steady-state emission spectra were obtained with a Varian Cary Eclipse fluorimeter with excitation at 365 nm. Time-resolved

photoluminescence (TRPL) data were obtained by time-correlated single-photon counting (TCSPC) with a Becker & Hickl Tau130 system with a 16-channel multi-anode photomultiplier tube (PML 16-C). A pulsed diode laser (BDL-440 SMC) excited the samples at 440 nm (20 MHz, 40-90 ps, 0.07-20 mJ). Data were acquired at magic angle conditions. TRPL decay traces were recorded in 4096 bins with a resolution of 12.2 ps over a time span of 50 ns. Instrument response function (IRF) was obtained by scattering the excitation beam with dispersed colloidal silica (Ludox). All TCSPC data were collected for 150 s. TRPL decay traces were fit using a global analysis involving multiexponential reconvolution.

IV.3 Results and Discussion

IV.3.1 β-$Pb_xV_2O_5$ Nanowires

In past work, we have reported the preparation of β-$Pb_xV_2O_5$ nanowires wherein the stereoactive $6s^2$ lone pair in the intercalating Pb^{2+} ion gives rise to "mid-gap" states derived primarily from Pb 6s—O 2p interactions that are antibonding in character.[48,49] Figure A. 3 shows the crystal structure of β-$Pb_xV_2O_5$ where Pb^{2+} cations reside within tunnels defined by a V_2O_5 framework constituted from parallel chains of [VO_6] and [VO_5] polyhedra. Powder X-ray diffraction and X-ray absorption and emission spectroscopy characterization of the nanowires along with detailed verification of the stoichiometry have been published in previous work.[48] The cations are highly ordered along the tunnel framework as indicated by the appearance of superlattice reflections in the powder diffraction patterns.[48]

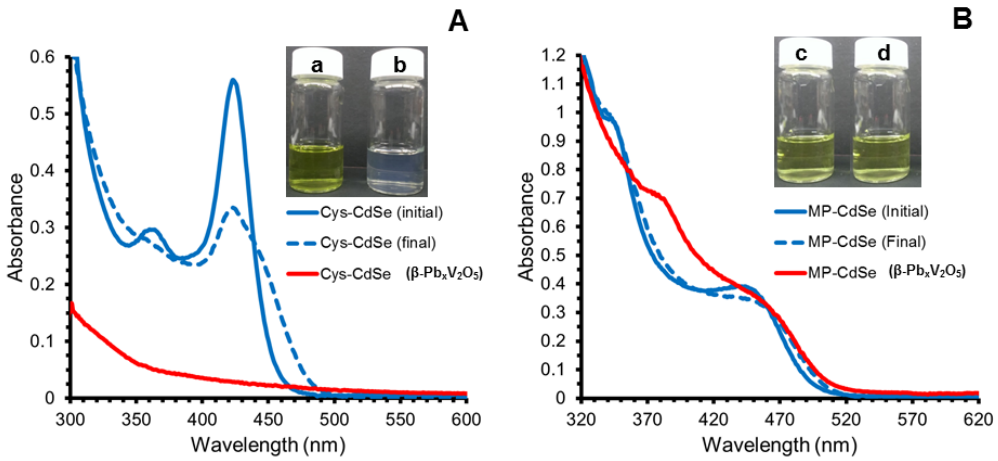

Figure IV. 1 UV-Vis absorption spectra of CdSe QDs initially after dispersion into DI H_2O (solid blue curves), of CdSe QDs after 12-16 h in DI H_2O (dashed blue curves), and of the supernatant recovered after removing by centrifugation β-$Pb_xV_2O_5$ nanowires that had equilibrated for 12-16 h with CdSe QDs (solid red curve); *insets:* digital photographs of dispersions of CdSe QDs before (a, c) and after (b, d) mixing with β-$Pb_xV_2O_5$ nanowires. Data in A) correspond to Cys-CdSe QDs; data in B) correspond to MP-CdSe QDs.

IV.3.2 Linker-Assisted Assembly of CdSe QDs onto Nanowires Surfaces

Water-dispersible Cys-CdSe and MP-CdSe QDs were synthesized for adsorption onto β-$Pb_xV_2O_5$ nanowires.[65,147,150] These QDs are attractive because (1) β-$Pb_xV_2O_5$ nanowires disperse well into water, (2) the synthesis is facile and relatively chemically benign (and thereby amenable to scaling), and (3) the QDs are synthesized with bifunctional linkers as the native capping ligands, avoiding the need for post-synthesis ligand exchange and providing a facile handle for attachment to the nanowire surfaces. The absorption spectrum of dispersed Cys-CdSe QDs is characterized by an intense and narrow band centered at 423 nm and a weaker but well-resolved band centered at 360

nm, corresponding to the first and second excitonic transitions, respectively (Figure IV. 1A). The spectrum was consistent with the spectrum reported by Park *et al.* for Cys-CdSe QDs prepared similarly.[145,146] The high energy and sharpness of the first excitonic band, as well as its large intensity relative to the second excitonic band, indicate the formation of CdSe QDs with diameters less than 2 nm.[151,152] The absorption spectrum of MP-CdSe QDs differed significantly (Figure IV. 1B). The spectrum was characterized by broader first and second excitonic absorption bands centered at approximately 434 and 349 nm, respectively. The first excitonic absorption band was less intense than the second. While these QDs do not have an ideal spectral overlap with the solar spectrum, they serve to demonstrate the feasibility of electronic coupling of QD valence band edges to mid-gap states of β-$Pb_xV_2O_5$. In addition, this method is broadly generalizable to Cys-CdSe QDs of a larger size with an absorption onset at 550 nm such as reported in our previous work.[150] Cysteinate(2-) (Cys) and mercaptopropionate (MP) differ only in the presence of the amine group of Cys at the alpha position relative to the carboxylate. We previously reported that coordination of the amine of Cys to Cd^{2+} influences precipitation-dissolution equilibria and the size and optical properties of CdSe QDs.[65,147]

As an initial approach to determine whether Cys-CdSe and/or MP-CdSe QDs attached to β-$Pb_xV_2O_5$ nanowires by linker-assisted assembly, we characterized dispersions of the QDs before and after exposure to the nanowires (Figure IV. 1). Dispersions of Cys-CdSe QDs and β-$Pb_xV_2O_5$ nanowires were combined and allowed to equilibrate; subsequently, the nanowires were removed by centrifugation. The resulting supernatant was colorless, and its absorption spectrum exhibited no measurable excitonic

absorption bands characteristic of Cys-CdSe QDs. The absence of Cys-CdSe QDs in the supernatant indicates that the QDs adhered to the surface of the β-$Pb_xV_2O_5$ nanowires. Importantly, dispersions of Cys-CdSe QDs that were not exposed to β-$Pb_xV_2O_5$ nanowires retained their yellow coloration, and absorption spectra of these dispersions exhibited well-resolved first and second excitonic absorption bands (Figure IV. 1A). The diminution and red-shift of the first excitonic absorption band of the Cys-CdSe QDs that were not exposed to β-$Pb_xV_2O_5$ nanowires arose from a slow growth mechanism that we have reported previously.[65]

In contrast, the addition of β-$Pb_xV_2O_5$ nanowires to dispersions of MP-CdSe QDs resulted in little or no attachment of QDs to the nanowires, as evidenced by the lack of change in color of dispersions of QDs recovered after mixing with β-$Pb_xV_2O_5$ (inset to Figure IV. 1B) and the persistence of excitonic absorption bands in the spectra of such dispersions. An increase in the absorbance of MP-QDs that had been mixed with β-$Pb_xV_2O_5$ nanowires has been observed at wavelengths less than 440 nm. This increase in absorbance is most likely due to absorption by β-$Pb_xV_2O_5$ nanowires remaining in suspension following centrifugation. Absorption spectra of dispersions of MP-CdSe QD that are not exposed to β-$Pb_xV_2O_5$ nanowires changed only minimally over 12-16 h.

SEM images have been acquired of β-$Pb_xV_2O_5$ nanowires following immersion in dispersions of Cys-CdSe or MP-CdSe QDs (Figure IV. 2 and Figure A. 4). The β-$Pb_xV_2O_5$ nanowires that are exposed to MP-CdSe QDs are unchanged relative to as-synthesized nanowires (Figure A. 4). In contrast, agglomerated Cys-CdSe QDs are discernible on the surfaces of β-$Pb_xV_2O_5$ nanowires yielding a very different

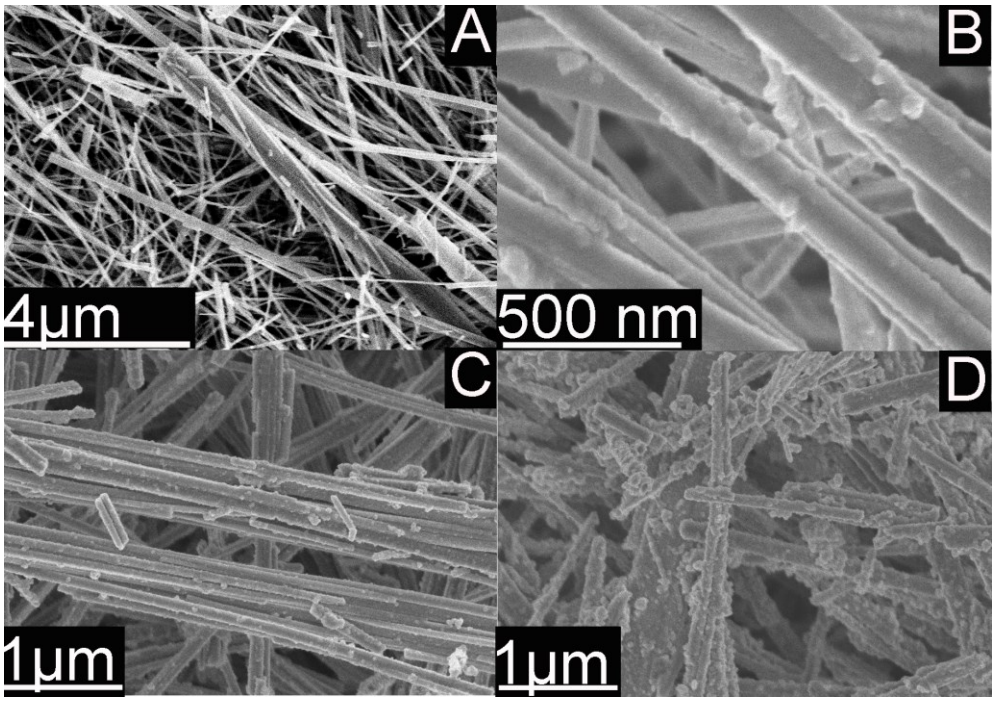

Figure IV. 2 SEM images of uncoated β-$Pb_xV_2O_5$ nanowires (A) and β-$Pb_xV_2O_5$ nanowires coated with CdSe *via* immersion for 12-16 h in aqueous solutions of Cys-CdSe QDs (B), and *via* three SILAR cycles (C) and five SILAR cycles (D).

morphology as compared to uncoated β-$Pb_xV_2O_5$ nanowires. Owing to the small particle size of the QDs, we were unable to resolve individual QDs on the surfaces of nanowires. However, energy dispersive X-ray spectroscopy (EDS) data have been acquired for β-$Pb_xV_2O_5$ nanowires after mixing with either Cys-CdSe or MP-CdSe QDs. Ensemble EDS studies of the nanowires confirms the presence of Cd and Se on the nanowires immersed in aqueous solutions of Cys-CdSe QDs (Figure A. 5). Average relative amounts of Cd, Se, Pb, and V have been calculated from five spectra, suggesting an apparent molecular formula of $Cd_{(0.09 \pm 0.03)}Se_{(0.06 \pm 0.01)}Pb_{(0.27 \pm 0.01)}V_2O_5$ for the nanowires coated with Cys-CdSe QDs. The excess of cadmium relative to selenium is consistent

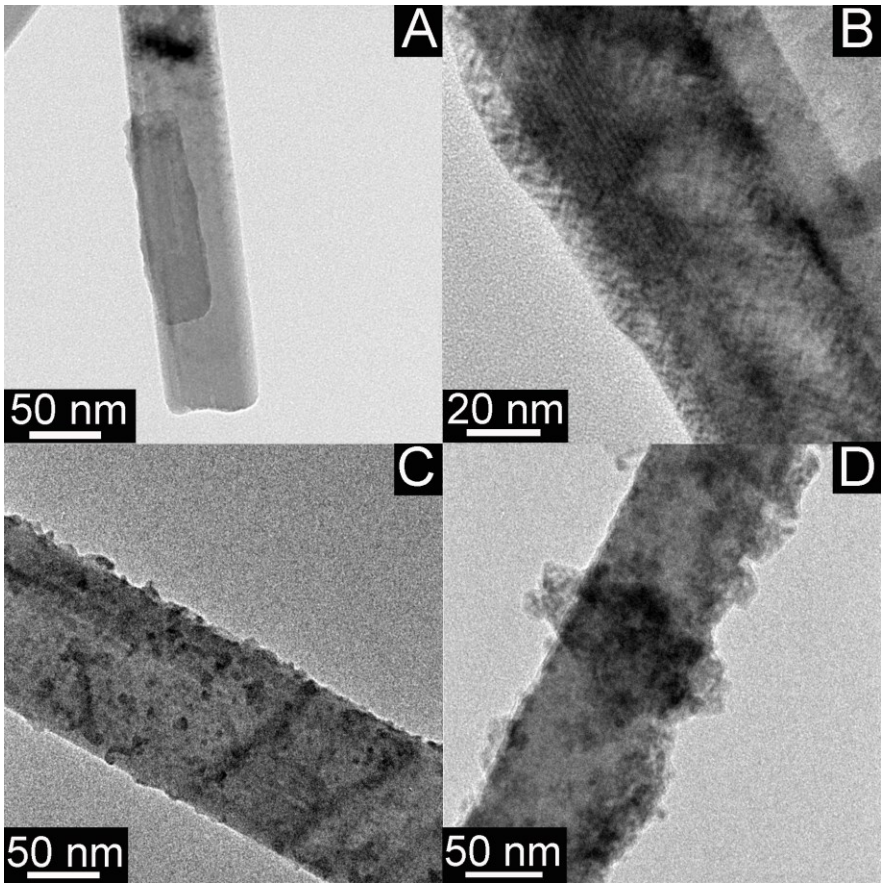

Figure IV. 3 TEM images of an uncoated β-$Pb_xV_2O_5$ nanowire (A) and β-$Pb_xV_2O_5$ nanowires coated with CdSe *via* immersion for 12-16 h in aqueous solutions of Cys-CdSe QDs (B), and *via* three SILAR cycles (C) and five SILAR cycles (D).

with our prior elemental analysis of Cys-CdSe QDs.[147] EDS spectra of β-$Pb_xV_2O_5$ nanowires after mixing with MP-CdSe QDs (Figure A. 6) showed no evidence of Cd or Se.

As further characterization of the heterostructures, TEM images have been acquired for β-$Pb_xV_2O_5$ nanowires before and after mixing with Cys-CdSe QDs (Figure IV. 3A and B). The unfunctionalized β-$Pb_xV_2O_5$ nanowire shows a smooth, uniform

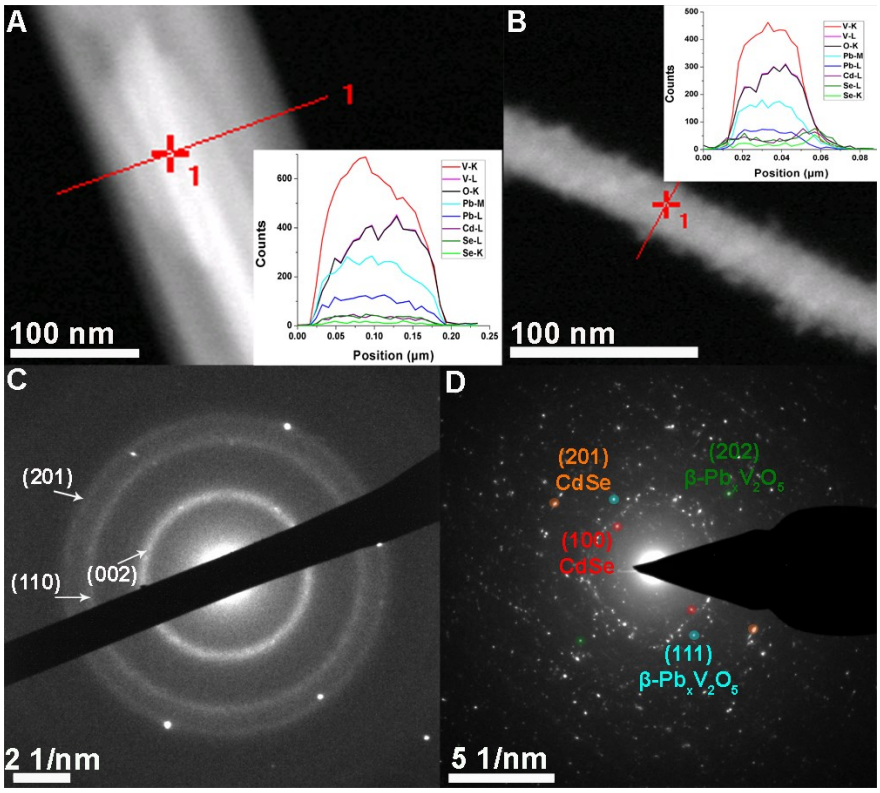

Figure IV. 4 TEM images and corresponding EDS linescans (insets) acquired for β-$Pb_xV_2O_5$ nanowires coated with CdSe *via* immersion for 12-16 h in aqueous solutions of Cys-CdSe QDs (A), and upon deposition of CdSe QDs by three SILAR cycles (B). SAED pattern acquired for a CdSe QD agglomerate deposited *via* SILAR protruding from the nanowire surface (C) and of β-$Pb_xV_2O_5$ nanowires coated with CdSe *via* three SILAR cycles (D).

surface morphology, whereas the Cys-CdSe QD-coated β-$Pb_xV_2O_5$ nanowire exhibited a rougher, speckled surface morphology. A well-defined overlayer of CdSe is visible on the top-most surface of nanowire, obscuring the view of lattice planes of the underlying β-$Pb_xV_2O_5$ nanowires. No modification of the surfaces of nanowires is discernible upon mixing the β-$Pb_xV_2O_5$ nanowires with MP-CdSe QDs (Figure A. 4). Figure IV. 4A further depicts EDS linescans acquired along the width of an individual nanowire

reacted with Cys-CdSe, clearly indicating the presence of Cd and Se across the nanowire. Taken together, absorption spectra, SEM images, TEM images, and EDS linescans reveal that Cys-CdSe QDs adhere to β-$Pb_xV_2O_5$ nanowires, whereas MP-CdSe QDs do not attach to a similar extent. Cys contains three functional groups (thiolate, carboxylate, and amine) that may be involved in adsorption to either CdSe QDs or β-$Pb_xV_2O_5$ nanowires, whereas MP contains two of these moieties (thiolate and carboxylate). Under the basic reaction conditions in which Cys-CdSe QDs are synthesized (pH of approximately 13), all three functional groups are deprotonated.[153] Our prior vibrational spectroscopic analysis of the molecular linkage between Cys-CdSe QDs and TiO_2 thin films revealed that the thiolate coordinated to Cd^{2+} surface sites on QDs and the carboxylate coordinated to Ti^{4+} surface sites of TiO_2. Deprotonated amines of Cys were predominately coordinated to CdSe QDs.[147] The dramatic difference in the affinities of Cys-CdSe and MP-CdSe QDs for β-$Pb_xV_2O_5$ nanowires implies that the amine group of Cys played a crucial role in adsorption to the surface of β-$Pb_xV_2O_5$ nanowires. Previous self-assembly studies on the adsorption of V_2O_5 nanowires to substrates have revealed that the negatively-charged, hydroxylated surfaces of V_2O_5 nanowires can adsorb to surfaces functionalized with positively-charged protonated amines through electrostatic interactions.[154–156] Our Cys-CdSe QDs used for linker-assisted assembly were twice rinsed with DI H_2O then redispersed into DI H_2O, yielding Cys-CdSe dispersions with pH values between 8.5 and 9.0, lower than the pK_a of the amine group of Cys.[147] Therefore, the dispersions of Cys-CdSe QDs used for adsorption experiments had available protonated amines for electrostatic interaction with β-$Pb_xV_2O_5$

nanowires. Despite the complexities associated with adsorption-desorption equilibria of the amine at the surfaces of both CdSe and β-$Pb_xV_2O_5$, we posit that protonated amines of cysteinate(-) or cysteine interacted electrostatically with negatively-charged surfaces of β-$Pb_xV_2O_5$ nanowires, resulting in the attachment of Cys-CdSe QDs to the nanowires. The lack of affinity of MP-CdSe QDs for β-$Pb_xV_2O_5$ nanowires supports this mechanism.

IV.3.3 SILAR Deposition of QDs onto Nanowire Surfaces

β-$Pb_xV_2O_5$ nanowires have further been functionalized with nanostructured CdSe through one to five SILAR deposition cycles with the goal of varying the thickness of the CdSe layer. The resulting materials have been characterized by SEM and TEM as indicated by Figures IV. 2 and IV. 3 as well as Figure A. 7. Uncoated nanowires are characterized by smooth faceted surfaces. Individual CdSe QDs are not discernible by SEM after one cycle of SILAR deposition, although EDS analysis suggests the presence of Cd and Se on the surfaces of nanowires (Figures A. 7 and A. 8). The surface morphology of β-$Pb_xV_2O_5$ nanowires exposed to increasing numbers of SILAR cycles becomes progressively rougher; the presence of nanostructured CdSe and/or agglomerates is readily discernible on β-$Pb_xV_2O_5$ nanowires after three cycles of SILAR. Samples subjected to five SILAR cycles appear to be completely and continuously coated with CdSe QDs (Figures IV. 2D and IV. 3D).

Discrete CdSe QDs can be resolved at low fractional surface coverages upon deposition for one or two SILAR cycles (Figure A. 7). With increasing number of SILAR cycles, more CdSe QDs are present on the nanowire surfaces as observed in

Figure IV. 3C for nanowires exposed to three SILAR cycles where an almost continuous overlayer of individual CdSe QDs is observed on the nanowire surfaces. After five SILAR cycles, Figure IV. 3D indicates the presence of agglomerates of QDs. The electron microscopy images thus clearly demonstrate that SILAR allows for tunability of the density and coverage of QDs on the surfaces of β-$Pb_xV_2O_5$ nanowires as a function of the number of cycles. On the basis of imaging β-$Pb_xV_2O_5$ nanowires coated with one or two SILAR cycles, it is likely that the QDs are heterogeneously nucleated onto the nanowire surfaces (Figure A. 7). Figure IV. 4B further depicts an EDS linescan acquired along the width of an individual β-$Pb_xV_2O_5$ nanowire treated with three SILAR cycles illustrating the presence of both cadmium and selenium across the entire cross-section of the nanowire. After five SILAR cycles, a complete core-shell structure is seen, as indicated by the presence of cadmium and selenium on both sides of the nanowire as well as across the wire (Figure A. 9).

In addition, SAED analysis has been performed for both agglomerations of CdSe QDs protruding from the nanowires (without obscuration from reflections from the underlying β-$Pb_xV_2O_5$ nanowires) and the CdSe-coated β-$Pb_xV_2O_5$ heterostructures subjected to three SILAR cycles (Figure IV. 4C, D). Diffuse rings are observed for the QDs alone, consistent with the polycrystalline nature of the CdSe. The SAED pattern can be indexed to the wurtzite phase of cadmium selenide (JCPDS # 08-0459), providing definitive phase identification of the crystalline CdSe coating grown onto the nanowires by SILAR. The SAED pattern acquired for the heterostructure is more complex given the contributions from both components. However, several of the reflections can be

indexed to the wurtzite phase of CdSe (JCPDS # 08-0459), whereas others can be indexed to β-$Pb_{0.304}V_2O_5$ (JCPDS #41-1426) as depicted in Figure IV. 4D.[48] The lattice spacings of the β-$Pb_xV_2O_5$ nanowires deduced from the SAED pattern are not substantially altered upon SILAR deposition of the QDs, which is also consistent with Raman data discussed below. The EDS and SAED data depicted in Figure IV. 4 thus provide unequivocal determination of the growth of CdSe QDs stabilized in the wurtzite phase on the nanowire surfaces.

To further verify the crystal structure of the overlayer deposited by SILAR and to examine the influence of SILAR deposition on the oxide lattice, the heterostructures have been characterized by Raman spectroscopy (Figure IV. 5). The Raman spectrum of uncoated as-prepared β-$Pb_xV_2O_5$ nanowires is characterized by bands arising from phonon modes involving bond-bending and chaining of the V_2O_5 framework below 500 cm^{-1} and bond-stretching of the framework above 500 cm^{-1}.[157] The low-frequency modes around 175 cm^{-1} correspond to external motions of [VO_5] and [VO_6] polyhedra wherein these units are collectively displaced with respect to each other.[9,144] In contrast, the band at 951 cm^{-1} likely derives from the V—O stretching mode localized within the [VO_5] square pyramids of β-$Pb_xV_2O_5$.[9,144] Both sets of modes serve as sensitive probes for cation stoichiometry and lattice distortion. [9,144] It is thus notable that these bands do not shift upon SILAR deposition, indicating that the formation of a CdSe QD overlayer does not significantly distort the underlying oxide lattice (which is further consistent with the SAED findings noted above). The Raman spectra acquired upon SILAR deposition of CdSe onto the nanowires do indicate the emergence of a pronounced band at 200 cm^{-1}.

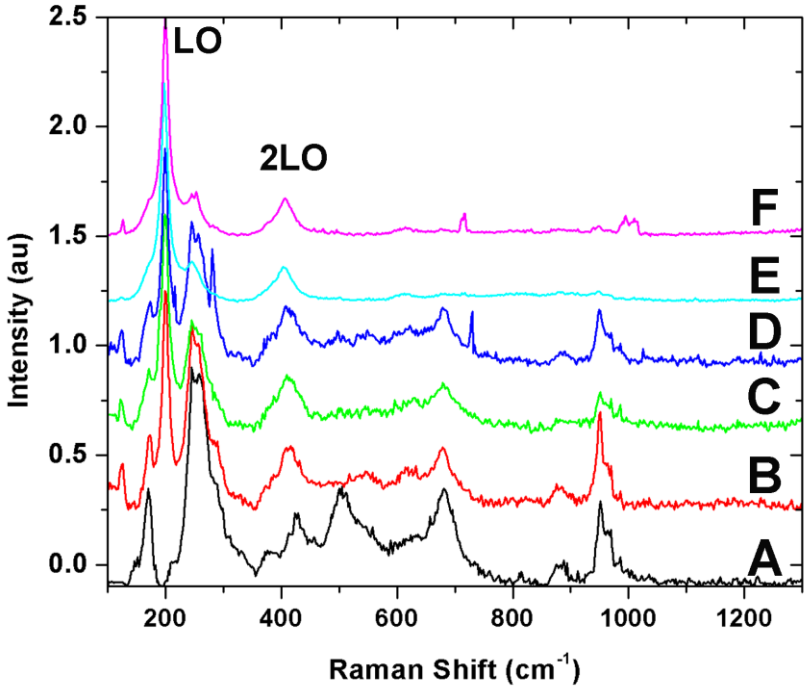

Figure IV. 5 Raman spectra of uncoated β-$Pb_xV_2O_5$ nanowires (A) and β-$Pb_xV_2O_5$ nanowires coated with CdSe *via* one SILAR cycle (B), two SILAR cycles (C), three SILAR cycles (D), four SILAR cycles (E), and five SILAR cycles (F).

This mode and an overtone at 407 cm^{-1} gradually increase in intensity such that, for the samples subjected to four or five SILAR cycles, they dwarf the Raman signals from β-$Pb_xV_2O_5$. The emergent Raman bands at 200 and 407 cm^{-1} can be assigned to the bulk longitudinal optic (LO) mode of wurtzite CdSe and its second-order overtone (2LO), respectively. [158,159] The 2LO band at 407 cm^{-1} initially overlaps with the 425 cm^{-1} mode of β-$Pb_xV_2O_5$ but grows dramatically in intensity with increased number of SILAR cycles. With laser excitation at 514.5 nm, resonance enhancement of a fraction of the QDs may contribute to the strong intensities that are observed. In summary, the Raman spectra provide additional evidence that SILAR yields wurtzite-structured CdSe on the

β-$Pb_xV_2O_5$ nanowires, the amount of CdSe monotonically increases with the number of SILAR cycles, and the underlying oxide lattice does not appear to be substantially distorted upon coating with CdSe QDs.

IV.3.4 Electronic Structure of CdSe/β-$Pb_xV_2O_5$ Interfaces by Hard X-ray Photoemission Spectroscopy (HAXPES)

Figure IV. 6 shows the core-levels, O 1s, V 2p, Cd 3d, and Pb 4d core regions of the HAXPES spectra acquired for β-$Pb_xV_2O_5$ nanowires functionalized with CdSe by SILAR (along with the corresponding spectrum for reference undoped V_2O_5 nanorods). Figure A. 10 depicts the corresponding spectra for heterostructures prepared by the linker-assisted route. All the spectra shown in Figure IV. 6 (and Figure A. 10) have been aligned to the main O 1s peak (529.8 eV) of the V_2O_5 reference to account for Fermi level shifts that may complicate chemical assignments. The broad feature observed at ca. 412.5 eV for the unfunctionalized β-$Pb_{0.33}V_2O_5$ nanowires corresponds to the Pb $4d_{5/2}$ emission and has a chemical shift value similar to most lead oxide species. Deposition of CdSe onto the nanowires by SILAR or linker-assisted assembly gives rise to Cd $3d_{5/2}$ and $Cd3d_{3/2}$ emission features at 405 and 413 eV, respectively, with the latter being closely overlapped with the Pb 4d emission. The intensities of the Cd 3d core-level features are comparable for the one-cycle SILAR and linker-assisted Cys-CdSe/β-$Pb_{0.33}V_2O_5$ heterostructures, consistent with the notion of discrete CdSe QDs dispersed along the nanowire surfaces observed by electron microscopy (Figures IV. 2 and IV. 3). Increasing the number of SILAR cycles clearly brings about an increase in the intensity of the Cd 3d core-level features. HAXPES measurements do not distinguish between

samples coated by three or five SILAR cycles since a continuous overlayer is constituted around the nanowires with three cycles and it is primarily the overlayer that is being probed in the measurement.

The corresponding O 1*s* and V 2*p* core-level HAXPES spectra in Figure IV. 6 indicate that the one cycle SILAR sample is characterized by some surface oxidation of the Cd to CdO (peak at 534 eV). Interestingly, no such surface oxidation is observed for the linker-attached CdSe QDs wherein the surfaces are passivated by Cys (Figure A. 10) or for SILAR-functionalized samples with increasing number of cycles. The V $2p_{3/2}$ core-level spectra indicate the mixed-valence (V^{5+} and V^{4+}) nature of vanadium atoms in

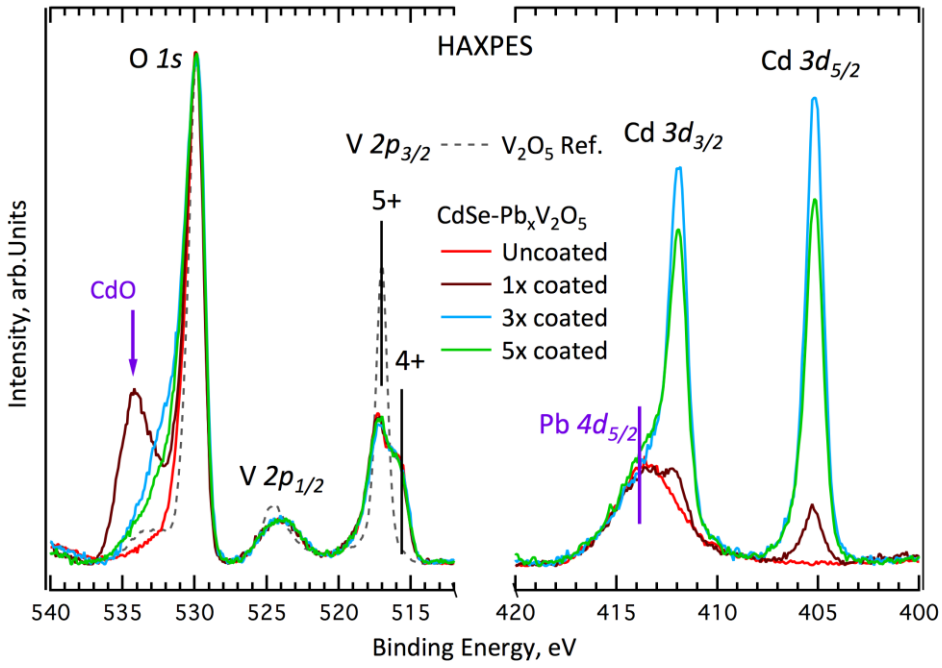

Figure IV. 6 HAXPES spectra obtained for SILAR functionalized β-$Pb_xV_2O_5$ nanowires contrasted with spectra acquired for V_2O_5 and as-prepared (unfunctionalized) β-$Pb_xV_2O_5$ nanowires.

the system and suggest that functionalization with CdSe does not greatly alter the ratio of vanadium oxidation states.[49]

Figure IV. 7 displays the valence band spectra acquired for these samples, which are aligned to their Fermi levels. To highlight the evolution of the electronic structure, all the valence band spectra have been normalized to the background and their intensities scaled to the O 2p non-bonding state. As a result, the accompanying difference spectra can be used to identify the emergence of new features. As detailed in previous studies of β-$Pb_{0.33}V_2O_5$ nanowires,[49] the valence band region is characterized by a broad band between 2 and 9 eV and includes an O 2*p* non-bonding peak at ca. 5 eV and a V—O bonding peak at ca. 7 eV; these assignments are analogous to the spectra calculated and experimentally measured for V_2O_5.[126] In addition, a feature at ca. 9.5 eV has been assigned to a Pb 6s—O 2p bonding interaction that is observed for β-$Pb_{0.33}V_2O_5$ nanowires but not for V_2O_5. The related anti-bonding Pb 6s—O 2p interaction is observed as a shoulder centered at ca. 2 eV and constitutes the "in gap" or "mid-gap" state that was first predicted in density functional theory calculations of β-$Pb_{0.33}V_2O_5$.[48,49] The bonding and antibonding states are highlighted by the difference spectra between the β-$Pb_{0.33}V_2O_5$ and V_2O_5 shown in Figure IV. 7. The mid-gap state raises the topmost filled states by 0.8 eV above the valence band maximum of V_2O_5. With the attachment of CdSe QDs by linker-assisted assembly (Figure A. 10) or SILAR (Figure IV. 7), spectral weight is added to the 1.6—4 eV region that is most prominent with the highest amounts of CdSe coverage, corresponding to the topmost valence band

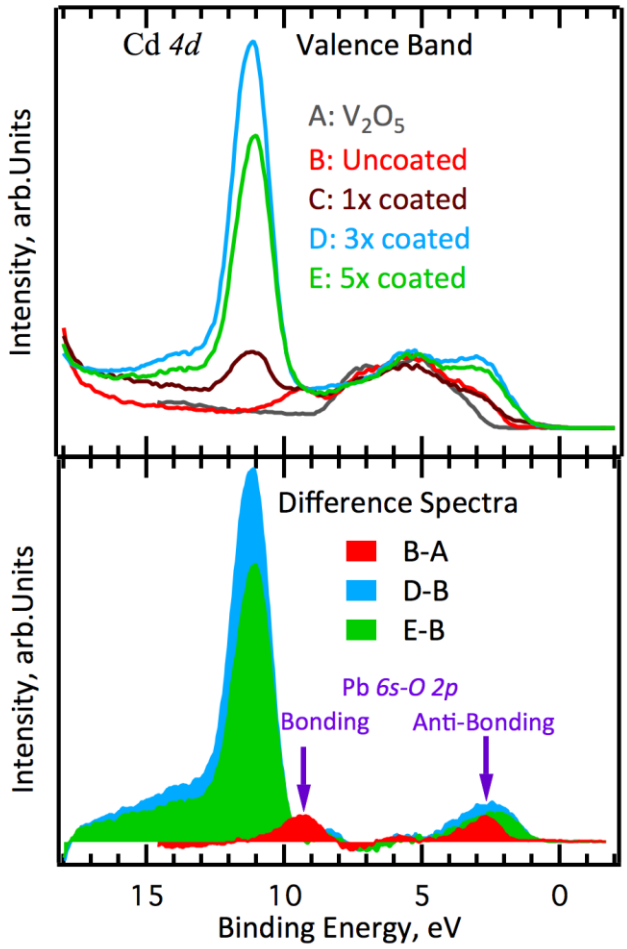

Figure IV. 7 Valence band spectra for functionalized β-$Pb_xV_2O_5$ nanowires contrasted with spectra acquired for V_2O_5 and as-prepared (unfunctionalized) β-$Pb_xV_2O_5$ nanowires. The top panel indicates the valence band spectra, whereas the bottom panel depicts difference spectra.

region of CdSe. Difference spectra reveal that that the Cd 4s derived valence band edge is overlapped with the mid-gap states in β-$Pb_{0.33}V_2O_5$, suggesting the possibility for transfer of electrons from the mid-gap states of the β-$Pb_{0.33}V_2O_5$ nanowires to the valence bands of putative photoexcited CdSe QDs, or equivalently for the transfer of

photogenerated holes from CdSe to mid-gap states of β-$Pb_{0.33}V_2O_5$. The broad size distribution of SILAR-deposited QDs likely leads to the relatively broad Se 4p-derived-valence band observed here.

IV.3.5 Photoluminescence and Charge Transfer

As an initial approach to investigate the excited-state charge-transfer reactivity of our heterostructures, we have measured steady-state and time-resolved emission from Cys-CdSe QDs in the presence of β-$Pb_xV_2O_5$ nanowires. The experiments involve combining aqueous dispersions of Cys-CdSe QDs and β-$Pb_xV_2O_5$ nanowires and acquiring absorption and emission spectra as a function of elapsed time. There are several different mechanisms for photoluminescence quenching that can occur and in order to elucidate the quenching processes, mixed dispersions of Cys-CdSe QDs with V_2O_5 nanowires, as well as dispersions of Cys-CdSe QDs alone, have been characterized as controls. The latter set of control experiments performed in tandem with experiments of nanowire/QD dispersions allows us to control for evolution of the optical properties of the Cys-CdSe QDs as a function of time. Importantly, EDS data reveals the presence of Cd and Se on V_2O_5 nanowires isolated from mixed dispersions prepared under identical conditions as the fully-characterized Cys-CdSe/β-$Pb_xV_2O_5$ heterostructures (Figure A. 11); thus indicating that Cys-CdSe QDs can be attached to the surfaces of V_2O_5 nanowires. We and others have characterized charge transfer at various QD-molecule-semiconductor interfaces formed *in situ* within mixed dispersions.[136,160–163] The approach enables the facile preparation of materials interfaces within optically transparent mixtures that are suitable for spectroscopy.

The first excitonic absorption band of diluted dispersions of Cys-CdSe QDs diminished and red-shifted slightly with reaction time (Figure A. 12), as described above. The absorption spectrum was otherwise unchanged when Cys-CdSe QDs were mixed with β-$Pb_xV_2O_5$ or V_2O_5 nanowires (Figure IV. 8). The steady-state emission spectrum of free Cys-CdSe QDs contained a broad trap-state emission band centered at approximately 575 nm, consistent with our reported measurements.[147] This band intensified by approximately 18% within the first hour after the QDs were redispersed into DI H_2O and then equilibrated. Despite surface passivation with cysteinate ligands, the synthesized Cys-CdSe QDs display a significant amount of trap-state emission with no appreciable band edge emission. These QDs exhibit a quantum yield of 6.3% (±0.7%). Significant trap-state emission is reasonably expected with such small QDs because of larger surface/volume ratios.[164] Enhanced trap-state emission is common for QDs with shorter, less bulky, capping ligands.[165] When Cys-CdSe QDs were mixed with V_2O_5 nanowires, the trap-state emission band was initially unchanged relative to that of free Cys-CdSe QDs; the intensity at the band maximum then decreased by approximately 25% throughout the 5.5-h duration of our experiments. In contrast, when Cys-CdSe QDs were mixed with β-$Pb_xV_2O_5$ nanowires, the trap-state emission from Cys-CdSe QDs was quenched much more significantly at all reaction times. Within the first 15 min after preparing the mixed dispersions, the trap-state emission was quenched by approximately 22% relative to that of free Cys-CdSe QDs. After 5.5 h, the emission was quenched by nearly 50%. The increased quenching of emission with reaction time, for samples containing either β-$Pb_xV_2O_5$ or V_2O_5 nanowires, likely reflects the

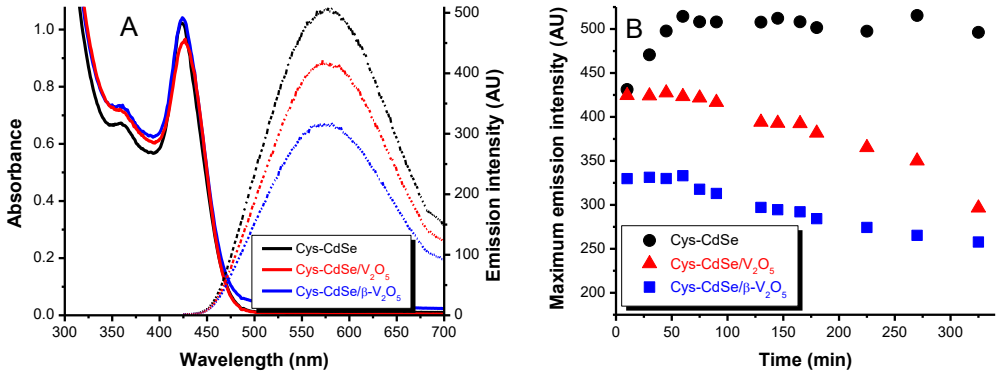

Figure IV. 8 Absorption (solid) and emission (dashed) spectra (A) and intensity of emission at the trap-state band maximum (575 nm) (B) of Cys-CdSe QDs, mixed dispersions of Cys-CdSe QDs and β-$Pb_xV_2O_5$ nanowires, and mixed dispersions of Cys-CdSe QDs and V_2O_5 nanowires. Spectra in A were acquired approximately 75 min after samples were prepared.

increasing electronic coupling of Cys-CdSe QDs with the nanowires *via* linker-assisted assembly. When averaged over the ten emission spectra acquired from 60 to 325 min (at reaction times after the emission band of free Cys-CdSe QDs had equilibrated), the trap-state emission from Cys-CdSe QDs was quenched (1.8 ± 0.3)-fold more by β-$Pb_xV_2O_5$ nanowires than by V_2O_5 nanowires, clearly indicating greater electronic coupling of the QDs to the former. Deep trap state emission of CdSe QDs is thought to be derived from the recombination of electrons in surface-localized selenide vacancies with valence band holes.[164–168] Therefore, the observed dynamic quenching of trap-state emission is nonetheless consistent with the transfer of holes derived from the valence band.

Time-resolved emission experiments were performed to gain further insight into the enhanced quenching of emission by β-$Pb_xV_2O_5$ nanowires. Emission decay traces were acquired following 440-nm pulsed excitation of dispersed Cys-CdSe QDs, mixed

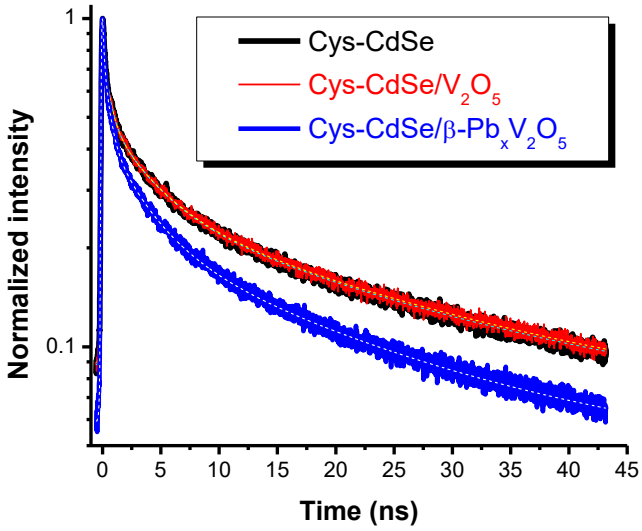

Figure IV. 9 Normalized time-resolved emission decay traces for Cys-CdSe QDs, mixed dispersions of Cys-CdSe QDs and β-$Pb_xV_2O_5$ nanowires, and mixed dispersions of Cys-CdSe QDs and V_2O_5 nanowires; dashed lines superimposed on the data are triexponential fits from global analysis. Data were acquired over a ~12.5-nm range of emission wavelengths centered near the trap-state emission maximum with 440-nm excitation. These decay traces were acquired 75 min after the samples were prepared.

dispersions of Cys-CdSe QDs and β-$Pb_xV_2O_5$ nanowires, and mixed dispersions of Cys-CdSe QDs and V_2O_5 nanowires as a function of elapsed time from the preparation of samples (Figures IV. 9 and A. 13). Emission decay traces were acquired simultaneously in sixteen channels spanning a 200-nm range centered near the maximum of the trap-state emission band. Emission from free Cys-CdSe QDs decayed multiexponentially, as evidenced by the nonlinearity of decay traces with logarithmic intensity axes. QDs often exhibit multiexponential emission decay kinetics, due to distributions of electron and hole trap states and multiple trap-state recombination mechanisms.[160,169–172] A global

fitting analysis revealed that the data for free Cys-CdSe QDs were modeled precisely by triexponential kinetics. Fitting parameters are compiled in Table A 2. Fitting parameters averaged over all reaction times from 60 to 325 min, after the steady-state emission spectrum of free Cys-CdSe QDs had equilibrated, are presented in Table IV. 1. The decay of trap-state emission from free Cys-CdSe QDs was dominated by the longest component with averaged lifetime ($\tau_{3,ave}$) of (26 ± 1) ns and averaged fractional emission intensity ($f_{3,ave}$) of 0.819 ± 0.009. The averaged intensity-weighted average lifetime ($<\tau>_{ave}$) was (22 ± 1) ns. Trap-state emission decayed more rapidly when Cys-CdSe QDs were combined with V_2O_5 nanowires. The value of $<\tau>_{ave}$ was (19 ± 1) ns; the accelerated decay arose primarily from a decrease of $\tau_{3,ave}$ to (23 ± 1) ns. The decay of trap-state emission was accelerated to an even greater extent when Cys-CdSe QDs were combined with β-$Pb_xV_2O_5$ nanowires. The value of $<\tau>_{ave}$ decreased to (16.6 ± 0.2) ns, owing to a decrease of $\tau_{3,ave}$ to (20.8 ± 0.3) ns and increases of the averaged fractional emission intensities of the faster components ($f_{1,ave}$ and $f_{2,ave}$).

The enhanced quenching of emission from Cys-CdSe QDs by β-$Pb_xV_2O_5$ nanowires, beyond the quenching by V_2O_5 nanowires, was dynamic, consistent with charge-transfer quenching and is readily apparent from even a qualitative evaluation of the decay profiles in Figure IV. 9. To a first approximation, the two types of nanowire differ only in the presence or absence of intercalated Pb^{2+} cations and the resulting mid-gap states, which overlap in energy with valence-band states of CdSe. Therefore, we assign the enhanced dynamic emission quenching by β-$Pb_xV_2O_5$ nanowires to the transfer of photogenerated holes from the valence band and/or trap states of Cys-CdSe

Table IV. 1. Averaged fitting parameters from global analysis of time-resolved emission decay data.

Sample	$\langle\tau\rangle_{ave}$ (ns) [a]	$\tau_{1,ave}$ (ns)	$f_{1,ave}$ (%) [b]	$\tau_{2,ave}$ (ns)	$f_{2,ave}$ (%) [b]	$\tau_{3,ave}$ (ns)	$f_{3,ave}$ (%) [b]
Cys-CdSe	22 ± 1	0.51 ± 0.01	3.1 ± 0.1	3.82 ± 0.08	15.1 ± 0.4	26 ± 1	81.9 ± 0.9
Cys-CdSe/V_2O_5	19 ± 1	0.48 ± 0.02	3.9 ± 0.5	3.5 ± 0.2	17 ± 1	23 ± 1	81 ± 4
Cys-CdSe/β-$Pb_xV_2O_5$	16.6 ± 0.2	0.47 ± 0.01	4.6 ± 0.1	3.32 ± 0.06	18.4 ± 0.2	20.8 ± 0.3	77.0 ± 0.3

$$\langle\tau\rangle=\Sigma_n(A_n\tau_n^2)/\ \Sigma_n(A_n\tau_n) \quad \text{(VI.1)}$$

where A_n and τ_n are preexponential factors and lifetimes, respectively, from triexponential fits;

$$f_n(\%)=[A_n\tau_n/\ \Sigma_n(A_n\tau_n)]x100 \quad \text{(VI.2)}$$

All fitting parameters are averaged from global analysis of ten emission decay data sets acquired at elapsed times from 60 to 325 min after samples were prepared; standard deviations are relative to the average values.

QDs to the mid-gap states of β-$Pb_xV_2O_5$ nanowires. It is important to note that overlap of the conduction band of CdSe QDs with the conduction band of β-$Pb_xV_2O_5$ can also potentially lead to electron transfer. However, the control experiments with V_2O_5 nanowires that have a similarly positioned conduction band but lack the intercalating cation provide substantial credence to the role of the primary electronic coupling within this system being between the valence band edges of the QDs and the mid-gap states of the β-$Pb_xV_2O_5$ nanowires. Inspection of the decay traces in Figure IV. 9 clearly illustrate

that the free Cys-CdSe QDs and the Cys-CdSe QDs mixed with V_2O_5 had very similar decay profiles indicating no charge transfer in the absence of optimally positioned mid-gap states. The rate constant for hole transfer (k_{ht}) was estimated from values of $<\tau>_{ave}$:[161,173]

$$k_{ht}=[1/<\tau>_{ave}(CdSe/\beta\text{-}Pb_xV_2O_5)]- [1/<\tau>_{ave}(CdSe/V_2O_5)] \quad (IV.3)$$

where $<\tau>_{ave}(CdSe/\ \beta\text{-}Pb_xV_2O_5)$ and $<\tau>_{ave}(CdSe/\ V_2O_5)$ are values of $<\tau>_{ave}$ for mixed dispersions of Cys-CdSe QDs with β-$Pb_xV_2O_5$ nanowires and V_2O_5 nanowires, respectively. This analysis is predicated on the assumptions (1) that the rate constants of all processes that compete with hole transfer are unchanged for Cys-CdSe QDs in the presence of β-$Pb_xV_2O_5$ nanowires relative to V_2O_5 nanowires and (2) that hole transfer is the only additional excited-state deactivation pathway that is active for Cys-CdSe/β-$Pb_xV_2O_5$ heterostructures. The calculation yielded a k_{ht} value of $(8 \pm 4) \times 10^6\ s^{-1}$, which is 2-3 orders of magnitude less than recently-reported rate constants for transfer of holes from the valence band of CdSe QDs to p-type semiconductor electrodes[174,175] but similar to reported rate constants for interfacial electron transfer from trap states of QDs to dispersed semiconductor nanoparticles.[160,161] We cannot discount the possibility that differences in the emission-decay kinetics of Cys-CdSe QDs in the presence of β-$Pb_xV_2O_5$ nanowires relative to V_2O_5 nanowires arose from differences in the kinetics of linker-assisted assembly or the amount of QDs on the nanowires during the 5.5-h duration of our emission experiments. However, such differences are unlikely given that the nanowires differed only the presence or absence of intercalated Pb^{2+} cations. The

combination of increased steady-state and dynamic quenching of CdSe emission by β-$Pb_xV_2O_5$ nanowires in contrast to V_2O_5 nanowires that lack the intercalating Pb^{2+} cation makes a strong case for hole transfer from the photoexcited QDs to the mid-gap states of the oxide nanowires.

IV.4 Conclusion

We have functionalized β-$Pb_xV_2O_5$ nanowires with CdSe QDs using linker-assisted assembly and SILAR. Cys-CdSe QDs adhered to β-$Pb_xV_2O_5$ nanowires but MP-CdSe QDs did not, suggesting that the protonated amine of cysteinate(-) or cysteine played a role in the likely electrostatic attachment of the QDs to the nanowires. One-to-two SILAR cycles yielded discrete CdSe QDs on the surfaces of β-$Pb_xV_2O_5$ nanowires, whereas additional SILAR cycles yielded rough, continuous overlayers of CdSe, apparently consisting of discrete QDs and, for the highest coverages of CdSe, some extended agglomerates. SILAR enabled customization of the thickness of the QD layer. The interface between CdSe QDs and β-$Pb_xV_2O_5$ nanowires was directly imaged by electron microscopy. HAXPES spectra acquired for CdSe/β-$Pb_xV_2O_5$ samples indicate good overlap between the valence band of the CdSe and the mid-gap state of the β-$Pb_xV_2O_5$. Steady-state and time-resolved emission measurements provide compelling evidence for excited-state interfacial hole transfer from CdSe QDs to β-$Pb_xV_2O_5$ nanowires. Future work includes photoelectrochemical experiments to quantify interfacial charge-transfer, transient absorption spectroscopy measurements of the heterostructures, as well as exploration of hot-injection and colloidal methods for direct

growth of QDs onto the nanowire surfaces.[134,135] Our data reveal that these heterostructures may be attractive candidates for applications in light harvesting and interfacial charge transfer for solar energy conversion.

CHAPTER V

DIRECTIONAL CHARGE TRANSFER MEDIATED BY MID-GAP STATES: A TRANSIENT ABSORPTION SPECTROSCOPY STUDY OF CDSE QUANTUM DOT/β-$PB_{0.33}V_2O_5$ HETEROSTRUCTURES*

V.1 Introduction

Harvesting sunlight and storing the energy of the absorbed photons in chemical bonds (in the form of solar fuels) or by doing electrical work (as in photovoltaic devices) is critical to reducing our reliance on fossil fuels.[35–37,132,176] For effective solar energy conversion, not only must a semiconductor absorb a large portion of the incident solar radiation but also the photoexcited electron-hole pairs must be further separated and transported across interfaces.[68,132,176,177] The kinetics of charge separation and transport are a critical consideration to mitigate the recombination or cooling of photogenerated charges.[63,178,179] Achieving efficient charge transfer and separation across semiconductor interfaces is thus predicated on careful alignment of thermodynamic driving forces (which in turn depends on relative band alignments) and on the competing kinetics of directional charge transfer, cooling, and recombination pathways. The appropriate alignment

---

* Reprinted with permission from "Directional Charge Transfer Mediated by Mid-Gap States: A Transient Absorption Spectroscopy Study of CdSe Quantum Dot/β-$Pb_{0.33}V_2O_5$ Heterostructures" by C. C. Milleville, K. E. Pelcher, M. Y. Sfeir, S. Banerjee and D. F. Watson, *J. Phys. Chem. C*, 2016, **120**, 5221–5232. Copyright 2016 American Chemical Society.

of bands is a first and necessary criterion for achieving charge transfer.[132,177,180] In many cases, a visible-light absorbing semiconductor is paired with a wide-bandgap semiconductor, and charge carriers are injected into the latter upon photoexcitation of the former.[35,36,39,132,181] Simple binary semiconductors that have traditionally been studied for photovoltaics have clearly defined valence and conduction band (CB) edges separated by a bandgap and are difficult to reconfigure thereby establishing some immutable limitations on tunability of the thermodynamic driving force. A promising alternative is to strategically position electronic states in a semiconductor through the introduction of dopants or defect states.[46,48] Mid-gap states are often defined by defects or surface traps.[49,63,182,183] In contrast, we have recently designed $M_xV_2O_5$ bronzes wherein the mid-gap states derive from stereoactive lone-pairs of post-transition-metal cations and are thus homogeneously distributed across the crystal.[3] Here we demonstrate that an intercalation-induced mid-gap state in β-$Pb_{0.33}V_2O_5$ can mediate directional charge transfer of both electrons and holes from photoexcited CdSe quantum dots (QDs) to the CB and mid-gap-states of β-$Pb_{0.33}V_2O_5$, respectively. The charge-transfer dynamics are contrasted with those of CdSe QDs interfaced with V_2O_5.

Several promising alternatives to traditional schemes of photoexcitation and charge separation within a semiconductor have been explored to increase the amount of solar energy absorbed and the efficiency with which it is converted to other energy forms.[176] Tandem solar cells, multijunction cells, multiple exciton generation, intermediate band solar cells, and hot-carrier solar cells are examples

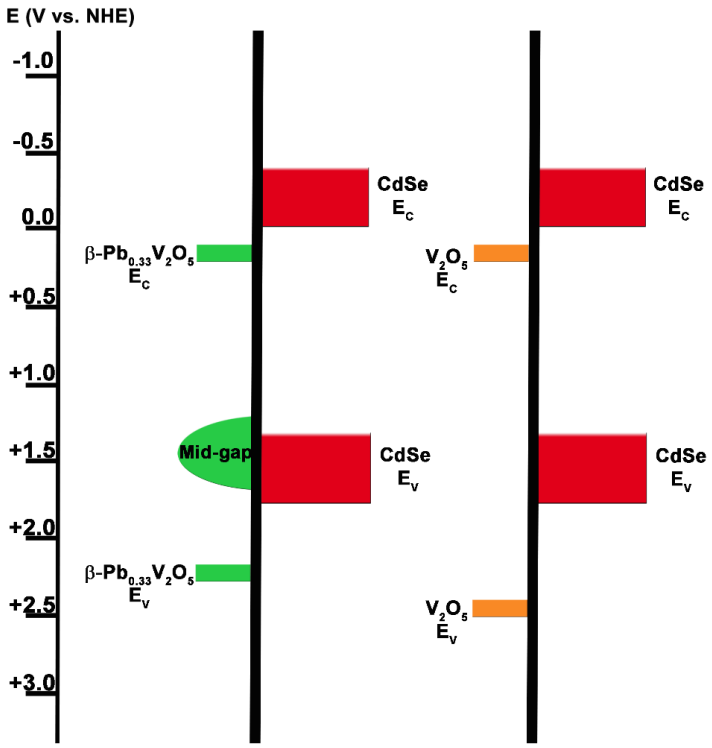

Figure V. 1 Energy diagram depicting approximate relative energy positioning of valence and conduction band edges of CdSe, β-$Pb_{0.33}V_2O_5$, and V_2O_5, as determined from X-ray photoemission spectroscopy. The mid-gap state of β-$Pb_{0.33}V_2O_5$ overlaps with the valence band edge of CdSe.

of different methods that demonstrate promise.[36,37,68,132,176,184–187] Metal oxides have a long history of being used for a variety of applications because of their semiconducting nature; however, the very positive valence band (VB) edge potentials of a majority of metal oxide semiconductors limit their practical use in applications for harvesting solar energy. In previous work, we have found that ternary vanadium oxide bronzes (with the formula of β-$M_xV_2O_5$, where M is a post-transition-metal with a stereoactive lone pair and *x* is its stoichiometry) were

found to possess mid-gap states slightly positive of the oxidation potential of water.[48] This mid-gap state is not present in V_2O_5, the parent oxide of the vanadium oxide bronze.[188] Initial density functional theory calculations predicting the presence of a mid-gap state have recently been experimentally verified using high-energy X-ray photoemission spectroscopy.[46,48,49] The energy positioning of the mid-gap state can be varied by choice of the intercalating cation, thereby providing a facile means for tuning the alignment of these levels with respect to other materials.[3,49] The approximate relative energy positioning of this mid-gap state, along with the VB edge potential (E_V) and CB edge potential (E_C) of both β-$Pb_{0.33}V_2O_5$ and V_2O_5 as well as CdSe is shown in Figure V. 1. This scheme suggests that upon photoexcitation of the CdSe QD (resulting in the creation of a hole in the VB), hole transfer from the VB of the CdSe QD to the mid-gap state of β-$Pb_{0.33}V_2O_5$ is thermodynamically favorable, providing a driving force to extract the hole and ultimately to propagate it along the nanowire for solar fuel production. Indeed, in previous work, we have demonstrated the successful synthesis of CdSe/β-$Pb_{0.33}V_2O_5$ heterostructures and experimentally verified substantial overlap of the CdSe VB edges with the mid-gap states of β-$Pb_{0.33}V_2O_5$ using high-energy X-ray photoemission spectroscopy.[46] Such a heterostructure represents a readily reconfigurable platform wherein the VB edges of the QD can be modulated by compositional variation and size, whereas the energy positioning of the mid-gap state can be tuned by choice of the intercalating cation, thereby

providing access to several routes for tuning the thermodynamic driving forces for charge transfer.

However, thermodynamic alignment of energy levels is but one part of the equation. As previously, directional charge transfer needs to compete with back-electron transfer, charge recombination, and cooling pathways. Several studies have shown that the nature of the interface strongly affects the kinetics of charge transfer.[138–141,143,189] Here we report on the use of transient absorption spectroscopy to explore the kinetics of charge transfer in CdSe/β-$Pb_{0.33}V_2O_5$ heterostructures as a function of the nature of the interface. Charge-transfer dynamics are contrasted for heterostructures prepared *via* two distinct routes: linker-assisted assembly (LAA) and successive ionic layer adsorption and reaction (SILAR). LAA allows for more precise control over QD size and the separation between the two components, whereas SILAR facilitates direct contact between the QDs and the nanowires but does not allow for precise size control. The charge-transfer kinetics for CdSe/*β*-$Pb_{0.33}V_2O_5$ heterostructures are contrasted with those of CdSe/V_2O_5 heterostructures to elucidate the role of the mid-gap states in facilitating charge transfer.

V.2 Experimental

V.2.1 Synthesis of β-$Pb_{0.33}V_2O_5$ and V_2O_5 Nanowires

β-$Pb_{0.33}V_2O_5$ nanowires were prepared using a one-step hydrothermal reaction as previously reported.[48] In brief, stoichiometric amounts of $Pb(CH_3COO)_2 \cdot 3H_2O$ and

V_2O_5 were placed in a polytetrafluoroethylene-lined acid digestion vessel (Parr) along with 16 mL of deionized (DI) water. The vessel was sealed in an autoclave and heated to 250ºC for 72 h. The product was isolated by vacuum filtration, washed with copious amounts of water, and allowed to dry in air. The resulting nanowires were ca. 170 nm in diameter and spanned microns in length.[48] The lead cations are highly ordered along the 1D tunnels of β-$Pb_{0.33}V_2O_5$, as evidenced by the appearance of superlattice reflections.[48] Such precise cation ordering is expected to provide a means for homogeneously modulating of the electronic structure of the entire nanowire unlike dopant sites, wherein the introduced states are rather localized. V_2O_5 nanowires were prepared by the oxidation of hydrothermally grown $V_3O_7{\cdot}xH_2O$ nanowires as reported in previous work.[144] The V_2O_5 nanowires were ca. 150-250 nm in diameter and spanned hundreds of microns in length.[144]

V.2.2 Synthesis of CdSe QDs

Cysteine-capped CdSe (Cys-CdSe) QDs were synthesized as previously reported.[147] In brief, the selenium precursor was prepared by refluxing an aqueous solution of Se powder and Na_2SO_3 overnight, and the cadmium precursor was an aqueous solution of $3CdSO_4{\cdot}8H_2O$ and cysteine. The pH of the cadmium precursor was titrated to 12.5 to 13.0 with solid NaOH. The hot selenium precursor was added to the cadmium precursor and allowed to stir for 30 min. The resulting dispersions of Cys-CdSe QDs, hereafter referred to as Cys-CdSe(sm) QDs, were purified by solvent-nonsolvent (H_2O/MeOH, 3:1) washing to remove excess reagents. Larger Cys-CdSe (Cys-CdSe(lg)) QDs were synthesized and purified by the same procedure, except that

the cadmium precursor was heated to, and maintained at, 80°C for the duration of the reaction (2 h).

V.2.3 Functionalization of β-$Pb_{0.33}V_2O_5$ and V_2O_5 Nanowires with CdSe QDs by SILAR and LAA

CdSe was deposited onto β-$Pb_{0.33}V_2O_5$ nanowires *via* SILAR and LAA following our reported methods.[46] In a single SILAR cycle, CdSe QDs were grown directly onto β-$Pb_{0.33}V_2O_5$ nanowires by sequentially mixing the nanowires with a 50 mM solution of $Cd(NO_3)_2$ in ethanol, followed by a 50 mM solution of Na_2Se in ethanol. The nanowires were washed with ethanol following each mixing step to remove excess ions. This SILAR process was performed once (1× SILAR samples), three times (3× SILAR samples), or five times (5× SILAR samples) to vary the density of CdSe QDs on the surface of the nanowires. An analogous procedure was utilized to coat V_2O_5 nanowires with CdSe.

LAA was employed to prepare Cys-CdSe(sm)/β-$Pb_{0.33}V_2O_5$ and Cys-CdSe(lg)/β-$Pb_{0.33}V_2O_5$ heterostructures (and corresponding V_2O_5 heterostructures) in which cysteine acted as a bifunctional linker molecule. As reported in our previous work, cysteine bound preferentially to CdSe *via* the thiolate functional group and to β-$Pb_{0.33}V_2O_5$ through an electrostatic interaction between a positively charged, protonated amine group on cysteine and the negatively charged, hydroxylated surface of β-$Pb_{0.33}V_2O_5$ (or V_2O_5).[46] In LAA, an aqueous dispersion of β-$Pb_{0.33}V_2O_5$ (or V_2O_5) nanowires was added to an aqueous dispersion of purified Cys-CdSe(sm) or Cys-CdSe(lg) QDs and allowed to

equilibrate overnight (12-16 h). CdSe-functionalized nanowires were recovered by centrifugation, rinsed with DI water to remove excess QDs, and subsequently dried at room temperature before characterization.

V.2.4 Preparation of Thin Films and Diffuse Reflectance Measurements

The nanowires and QD/nanowire heterostructures were immobilized onto glass microscope slides for diffuse reflectance and transient absorption measurements. Dispersions (20 mL) of β-$Pb_{0.33}V_2O_5$, V_2O_5, CdSe/β-$Pb_{0.33}V_2O_5$, or CdSe/V_2O_5 in ethanol (1 mg/mL) were spray coated onto the substrate, forming semitransparent thin films. UV-vis diffuse reflectance spectra of sample films were obtained with an Agilent 8453 diode array spectrophotometer equipped with a Labsphere RSA-HP-53 (Hewlett-Packard) reflectance accessory.

V.2.5 Spectroelectrochemistry Experiments

Spectroelectrochemical measurements were performed on β-$Pb_{0.33}V_2O_5$ and V_2O_5 films to monitor changes in the absorption spectra upon oxidation or reduction. Films were prepared by spray coating nanowires onto fluorine-doped tin oxide (FTO)-coated glass slides. A one-compartment, three-electrode electrochemical cell configuration was used consisting of a thin film working electrode, a Pt mesh auxiliary electrode, and a saturated calomel (SCE) reference electrode. Electrochemical measurements were performed using a Princeton Applied Research (PAR) VersaSTAT 3 potentiostat. A quartz cuvette (1 cm path length) with a 24/40 ground glass joint connection was used as the cell, and the electrolyte consisted of 0.1 M tetrabutylammonium perchlorate (Alfa Aesar, electrochemical grade) in anhydrous acetonitrile (EMD). The electrolyte solution

was prepared in a glovebox and then brought out immediately before beginning the experiments to avoid contamination with water. The cell was further purged with nitrogen to remove dissolved oxygen. The entire cell assembly was housed on the sample stage of spectrophotometer so that absorption spectra could be obtained while performing electrochemical measurements. For β-$Pb_{0.33}V_2O_5$ films, either an oxidizing potential of +1.75 V (vs SCE) or a reducing potential of -1.0 V (vs SCE) was applied. In contrast, for V_2O_5 films, either an oxidizing potential of +1.5 V (vs SCE) or a reducing potential of -0.25 V (vs SCE) was applied. Absorption spectra of the oxidized or reduced films were obtained after applying a potential for 5 min. Separate films were used for the oxidation and reduction reactions in case any redox processes were irreversible. Ground-state differential absorption spectra were computed by subtracting the absorption spectrum of the neutral sample from the absorption spectrum of the oxidized or reduced sample.

V.2.6 Transient Absorption Experiments

Transient absorption experiments were performed at the Advanced Optical Spectroscopy and Microscopy Facility in the Center for Functional Nanomaterials at Brookhaven National Laboratory (BNL). Ultrafast transient absorption measurements were conducted using a commercial Ti:sapphire amplified laser system (SpectraPhysics Spitfire Pro, 1 kHz repetition rate). Excitation light was generated using a commercial optical parametric amplifier (LightConversion). Supercontinuum probe light was generated by focusing the 800 nm fundamental into a sapphire disc. The probe light was split into signal and reference beams, both of which were detected on a shot-by-shot

basis with fiber-coupled silicon (visible) or InGaAs (infrared) diode arrays. The pump-probe delay was controlled by means of a mechanical delay stage (Newport). Nanosecond transient absorption measurements were conducted using the same ultrafast pump pulses along with an electronically delayed supercontinuum light source with a subnanosecond pulse duration (EOS, Ultrafast Systems). Transient absorbance (TA) spectra presented in this manuscript were extracted from the data matrix by averaging ΔA values between 1.5 and 10 ns. TA decay traces presented in this manuscript compiled by averaging ΔA values over a given range of probe wavelengths (λ_{probe}) at each delay time.

V.3 Results and Discussion

V.3.1 Ground-State Absorption Spectra of Unfunctionalized β-$Pb_{0.33}V_2O_5$ and V_2O_5 Nanowires

Diffuse reflectance spectra of V_2O_5 and β-$Pb_{0.33}V_2O_5$ films on glass slides are shown in Figure V. 2A. V_2O_5 displays an absorption onset at 580 nm with a steep rise in absorbance corresponding to bandgap excitation. β-$Pb_{0.33}V_2O_5$ displays an absorption onset at 615 nm with a gradual increase in absorbance to ~540 nm, followed by a steep increase in absorbance, similar to V_2O_5. The red-shifted absorption onset for β-$Pb_{0.33}V_2O_5$ is assigned to the lower energy transition associated with excitation of an electron from the mid-gap state to CB states. A gradual increase in absorbance can be attributed to a convolution of mid-gap excitation and bandgap excitation. A broad absorption feature for the mid-gap excitation is not surprising owing to a broad energy

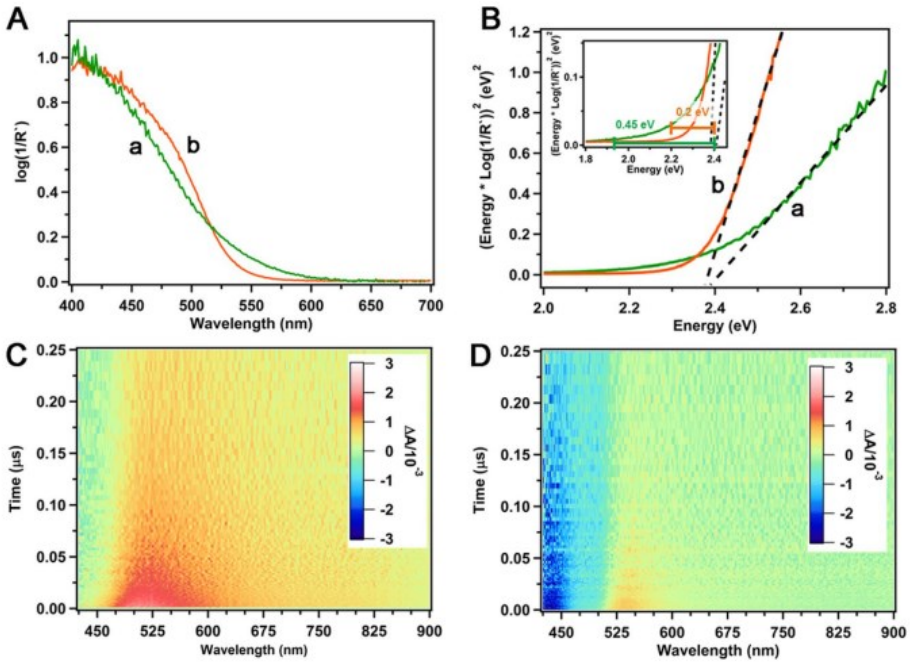

Figure V. 2 Ground-state diffuse reflectance spectra (A) and corresponding Tauc plots (B) of (a) β-$Pb_{0.33}V_2O_5$ (green) and (b) V_2O_5 (orange). The insert shows a closer view of the non-linear region. "Color maps" showing ΔA at all delay times and probe wavelengths for β-$Pb_{0.33}V_2O_5$ (C) and V_2O_5 (D) with λ_{pump} = 360 nm.

range of the mid-gap states as opposed to a single discrete energy level. On the basis of previous high-energy X-ray photoemission studies and density functional theory calculations, the mid-gap state represents a filled antibonding state derived from the hybridization of Pb 6s and O 2p bands.[49]

Tauc plots are commonly employed to determine the optical bandgap of semiconductors by extrapolating the linear region to the abscissa.[190,191] Tauc plots of (energy × log(1/*R*))^2 versus energy, where *R* is reflectance, for V_2O_5 and β-$Pb_{0.33}V_2O_5$ (inset to Figure V. 2B) accentuate the mid-gap excitation features. Both plots contain a linear region, associated with bandgap excitation, and a

pronounced deviation from linearity at lower energies due to intrinsic localized absorptions derived from mid-gap states. An optical bandgap of ca. 2.4 eV was determined for both V_2O_5 and β-$Pb_{0.33}V_2O_5$. Closer examination of the nonlinear region provides clear evidence of transitions involving the excitation of electrons from surface-localized or intercalative mid-gap states to the CB (in-set to Figure V. 2B). The energy difference between the absorption onset and bandgap excitation can be interpreted as the difference between the highest-energy localized mid-gap states and the VB edge. Measured differences of 0.12 and 0.37 eV were obtained for V_2O_5 and β-$Pb_{0.33}V_2O_5$, respectively. Assuming no significant change in the distribution of localized surface states for β-$Pb_{0.33}V_2O_5$ relative to V_2O_5, the larger shift of the absorption onset relative to the bandgap excitation for β-$Pb_{0.33}V_2O_5$ can be attributed to the presence of intercalative mid-gap states at even higher energies than surface-localized states above the VB edge.

V.3.2 Transient Absorption Spectra of Unfunctionalized β-$Pb_{0.33}V_2O_5$ and V_2O_5 Nanowires

Transient absorption spectra were acquired to examine excited-state spectral features and dynamics of β-$Pb_{0.33}V_2O_5$ and V_2O_5 nanowires. Data were acquired with pulsed excitation at 360, 425, 490, and 600 nm; selected data are presented in subsequent sections. Films of β-$Pb_{0.33}V_2O_5$ and V_2O_5 were excited at 360 nm and probed from 425 to 900 nm. The excitation wavelength corresponds to an energy greater than the bandgap of both materials. Three-dimensional TA "color maps" of β-$Pb_{0.33}V_2O_5$ and V_2O_5 (Figure V. 2C, D) reveal clear differences

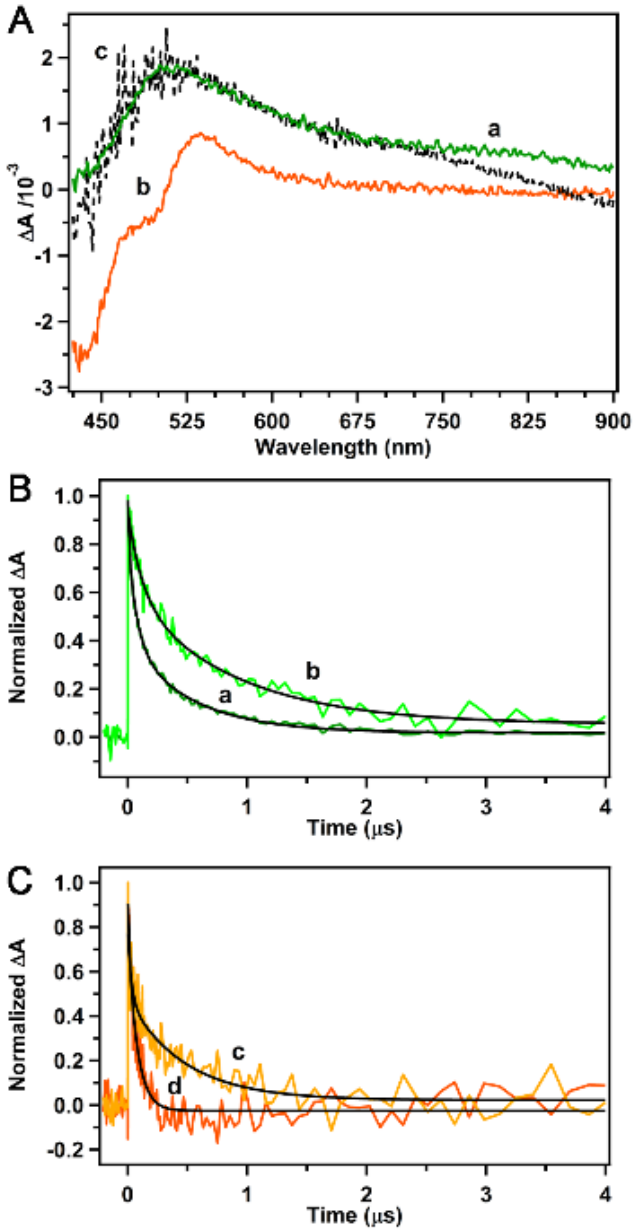

Figure V. 3 (A) TA spectrum of β-$Pb_{0.33}V_2O_5$ (a, green), TA spectrum of V_2O_5 (b, orange), and fit of spectrum (a) to a linear combination of oxidized and reduced β-$Pb_{0.33}V_2O_5$ (c, black) as derived from spectroelectrochemical measurements. (B, C) TA decay traces and fits for β-$Pb_{0.33}V_2O_5$ at λ_{probe} = 510 (a) and 750 nm (b) and for V_2O_5 at λ_{probe} = 430 (c) and 535 nm (d). For all data, λ_{pump} = 360 nm.

between the two samples, owing to the presence of mid-gap states in β-

$Pb_{0.33}V_2O_5$. TA spectra (ΔA vs wavelength) were extracted from the data matrix by averaging ΔA values between 1.5 and 10 ns at all probe wavelengths. The TA spectrum of β-$Pb_{0.33}V_2O_5$ (Figure V. 3A) is characterized by two absorption bands: a more intense band centered at ca. 510 nm and a less intense and broad shoulder stretching from ca. 650 nm into the near IR, with a center at ca. 750 nm. The TA spectrum of V_2O_5 differs markedly and is instead characterized by a bleach centered at ca. 430 nm and an absorption band centered at ca. 535 nm (Figure V. 3A).

Spectroelectrochemical measurements were acquired to assist with the assignment of TA spectra. Ground-state absorption spectra of V_2O_5 and β-$Pb_{0.33}V_2O_5$ films on FTO electrodes were acquired under the application of either an oxidizing or reducing potential. Absorbance difference spectra were generated by subtracting the absorbance spectrum of the neutral species from that of the oxidized or reduced species (Figure A. 14). Oxidation of both V_2O_5 and β-$Pb_{0.33}V_2O_5$ yielded a broad induced absorption band extending from <375 to ca. 675 nm. The oxidation of β-$Pb_{0.33}V_2O_5$ corresponds to the removal of electrons from filled mid-gap states that lie above the VB;[48,49] thus we assign the induced absorption to the excitation of VB electrons into empty mid-gap states. For V_2O_5, which has no intercalative mid-gap states, oxidation corresponds primarily to the removal of electrons from VB states. Therefore, the induced absorbance arises from the excitation of deep-VB electrons to the VB edge. Notably, the VB of β-$Pb_{0.33}V_2O_5$ is characterized by a pronounced Pb 6s-O2p bonding state that does

not exist for V_2O_5.[18] Reduction of both V_2O_5 and β-$Pb_{0.33}V_2O_5$ yielded a bleach of the bandgap absorption (Figure A. 14), consistent with the Burstein-Moss effect.[192–194] Reduction involves the filling of CB states, effectively increasing the optical bandgap and blue-shifting the bandgap absorption onset. Reduced β-$Pb_{0.33}V_2O_5$ also exhibited an induced absorption band extending from ca. 620 nm into the near IR. We assign this absorption to the excitation of electrons in the CB of reduced β-$Pb_{0.33}V_2O_5$ to higher-energy states, consistent with established spectral assignments for reduced metal oxides.[193–196]

The spectroelectrochemical data were used to assign features in the TA spectra of β-$Pb_{0.33}V_2O_5$ and V_2O_5. We assign the 510 nm absorption band in the TA spectrum of β-$Pb_{0.33}V_2O_5$, which exhibits similar absorption maximum and spectral profile as the induced absorption band of oxidized β-$Pb_{0.33}V_2O_5$, to the excitation of an electron from the VB to empty mid-gap states. We assign the broad 750 nm absorption band, which is similar to the induced absorption band of reduced β-$Pb_{0.33}V_2O_5$, to the excitation of free CB electrons. Importantly, the TA spectrum of photoexcited β-$Pb_{0.33}V_2O_5$ is well-modeled as a linear combination of the absorbance difference spectra associated with electrochemically reduced and oxidized β-$Pb_{0.33}V_2O_5$ (Figure V. 3A), supporting our interpretation of transient absorption bands as arising from the introduction of electrons into the CB and holes into the mid-gap states. For V_2O_5, the transient bleach at 430 nm is assigned to a bleach of the ground-state absorbance, as exhibited by reduced V_2O_5. The transient absorption band at 535 nm, which is similar to the induced absorption

band of oxidized V_2O_5, is assigned to the excitation of electrons from deep within the VB to the VB edge.

V.3.3 Excited-State Relaxation Dynamics of Unfunctionalized β-$Pb_{0.33}V_2O_5$ and V_2O_5 Nanowires

TA decay traces on time scales of 10^{-9}-10^{-5} s for β-$Pb_{0.33}V_2O_5$ and V_2O_5 were extracted from transient absorption data matrices by averaging ΔA values at a range of probe wavelengths for each delay time. Representative decay traces are shown in Figure V. 3B and C. TA decay traces were fit to multiexponential decay kinetics. The smallest number of individual decay lifetimes, τ_i, which resulted in the minimum χ^2 was used for each fit. All TA decay traces were modeled to biexponential decay kinetics (Equation V.1 with $i = 2$) except for the decay of the 510 nm absorption band of β-$Pb_{0.33}V_2O_5$, for which triexponential decay kinetics (Equation V.1 with $i = 3$) yielded a substantially improved fit (on the basis of χ^2). Fitting parameters for all TA decay traces are listed in Tables A. 3-A. 5. V_2O_5 has previously exhibited multiexponential transient absorption decay kinetics due to the presence of distributions of electron and hole trap states that give rise to multiple trap-state recombination mechanisms.[197]

$$\Delta A = \Delta A_0 + \Sigma_i A_i e^{(-t/\tau_i)} \quad (V.1)$$

$$\langle\tau\rangle = (\Sigma_i A_i \tau_i)/(\Sigma_i A_i) \quad (V.2)$$

TA decay traces reveal differences in kinetics for the various processes occurring in both samples. The decay traces (Figure V. 3B,C) and the "color

maps" (Figure V. 2C,D) reveal clearly that excited states are longer-lived in β-$Pb_{0.33}V_2O_5$ than in V_2O_5. Long-lived excited states are desirable because charge transfer can compete more effectively with electron-hole recombination. For ease of comparison and discussion of decay kinetics, amplitude-weighted average lifetimes (<τ>) were computed using equation V.2. For β-$Pb_{0.33}V_2O_5$, the 510 and 750 nm transient absorption bands had <τ> of $(2.3 \pm 0.1) \times 10^{-7}$ and $(5.9 \pm 0.7) \times 10^{-7}$ s, respectively. For V_2O_5, the 430 nm bleach and 535 nm TA band had <τ>of $(2.9 \pm 0.5) \times 10^{-7}$ and $(7 \pm 2) \times 10^{-8}$ s, respectively. A first observation is that the transient absorption band of β-$Pb_{0.33}V_2O_5$ centered at 750 nm, assigned to excitation of free CB electrons, is longer-lived than the bleach observed for V_2O_5, suggesting that the introduction of the mid-gap states (and the corresponding filled Pb 6s-O2p states in the VB) increases the lifetime of the excited electron. A second key observation is that the features associated with the hole (510 nm absorption band in β-$Pb_{0.33}V_2O_5$ and 535 nm absorption band in V_2O_5) decay more rapidly than the features associated with the electron (750 nm absorption band in β-$Pb_{0.33}V_2O_5$ and 430 nm bleach in V_2O_5). Finally, the hole is much longer lived in β-$Pb_{0.33}V_2O_5$ than in V_2O_5. This pronounced difference may arise from different spatial distributions of holes in the two compounds. The photogenerated holes in β-$Pb_{0.33}V_2O_5$ reside in mid-gap states, which derive primarily from a Pb 6s-O 2p interaction and thus are localized on the intercalating Pb^{2+}-ions;[48] in contrast, the photogenerated hole in V_2O_5 is situated within the O 2p-derived VB on the V_2O_5 framework.[198,199] For both structures, the electrons

reside on V 3d states in the CB (the $3d_{xy}$ states are the lowest lying CB states).[198,199] In other words, the electron-hole wave function overlap is expected to be greater for V_2O_5 where both charge carriers are localized on the V_2O_5 framework, whereas in β-$Pb_{0.33}V_2O_5$, the holes are located on the intercalants and the electrons reside on the V_2O_5 framework. This spatial separation is likely responsible for the longer excited-state lifetimes observed for the latter.

V.3.4 Transient Absorption Spectra of CdSe/β-$Pb_{0.33}V_2O_5$ and CdSe/V_2O_5 Heterostructures

CdSe/β-$Pb_{0.33}V_2O_5$ heterostructures, synthesized using both LAA and SILAR methods, were characterized with transient absorption spectroscopy (Figure V. 4). Thin films of CdSe/β-$Pb_{0.33}V_2O_5$ heterostructures were excited at 360 and 425 nm and probed from 425 to 900 nm. These pump wavelengths correspond to above-bandgap excitation for β-$Pb_{0.33}V_2O_5$ and V_2O_5 and to excitation substantially above the bandgap for CdSe QDs; 425 nm excitation is resonant with the first-excitonic absorption of CdSe QDs (Figure A. 15). TA spectra were compiled by averaging ΔA from 1.5 to 10 ns. Figures V. 4A and B show the results for the heterostructures excited at 360 nm pump wavelength. Interestingly, TA spectra of CdSe/β-$Pb_{0.33}V_2O_5$ heterostructures are nearly identical to those of β-$Pb_{0.33}V_2O_5$ nanowires and consist of an intense transient absorption band centered at 500-550 nm and a less intense and lower energy absorption band extending into the near-IR. These spectra are notable for the absence of a bleach of the first excitonic transition of CdSe QDs, which is the well-established spectral signature of CdSe QDs on time scales greater than 10^{-9} s,[200–202] and was the dominant

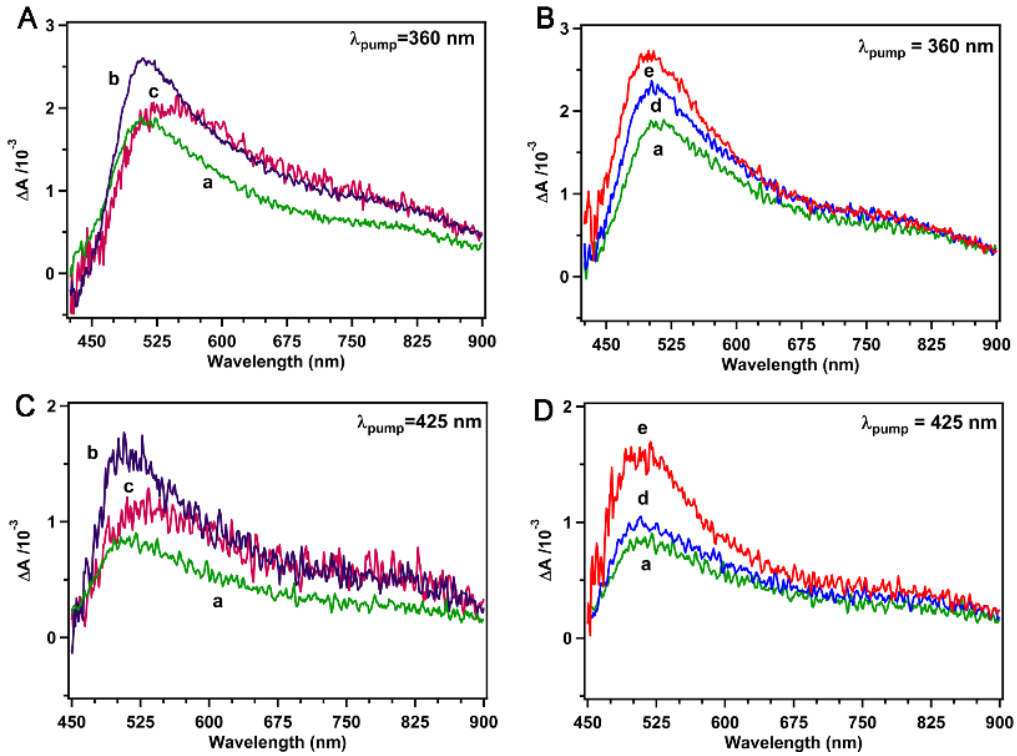

Figure V. 4 TA spectra of (a) β-$Pb_{0.33}V_2O_5$, (b) 1× SILAR CdSe/β-$Pb_{0.33}V_2O_5$, (c) 3× SILAR CdSe/β-$Pb_{0.33}V_2O_5$, (d) Cys-CdSe(sm)/β-$Pb_{0.33}V_2O_5$, and (e) Cys-CdSe(lg)/β-$Pb_{0.33}V_2O_5$ with λ_{pump} = 360 and 425 nm. ΔA values are averages of measured data at delay times of 1.5 to 10 ns.

feature of our measured TA spectrum of dispersed aqueous Cys-CdSe(lg) QDs (Figure A. 16). Thus, excitation of either CdSe QDs or β-$Pb_{0.33}V_2O_5$ nanowires within the heterostructures yielded a TA spectrum associated with electron-hole pairs localized in the β-$Pb_{0.33}V_2O_5$ nanowires. The most notable difference in the TA spectra of CdSe/β-$Pb_{0.33}V_2O_5$ heterostructures relative to the bare β-$Pb_{0.33}V_2O_5$ nanowires is that the spectra of heterostructures exhibit a substantial amplification of the absorption bands. This enhanced amplitude (increased ΔA) suggests an increase in the concentration of excited states in the β-$Pb_{0.33}V_2O_5$ nanowires arising from the injection of both holes and

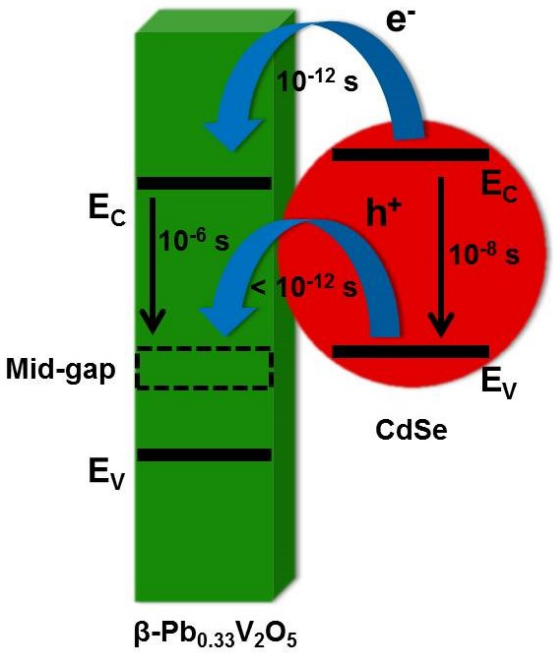

Figure V. 5 Time scales of excited-state interfacial charge transfer and electron-hole recombination processes of CdSe/β-$Pb_{0.33}V_2O_5$ heterostructures.

electrons from the CdSe QDs. In other words, apart from the native excited-state population generated by direct excitation of β-$Pb_{0.33}V_2O_5$, the transfer of electrons and holes from photoexcited CdSe QDs, both of which are thermodynamically favorable (Figure V. 1), further increases the population of excited states within the underlying nanowires. This behavior is agnostic of the nature of the interfaces and is observed for both the LAA and SILAR heterostructures. The excited-state charge-transfer processes of CdSe/β-$Pb_{0.33}V_2O_5$ heterostructures are summarized in Figure V. 5, which includes times scales of electron and hole transfer derived from ultrafast TA measurements described later.

The higher energy and more intense absorption band in the TA spectrum of 3× SILAR CdSe/β-$Pb_{0.33}V_2O_5$ heterostructures (spectrum c in Figure V. 4) is red-shifted relative to those of 1× SILAR CdSe/β-$Pb_{0.33}V_2O_5$ heterostructures (spectrum b in Figure V. 4) and β-$Pb_{0.33}V_2O_5$ nanowires (spectrum a in Figure V. 4). This apparent red shift may have arisen from the increased contribution of the ground-state bleach of CdSe, because the 3× SILAR sample has a significantly higher ratio of CdSe QDs to β-$Pb_{0.33}V_2O_5$ nanowires. If an appreciable fraction of QDs was not in direct contact with the nanowire surface, as previously observed,[46] then such QDs would probably not transfer charge carriers efficiently to the nanowires, resulting in some contribution of the excitonic bleach of CdSe to the overall TA spectrum and the corresponding diminution of the measured absorbance difference on the high energy side of the absorption band.

TA spectra of CdSe/β-$Pb_{0.33}V_2O_5$ heterostructures and bare β-$Pb_{0.33}V_2O_5$ nanowires acquired with 425 nm excitation were also nearly identical but with higher ΔA values for the QD-coated samples. The amplified absorption bands associated with the nanowire-localized excited states can again be attributed to the transfer of both electrons and holes from CdSe QDs to β-$Pb_{0.33}V_2O_5$ nanowires.

TA spectra of CdSe/V_2O_5 heterostructures were collected as a set of control experiments. The transfer of holes from CdSe to V_2O_5 is thermodynamically disfavored, whereas the injection of electrons from photoexcited CdSe to V_2O_5 is feasible based on the relative energy positioning of the CB edges of CdSe and V_2O_5 (Figure V. 1). Films of V_2O_5 and CdSe/V_2O_5 heterostructures were excited

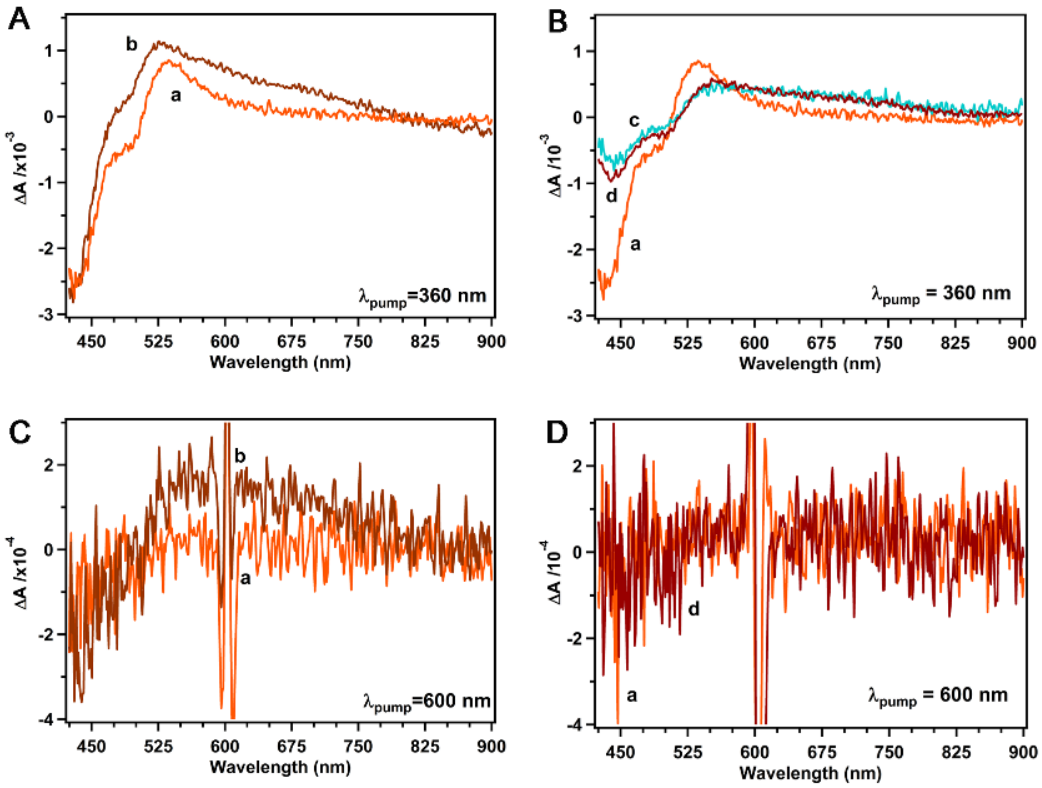

Figure V. 6 TA spectra of (a) V_2O_5, (b) 5× SILAR CdSe/V_2O_5, (c) Cys-CdSe(sm)/V_2O_5, and (d) Cys-CdSe(lg)/V_2O_5 with λ_{pump} = 360 and 600 nm. ΔA values are averages of measured data at delay times of 1.5 to 10 ns.

at 360 and 600 nm and probed between 425 and 900 nm, and TA spectra were compiled by averaging ΔA from 1.5 to 10 ns. The 5× SILAR CdSe/V_2O_5 heterostructures were chosen because the coverage of QDs on V_2O_5 nanowires was similar to the coverage of QDs on β-$Pb_{0.33}V_2O_5$ nanowires in 1× SILAR CdSe/β-$Pb_{0.33}V_2O_5$ heterostructures, as verified by energy-dispersive X-ray analysis.[46] TA spectra of CdSe/V_2O_5 heterostructures differ significantly from the TA spectrum of V_2O_5 and furthermore exhibit substantial differences depending

on the nature of the interface (Figure V. 6). First, in TA spectra acquired with excitation at 360 nm (Figure V. 6A, B), the CdSe/V_2O_5 heterostructures synthesized by both SILAR and LAA exhibit a transient absorption band centered at 525-545 nm, which is shifted and broadened significantly to long wavelengths relative to the 535 nm absorption band of V_2O_5. The band is less intense for CdSe/V_2O_5 heterostructures prepared by LAA than for those prepared by SILAR. Second, the transient absorption band of CdSe/V_2O_5 heterostructures is much more intense than that of V_2O_5 nanowires beyond 575 nm and extends into the near-IR. TA spectra of V_2O_5 nanowires and of Cys-CdSe(lg)/V_2O_5 heterostructures prepared by LAA were featureless when acquired with excitation at 600 nm (Figure V. 6C, D) because 600 nm light is insufficiently energetic to excite the bandgap transition of V_2O_5 nanowires or Cys-CdSe(lg) QDs (Figure A. 15). In contrast, the TA spectrum of 5× SILAR CdSe/V_2O_5 heterostructures, acquired with excitation at 600 nm, exhibits a poorly resolved bleach at wavelengths <500 nm, consistent with the filling of CB states of V_2O_5 and the Burstein-Moss effect. Additionally, the TA spectrum exhibits a long-wavelength absorption band similar to that observed upon excitation at 360 nm. This long-wavelength absorption band is noteworthy and facilitates spectral assignments. We attribute this feature, which extends to ca. 750 nm, to an absorption associated with trapped holes in CdSe QDs, consistent with reported assignments of TA spectra of oxidized CdSe QDs.[203] The transient absorption associated with a trapped hole, together with the transient bleach correlated with electrons in the CB

of V_2O_5, suggests that photoexcitation of the QDs is followed by electron transfer to V_2O_5, which is thermodynamically favorable (Figure V. 1). Transfer of the photogenerated hole from CdSe to the VB of V_2O_5 is thermodynamically uphill (Figure V. 1) and thus the hole apparently remains in the QD where it is confined in surface-localized trap states. The long-wavelength absorption band in the TA spectra of CdSe/V_2O_5 heterostructures acquired with 360 nm excitation (Figure V. 6A, B) can thus also be similarly assigned. The shift of the TA band centered at 535 nm for V_2O_5 can now be assigned to an increased proportion of reduced V_2O_5 in the heterostructures as a result of electron transfer from the photoexcited QDs (Figure A. 14). In addition, the superposition of a bleach from photoexcited QDs at probe wavelengths of 475-540 nm (Figure A. 16) probably also contributed to the observed shift of the maximum of the net transient absorption centered at 525-545 nm. Because the 600 nm pump pulse was insufficiently energetic to excite Cys-CdSe(lg) QDs, it is not surprising that TA spectrum (c) in Figure V. 6D suggests no evidence of charge transfer. In contrast, the CdSe/V_2O_5 heterostructures prepared by SILAR have a broader size distribution including larger nanocrystal sizes that exhibit measurable ground-state absorption beyond 600 nm (Figure A. 15C); therefore, the 600 nm excitation pulse excitated a fraction of the QDs, enabling electron transfer to V_2O_5 and giving rise to the broad long-wavelength absorption associated with the hole in CdSe observed in Figure V. 6C. TA spectra acquired for these samples at pump wavelengths of 425 and 490 nm, both of which are more energetic than the bandgap of CdSe QDs, are

shown in Figure A. 17. The TA spectra acquired at these pump wavelengths for $CdSe/V_2O_5$ heterostructures prepared by LAA and SILAR are markedly different. TA spectra for the SILAR-derived samples exhibit characteristic spectral signatures of electron transfer, whereas TA spectra of the LAA-derived samples are unmodified from that of V_2O_5 revealing the absence of electron transfer. These findings suggest that following excitation at 360 nm hot electrons can be injected across the interfaces defined by the molecular linker but electrons excited to the CB edge are not energetic enough to diffuse across the interface. In contrast, electron transfer is observed following excitation at all pump wavelengths for the SILAR-derived interface.

V.3.5 Excited-State Relaxation Dynamics of CdSe/β-$Pb_{0.33}V_2O_5$ and CdSe/V_2O_5 Heterostructures

TA decay traces of CdSe/β-$Pb_{0.33}V_2O_5$ samples pumped at 360 nm are shown in Figure V. 7. TA decay traces of the 510 nm absorption band were well-modeled with triexponential kinetics, and decay traces of the 750 nm band were well-modeled with biexponential kinetics. Tables A. 3 and A. 4 list fitting parameters and calculated average lifetimes. Upon functionalization of β-$Pb_{0.33}V_2O_5$ with CdSe QDs *via* both SILAR and LAA deposition methods, values of $\langle\tau\rangle$ for both the 510 and 750 nm transient absorption bands increased relative to uncoated β-$Pb_{0.33}V_2O_5$. For the 510 nm band, $\langle\tau\rangle$ increased by approximately 3-fold for SILAR-deposited CdSe/β-$Pb_{0.33}V_2O_5$. LAA-derived samples exhibited greater increases in $\langle\tau\rangle$ of approximately 3.9 and 6.5 fold for Cys-CdSe(sm)/β-

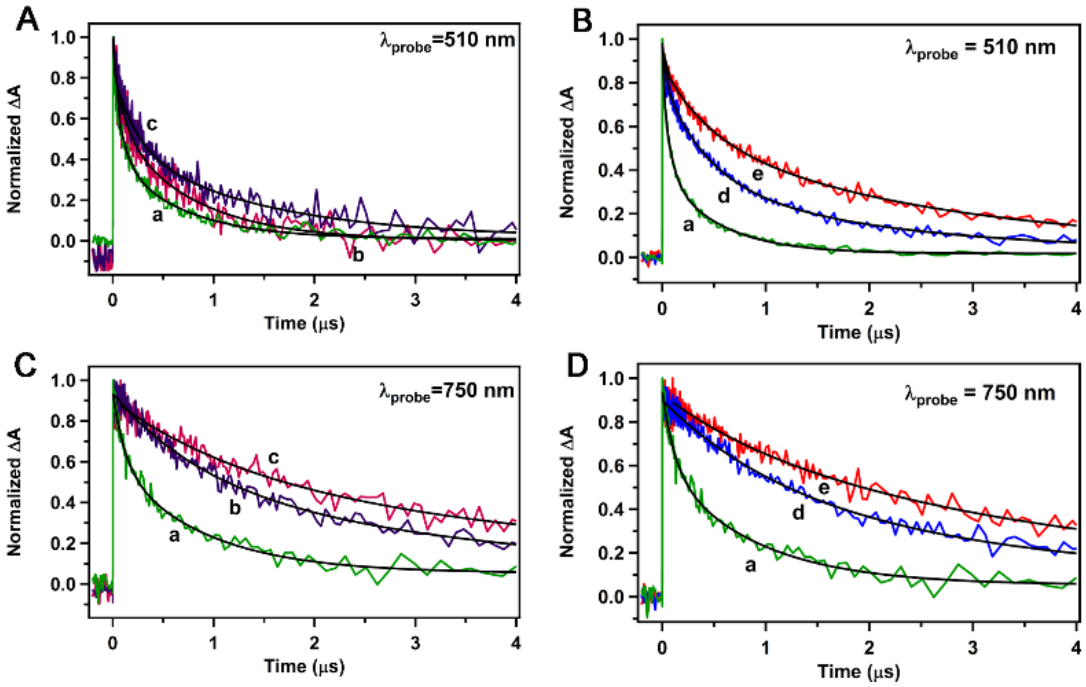

Figure V. 7 TA decay traces and fits for (a) β-$Pb_{0.33}V_2O_5$, (b) 1× SILAR CdSe/β-$Pb_{0.33}V_2O_5$, (c) 3× SILAR CdSe/β-$Pb_{0.33}V_2O_5$, (d) Cys-CdSe(sm)/β-$Pb_{0.33}V_2O_5$, and (e) Cys-CdSe(lg)/β-$Pb_{0.33}V_2O_5$ at probe wavelengths of 510 and 750 nm with λ_{pump} = 360 nm.

$Pb_{0.33}V_2O_5$ and Cys-CdSe(lg)/β-$Pb_{0.33}V_2O_5$ heterostructures, respectively. The value of $<\tau>$ for the 750 nm absorption band increased by approximately 5-fold for CdSe/β-$Pb_{0.33}V_2O_5$ prepared using both deposition methods. Observed increases in excited-state lifetimes for CdSe/β-$Pb_{0.33}V_2O_5$ are attributed to surface passivation of β-$Pb_{0.33}V_2O_5$ nanowires by the CdSe QDs and the elimination of surface trap states and trap-state-mediated electron-hole recombination pathways. The effects of surface passivation apparently outweigh the possible acceleration of electron-hole recombination that might be expected with the increased initial

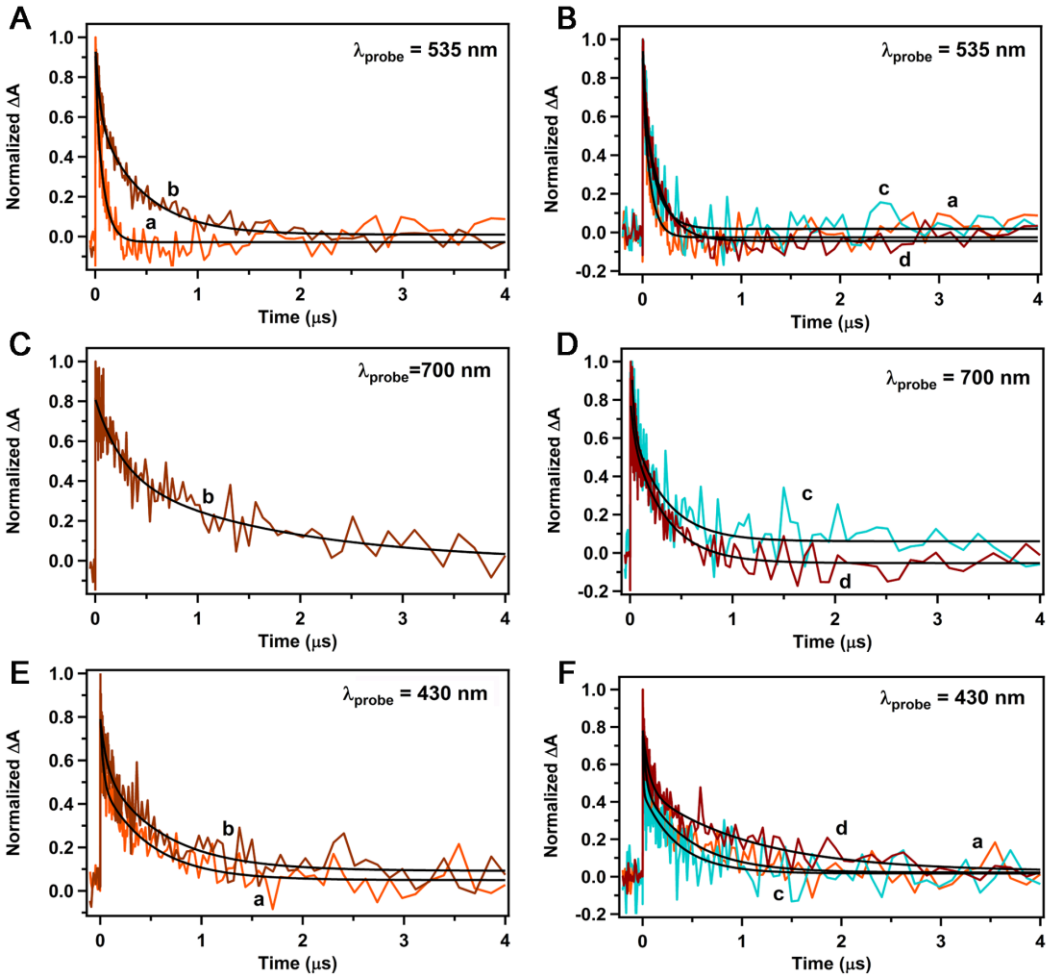

Figure V. 8 TA decay traces and fits for (a)V_2O_5, (b) 5× SILAR CdSe/V_2O_5, (c) Cys-CdSe(sm)/V_2O_5, and (d) Cys-CdSe(lg)/V_2O_5 at probe wavelengths of 535, 700, and 430 nm with λ_{pump} = 360 nm.

population of electrons and holes in β-$Pb_{0.33}V_2O_5$ nanowires interfaced with CdSe QDs.

TA decay traces of CdSe/V_2O_5 samples pumped at 360 nm are shown in Figure V. 8. All decay traces were well-modeled by biexponential kinetics; fitting parameters and average lifetimes are compiled in Table A. 5. Deposition of CdSe

QDs onto V_2O_5 nanowires by both SILAR and LAA had minimal impact on the decay kinetics of the 430 nm bleach. Values of $<\tau>$ for the bleach for CdSe/V_2O_5 heterostructures ranged from 70 to 150% of $<\tau>$ for V_2O_5 nanowires. Deposition of CdSe had a somewhat greater impact on decay kinetics of the 535 nm absorption band. For SILAR-derived heterostructures, $<\tau>$ for the absorption increased by approximately 3.3-fold relative to V_2O_5 nanowires. For LAA-derived CdSe/V_2O_5 heterostructures, $<\tau>$ decreased by approximately 1.6-fold for Cys-CdSe(sm) and increased by approximately 2-fold for Cys-CdSe(lg). Similarly to the CdSe/β-$Pb_{0.33}V_2O_5$ heterostructures, the increase in $<\tau>$ upon SILAR deposition of CdSe or LAA of Cys-CdSe(lg) QDs may have arisen from passivation of surface trap states on V_2O_5 nanowires.

TA decay traces of the long-wavelength transient absorption band observed for both SILAR- and LAA-derived CdSe/V_2O_5 are shown in Figure V. 8C and D. As previously discussed, the induced absorption observed exclusively for CdSe/V_2O_5 is assigned to trapped holes in oxidized CdSe QDs produced by the excited-state transfer of an electron from CdSe to V_2O_5.[203] Average lifetimes of $(1.0 \pm 0.8) \times 10^{-6}$, $(1.7 \pm 0.6) \times 10^{-7}$, and $(2.7 \pm 0.7) \times 10^{-7}$ s were determined for this long-wavelength absorption band of 5× SILAR CdSe/V_2O_5, LAA-derived Cys-CdSe(sm)/V_2O_5, and LAA-derived Cys-CdSe(lg)/V_2O_5 heterostructures, respectively. This absorption band is longer lived than the 535 nm absorption band of uncoated V_2O_5 ($(7 \pm 2) \times 10^{-8}$ s) and the excitonic bleach of dispersed Cys-CdSe(lg) QDs ($(5.9 \pm 0.2) \times 10^{-8}$ s) (Figure A. 16), supporting our assignment

of the band to a charge-separated state. The lifetimes of the 535 nm absorption band of uncoated V_2O_5 and the bleach of dispersed Cys-CdSe(lg) QDs are associated with excited states localized within a given material component. Charge-separated states are typically longer lived than localized excited states as the spatial separation between electron and hole is greater resulting in diminished overlap of their respective wave functions.[35,39,160]

V.3.6 Ultrafast Transient Absorption

Ultrafast transient absorption measurements were performed to examine excited-state dynamics on picosecond time scales and to directly observe charge-transfer processes. TA difference spectra for β-$Pb_{0.33}V_2O_5$, 3× SILAR CdSe/β-$Pb_{0.33}V_2O_5$, and Cys-CdSe(lg)/β-$Pb_{0.33}V_2O_5$ were extracted at 1 ps intervals over the first 5 ps following excitation (Figure V. 9). For β-$Pb_{0.33}V_2O_5$ nanowires, the transient absorption bands reached maximum amplitude within the instrument response time, as expected for TA signals derived from the direct photogeneration of an excited state in β-$Pb_{0.33}V_2O_5$. For 3× SILAR CdSe/β-$Pb_{0.33}V_2O_5$ and Cys-CdSe(lg)/β-$Pb_{0.33}V_2O_5$, the short-wavelength onsets of the absorption bands appear to be at full intensity within the temporal resolution of the measurement; however, distinct progressive rises of ΔA amplitude in the longer-wavelength regions of the absorption bands are discernible. This growth of absorption for 3× SILAR CdSe/β-$Pb_{0.33}V_2O_5$ occurs from approximately 525 to 650 nm, appearing as a broad growth of the entire longer-wavelength half of the absorption band. The rise in ΔA for Cys-CdSe(lg)/β-$Pb_{0.33}V_2O_5$ spans a smaller wavelength range, from

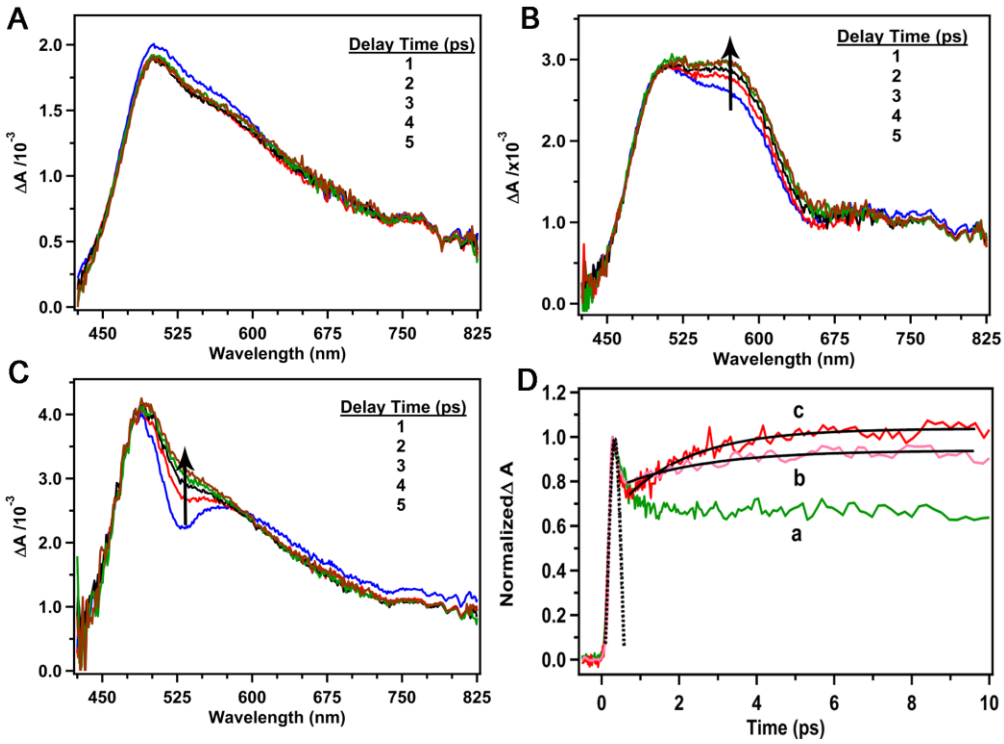

Figure V. 9 Ultrafast TA spectra of (A) β-$Pb_{0.33}V_2O_5$, (B) 3× SILAR CdSe/β-$Pb_{0.33}V_2O_5$, and (C) Cys-CdSe(lg)/β-$Pb_{0.33}V_2O_5$ with λ_{pump} = 360 nm and corresponding TA decay traces (D) for (a) β-$Pb_{0.33}V_2O_5$ (λ_{probe} = 525 nm), (b) 3× SILAR CdSe/β-$Pb_{0.33}V_2O_5$ (λ_{probe} = 565 nm), and (c) Cys-CdSe(lg)/β-$Pb_{0.33}V_2O_5$ (λ_{probe} = 525 nm). A Gaussian model of the excitation laser pulse is superimposed on the TA decay traces.

approximately 490 to 575 nm, with a local ΔA minimum at 535 nm in the TA spectra acquired at the shortest delay times of 1 and 5 ps.

The rise of ΔA across a specific spectral range, observed only upon interfacing with CdSe QDs, is logically attributed to contributions to the observed TA spectra from the decay of the bleach associated with the first excitonic ground-state absorption of the QDs. Considering that TA spectra of CdSe/β-$Pb_{0.33}V_2O_5$ are a combination of the signal from photoexcited β-$Pb_{0.33}V_2O_5$ and

CdSe, the CdSe bleach can reasonably be expected to contribute to the total measured ΔA. The TA spectrum of Cys-CdSe(lg) QDs dispersed in H_2O (Figure A. 16A) consists of a bleach of the ground-state absorption, with an onset at 575 nm and a minimum at 516 nm and shoulder minimum at 445 nm, corresponding to the first and second excitonic bands, respectively.[200–202] Indeed, the shape and position of the first-excitonic bleach are quite similar to the shape and position of the ΔA minimum observed in the TA spectrum of Cys-CdSe(lg)/β-$Pb_{0.33}V_2O_5$ (Figure V. 9C) at short delay times. As the CdSe bleach decays, its contribution to the total ΔA decreases and a net rise in ΔA is observed. It should be noted that a well-resolved bleach band was not observed in the TA spectrum of the SILAR-prepared sample due to a wide distribution of particle sizes inherent to the deposition method.[141] The broad rise in ΔA intensity observed is similar to what one would expect based on the ground-state absorbance of SILAR CdSe QDs on β-$Pb_{0.33}V_2O_5$ (Figure A. 15).

Apart from the contribution from the CdSe bleach, the transient absorption band appears to be at maximal amplitude instantaneously for both CdSe/β-$Pb_{0.33}V_2O_5$ samples. As previously discussed, this absorption band is associated with a hole located in the mid-gap states of β-$Pb_{0.33}V_2O_5$ nanowires and corresponds to excitation of an electron from deeper VB states. Therefore, we conclude that holes are transferred from the VB of CdSe to the mid-gap states of β-$Pb_{0.33}V_2O_5$ within the excitation pulse. If the hole-transfer reaction was slower, one would expect the absorption band to grow as hole transfer occurred. In

contrast, the time-resolvable decay of the first excitonic bleaches of CdSe(lg) and SILAR-derived CdSe QDs suggests that the transfer of electrons to the CB of β-$Pb_{0.33}V_2O_5$ occurs more slowly than the transfer of holes to the mid-gap states. Ultrafast TA decay traces (Figure V. 9D) show the rise in ΔA associated with the decay of the bleach from CdSe. The rise in ΔA was well-modeled by a single exponential function, and lifetimes of $(2.3 \pm 0.3) \times 10^{-12}$ s and $(1.8 \pm 0.1) \times 10^{-12}$ s were obtained for 3× SILAR CdSe/β-$Pb_{0.33}V_2O_5$ and Cys-CdSe(lg)/β-$Pb_{0.33}V_2O_5$, respectively. These lifetimes can be attributed to the tail-end of electron transfer from the CB edges of photoexcited CdSe QDs into the CB edge of β-$Pb_{0.33}V_2O_5$. Importantly, the transient bleach of free dispersed Cys-CdSe(lg) QDs, for which electron-hole recombination is the only excited-state deactivation pathway, decays with an average lifetime of $(5.9 \pm 0.2) \times 10^{-8}$ s (Figure A. 16B). Thus, the vastly accelerated bleach decays for the CdSe/β-$Pb_{0.33}V_2O_5$ samples, which give rise to the time-resolvable growth of the net absorption, are entirely consistent with a mechanism in which rapid electron transfer competes with intra-QD electron-hole recombination.

V.4 Conclusion

Transient absorption spectroscopy measurements of CdSe/β-$Pb_{0.33}V_2O_5$ heterostructures prepared by LAA and SILAR have provided compelling evidence that electrons were transferred from photoexcited CdSe QDs into the CB of β-$Pb_{0.33}V_2O_5$ nanowires, while holes were transferred into the mid-gap states of the nanowires. In

stark contrast, for CdSe/V_2O_5 heterostructures, only electron transfer from photoexcited QDs to CB states of V_2O_5 was observed. Ultrafast transient absorption measurements of CdSe/β-$Pb_{0.33}V_2O_5$ heterostructures suggest that holes were transferred more rapidly than electrons. Relevant time scales of interfacial charge transfer and electron-hole recombination pathways for CdSe/β-$Pb_{0.33}V_2O_5$ heterostructures are summarized in Figure V. 5. The efficient extraction of holes from photoexcited CdSe QDs (as required for applications such as water oxidation) can thus be facilitated by the presence of mid-gap states derived from intercalative cations.

Distinctive electron-transfer dynamics were observed for CdSe/V_2O_5 heterostructures depending on the nature of the interface. Electron transfer from CdSe QDs to β-$Pb_{0.33}V_2O_5$ nanowires occurred readily for heterostructures assembled *via* SILAR with direct interfaces; however, for heterostructures prepared by LAA and interfaced using molecular linkers, electron transfer was observed only for hot electrons produced with excitation at energies significantly greater than the bandgap of CdSe.

The results presented here demonstrate that charge transfer from photoexcited CdSe QDs to β-$Pb_{0.33}V_2O_5$ nanowires can compete successfully with electron-hole recombination pathways, suggesting the feasibility of using intercalative mid-gap states as acceptors of photogenerated holes. Such an approach would represent a fundamentally distinct design for enhancing charge transfer across interfaces. Future work will focus on the development of CdSe/β-$Pb_{0.33}V_2O_5$ hybrid photocathodes by incorporating an electron acceptor into the

heterostructures such that electron transfer to the acceptor might compete with electron injection into the CB of β-$Pb_{0.33}V_2O_5$.

CHAPTER VI

PROGRAMMING INTERFACIAL ENERGETIC OFFSETS IN β-$PB_{0.33}V_2O_5$/QUANTUM-DOT HETEROSTRUCTURES: TUNING VALENCE BAND EDGES TO OVERLAP WITH MID-GAP STATES

VI.1 Introduction

Nanoscale semiconductor heterostructures are of significant interest for solar energy conversion owing primarily to the tunability of the bandgaps and band-edge potentials of semiconductors as a function of composition and size.[39,125,204,205] In a typical heterostructure configuration, agnostic of the mode of growth, a light-harvesting semiconductor nanoparticle (excited-state charge donor) is interfaced with a wide-bandgap semiconductor (charge acceptor), and photogenerated charge carriers are transferred across the interface.[132,176,206] To achieve efficient solar energy conversion, the separation of excited electrons and holes must occur more rapidly than excited-state relaxation, and subsequent charge-transport or redox photocatalytic steps must outcompete charge recombination. The kinetics of charge separation depend on the thermodynamic driving force, which is dictated by interfacial energetic offsets of electron-donating and accepting states. Consequently, the design of nanoscale semiconductor heterostructures for charge transfer and energy conversion requires careful consideration of interfacial energetic offsets.[63,177,180] The tunability of electronic structure that is accessible in semiconductor quantum dots (QDs) provides a powerful adjustable parameter for achieving heterostructures with desired energetic offsets.

Recently, we demonstrated a promising tunable platform for light-harvesting and excited-state charge transfer derived from interfacing β-$Pb_{0.33}V_2O_5$ nanowires (NWs) with CdSe QDs.[46,47] This platform exploits a distinctive feature in the electronic structure of ternary vanadium oxide bronzes: the presence of intrinsic mid-gap states derived from the intercalating cations that are situated between the valence and conduction band edges.[52,60] In the case of β-$Pb_{0.33}V_2O_5$, mid-gap states are derived from Pb 6s-O 2p antibonding interactions.[48,49] The energies and occupancies of these mid-gap states are tunable through the choice of intercalating cation and cation stoichiometry.[49,188] Since the intercalating cations are homogeneously incorporated within the quasi-1D crystal structure, such states constitute an integral part of the electronic structure and are quite distinct from mid-gap states derived from defects or dopants. Hard X-ray photoemission spectroscopy measurements revealed substantial energetic overlap between the mid-gap states of β-$Pb_{0.33}V_2O_5$ and valence-band states of CdSe, suggesting that the transfer of photogenerated holes from the valence band of CdSe into the mid-gap states of β-$Pb_{0.33}V_2O_5$ is possible.[46] Recently, hole transfer was measured experimentally using transient absorption spectroscopy; these measurements revealed that photoexcitation of CdSe QDs was followed by hole transfer to the mid-gap states on time scales less than one ps.[47] However, the valence band edge of CdSe QDs was measured to lie ca. 0.7 eV higher in energy than the highest-energy mid-gap states of β-$Pb_{0.33}V_2O_5$ NWs. Therefore, the transfer of thermalized holes at the valence band edge of CdSe QDs to the mid-gap states of β-$Pb_{0.33}V_2O_5$ NWs was thermodynamically unfavorable.[46]

The size- and composition-dependent electronic structure of QDs is advantageous when designing heterostructures with desirable interfacial energetic offsets and tunable driving forces for excited-state charge transfer.[125,132] In this letter, we demonstrate that an improved driving force for hole transfer in QD/NW heterostructures is obtained by replacing CdSe QDs with CdS QDs of the appropriate dimensionality as light-harvesters and excited-state hole donors. The valence band edge of bulk CdS is ca. 0.5 eV lower in energy than that of bulk CdSe;[207,208] and indeed this is the basis for our hypothesis that replacing CdSe with CdS will increase the energetic overlap of valence-band states of QDs with mid-gap states of β-$Pb_{0.33}V_2O_5$ NWs, thereby rendering such interfaces more suitable for excited-state charge separation. Interfacial energetic offsets have been examined for heterostructures with distinctive sizes and modes of attachment of CdS and CdSe QDs.

Specifically, CdS/β-$Pb_{0.33}V_2O_5$ heterostructures have been prepared using two distinct routes: linker-assisted assembly (LAA) and successive ionic layer adsorption and reaction (SILAR).[46] Cysteinate (Cys)-capped CdS QDs with average diameters of ca. 2.6 nm (hereafter referred to as Cys-CdS(sm)) and ca. 3.8 nm (Cys-CdS(lg)), as determined from maxima of the first excitonic absorption bands,[152] were used for LAA. Cys acts as a bifunctional linker molecule, preferentially binding to Cd^{2+} sites *via* the thiolate functional group and to β-$Pb_{0.33}V_2O_5$ through an electrostatic interaction between the positively charged, protonated amine of Cys and the negatively charged, hydroxylated surface of β-$Pb_{0.33}V_2O_5$.[46] For SILAR-derived heterostructures, CdS QDs were grown directly onto β-$Pb_{0.33}V_2O_5$ NWs by immersing the NWs first in a Cd^{2+}

precursor solution followed by a Se^{2-} precursor solution, constituting a single SILAR cycle. Multiple iterations of SILAR (1× and 3× are hereafter used to designate one and three cycles, respectively) allow for tunability of the size of the QDs and their loading on the NWs. To enable direct comparison of interfacial energetics as a function of the composition of QDs, we prepared analogous CdSe/β-$Pb_{0.33}V_2O_5$ heterostructures both *via* LAA and SILAR, as reported previously.[46]

VI.2 Experimental

VI.2.1 Synthesis of β-$Pb_{0.33}V_2O_5$ Nanowires

β-$Pb_{0.33}V_2O_5$ NWs were prepared using a one-step hydrothermal reaction as previously reported.[48] In brief, stoichiometric amounts of $Pb(CH_3COO)_2 \cdot 3H_2O$ and V_2O_5 were placed in a polytetrafluoroethylene-lined acid digestion vessel (Parr) along with 16 mL of deionized (DI) water. The vessel was sealed in an autoclave and heated to 250 °C for 72 h. The product was isolated by vacuum filtration, washed with water, and allowed to dry in air.

VI.2.2 Synthesis of Cys-CdSe Quantum Dots

Cys-CdSe(sm) QDs were synthesized as previously reported.[147] The selenium precursor was prepared by refluxing an aqueous solution of Se powder and Na_2SO_3 overnight, and the cadmium precursor was an aqueous solution of $3CdSO_4 \cdot 8H_2O$ and cysteine. The pH of the cadmium precursor was titrated to 12.5 to 13.0 with solid NaOH. The hot selenium precursor was added to the cadmium precursor and allowed to stir for 30 min. The resulting dispersions of Cys-CdSe(sm) QDs were purified by solvent/non-

solvent (H_2O/MeOH, 3:1) washing to remove excess reagents. Cys-CdSe(lg) QDs were synthesized and purified by the same procedure, except that the cadmium precursor was heated to, and maintained at, 80ºC for the duration of the experiment (2 h).

VI.2.3 Synthesis of Cys-CdS Quantum Dots

Cys-CdS QDs were prepared using a modification of the synthesis procedure for Cys-CdSe QDs. A sulfur precursor solution was prepared by adding sodium thiosulfate (1.17 g, 7.41 mmol) to 25 mL DI water in a 50 mL round bottom flask and heating to reflux for 30 min. For Cys-CdS(sm) QDs, the cadmium precursor was an aqueous solution (10.5 mL) of cadmium sulfate octahydrate (0.433 g, 1.69 mmol) and cysteine (1.02 g, 8.44 mmol). The pH of the solution was titrated to 12.5 - 13.0 with solid NaOH. The hot sodium thiosulfate solution (4.5 mL) was added to the cadmium precursor with stirring. The reaction was allowed to stir overnight (12-16 h) resulting in the formation of a cloudy, white suspension of flocculated Cys-CdS(sm) QDs. For Cys-CdS(lg) QDs, the cadmium precursor was an aqueous solution (21 mL) of cadmium sulfate octahydrate (0.866g, 3.38 mmol) and cysteine (2.05 g, 16.88 mmol). The pH of the solution was titrated to 12.5 - 13.0 with solid NaOH. The cadmium precursor was then heated to 80ºC and the hot sodium thiosulfate solution (9 mL) was added with stirring. The reaction was allowed to continue heating for 4 h with stirring, resulting in the formation of a cloudy, yellow suspension of flocculated Cys-CdS(lg) QDs. Typical concentrations of cadmium, sulfur, and Cys in the reaction mixtures for both Cys-CdS(sm) and Cys-CdS(lg) were 113, 90, and 563 mM, respectively. Dispersions of both Cys-CdS(sm) and Cys-CdS(lg) QDs were purified by solvent/non-solvent washing to remove excess

reagents. First, 5 mL of the flocculated QDs were centrifuged to isolate the QDs and the supernatant was discarded. The pellet of QDs was then fully dispersed into 10 mL DI water resulting in a clear dispersion. Then, 30 mL of methanol was added to the dispersion of QDs, resulting in the flocculation of QDs. The flocculate was then centrifuged again to isolate the QDs, supernatant was discarded, and the QDs were redispersed into 10 mL DI water. This process was repeated once for a total of two purification cycles.

VI.2.4 SILAR Prepared CdSe/β-$Pb_{0.33}V_2O_5$ and CdS/β-$Pb_{0.33}V_2O_5$ Heterostructures

CdSe deposited directly onto β-$Pb_{0.33}V_2O_5$ NWs were prepared via SILAR using previously a reported method.[46] In a single SILAR cycle, CdSe QDs were grown directly onto β-$Pb_{0.33}V_2O_5$ by sequentially mixing the NWs with a cadmium precursor solution ($Cd(NO_3)_2$ in ethanol), followed by a selenium precursor (Na_2Se in ethanol). The NWs were washed with ethanol following each mixing step to remove excess ions. SILAR-prepared CdS/β-$Pb_{0.33}V_2O_5$ heterostuctures were prepared using a modification of this procedure. A 50 mM solution of Na_2S was prepared by dissolving $Na_2S{\cdot}9H_2O$ in ethanol. Meanwhile, β-$Pb_{0.33}V_2O_5$ NWs (50 mg) were dispersed in 15 mL ethanol and a 100 mM solution of $Cd(NO_3)_2{\cdot}4H_2O$ was prepared in ethanol. All solutions were placed in a glovebag filled with Ar gas. To begin the SILAR cycle, the NW dispersion was mixed with the $Cd(NO_3)_2$ solution, thus bringing the concentration of $Cd(NO_3)_2$ to 50 mM. The solution was stirred for 30 s and the NWs were then removed through centrifugation at 6500 rpm for 90 s. Subsequently, the NWs were washed with 10 mL of ethanol for 30 s and centrifuged. Next, the NWs were mixed with the Na_2S solution for

30 s, centrifuged and isolated, and washed again with 10 mL of ethanol. This final washing step concludes one SILAR cycle.

VI.2.5 Linker-Assisted Assembly of Cys-CdSe/β-$Pb_{0.33}V_2O_5$ Heterostructures

Cys-CdSe(sm)/β-$Pb_{0.33}V_2O_5$ and Cys-CdSe(lg)/β-$Pb_{0.33}V_2O_5$ heterostructures were prepared *via* LAA as reported previously.[46] An aqueous dispersion of β-$Pb_{0.33}V_2O_5$ NWs was added to an aqueous dispersion of purified Cys-CdSe(sm) or Cys-CdSe(lg) QDs and allowed to equilibrate overnight (12—16 h). CdSe-functionalized NWs were recovered by centrifugation, rinsed with DI water to remove excess QDs, and dried at room temperature before characterization.

VI.2.6 Linker-Assisted Assembly of Cys-CdS/β-$Pb_{0.33}V_2O_5$ Heterostructures

Cys-CdS/β-$Pb_{0.33}V_2O_5$ heterostructures were prepared using a modification of the LAA method employed for formation of Cys-CdSe/β-$Pb_{0.33}V_2O_5$ heterostructures. β-$Pb_{0.33}V_2O_5$ NWs (10 mg) were dispersed in DI water (10 mL) in a 20 mL scintillation vial. The dispersion was sonicated for 20 min to maximize the amount of dispersed NWs. An aqueous dispersion of either purified Cys-CdS(sm) QDs or purified Cys-CdS(lg) QDs (1 mL) was added to the dispersion of β-$Pb_{0.33}V_2O_5$ NWs and allowed to equilibrate overnight (12-16 h). Cys-CdS(sm)/β-$Pb_{0.33}V_2O_5$ or Cys-CdS(lg)/β-$Pb_{0.33}V_2O_5$ heterostructures were recovered *via* centrifugation and then rinsed with DI water to remove excess QDs. The heterostructures were dried at room temperature before characterization.

VI.2.7 Characterization Methods and Instrumentation

Scanning electron microscopy (SEM) was performed using a JEOL JSM-7500F operated at 5 keV. Samples were prepared for SEM by spreading synthesized samples on carbon tape. High-resolution transmission electron microscopy (HRTEM), selected area electron diffraction (SAED) measurements, and energy dispersive X-ray spectroscopy (EDS) were performed with a FEI Tecnai G2 F20 FE-TEM operated at 200 keV equipped with an EDAX instruments EDS detector. Samples were prepared for TEM by dispersing samples in ethanol and drop-casting onto carbon-coated copper grids.

Raman spectra of solid-phase powders of SILAR CdS/ β-$Pb_{0.33}V_2O_5$ and Cys-CdS QDs was obtained with a Jobin-Yvon Horiba Labram HR800 instrument coupled to an Olympus BX41 microscopy using the 514.5 nm laser excitation from an Ar-ion laser. Cys-CdS QDs were dispersed in water and drop-casted onto a gold-coated silicon pyramids to enhance Raman signal. The preparation of substrates for surface enhanced Raman spectroscopy has been discussed in previous work.[209]

X-ray photoemission spectroscopy (XPS) measurements were performed using a Phi VersaProbe 5000 system with a monochromated Al Kα source and hemispherical analyzer at the Analytical and Diagnostics Laboratory (ADL) at Binghamton University. The valence band region was measured with a pass energy of 23.5 eV, and a flood gun was used to achieve charge neutralization. Valence band spectra were energy aligned to the Cd 4d peak at 11 eV.

VI.3 Results and Discussion

The CdS/β-$Pb_{0.33}V_2O_5$ heterostructures were characterized by electron microscopy, electron diffraction, and Raman spectroscopy (Figure VI. 1). Transmission electron microscopy (TEM) images of 3× SILAR-derived CdS/β-$Pb_{0.33}V_2O_5$ heterostructures reveal a continuous shell of QDs around the NWs (Figure VI. 1A). TEM images of LAA-derived Cys-CdS(lg)/β-$Pb_{0.33}V_2O_5$ heterostructures similarly reveal a continuous overlayer of Cys-CdS QDs with resolvable lattice fringes indexed to the separation between the (112) planes of wurtzite CdS (Joint Committee on Powder Diffraction Standards (JCPDS) #41-1049). Selected area electron diffraction (SAED) of Cys-CdS(lg)/β-$Pb_{0.33}V_2O_5$ heterostructures yields a complex pattern with reflections from both β-$Pb_{0.33}V_2O_5$ and wurtzite CdS (Figure VI. 1E). The diffuse diffraction ring can be indexed to the (101) plane of wurtzite CdS, consistent with our assignment of the lattice fringes observed in the TEM image. The other reflections are indexed to β-$Pb_{0.304}V_2O_5$ (JCPDS #41-1426).[46,48] Energy-dispersive X-ray spectroscopy (EDS) spectra confirm the presence of Cd and S in the heterostructures (Figure A. 18) and this was further verified by X-ray photoelectron spectroscopy (XPS) survey scans. Scanning electron microscopy (SEM) images of SILAR- and LAA-derived heterostructures (Figure VI. 1C, D) indicate speckled nanowires with homogeneous QD coverage along their entire lengths.

To further verify the phase assignment of CdS QDs, the SILAR-prepared heterostructures and dispersed Cys-CdS(sm) and Cys-CdS(lg) QDs were characterized by surface enhanced Raman spectroscopy (Figure VI. 1F) by inclusion of the materials

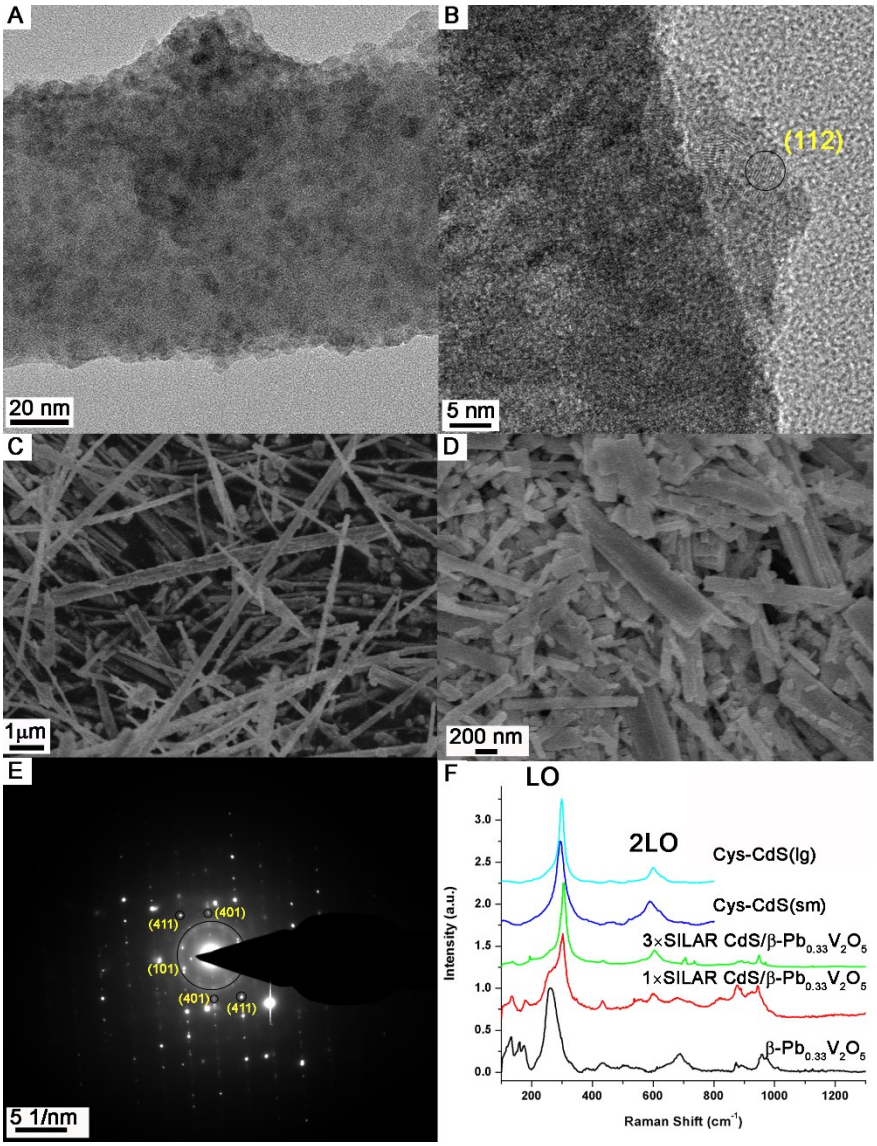

Figure VI. 1 A) TEM image of 3× SILAR CdS/β-$Pb_{0.33}V_2O_5$; B) TEM image of Cys-CdS(lg)/β-$Pb_{0.33}V_2O_5$ with the separation between the lattice planes indexed to wurtzite CdS; C) SEM image of 3× SILAR CdS/β-$Pb_{0.33}V_2O_5$; D) SEM image of Cys-CdS(lg)/β-$Pb_{0.33}V_2O_5$; E) SAED of Cys-CdS(lg)/β-$Pb_{0.33}V_2O_5$ indexed to the wurtzite phase of CdS (JCPDS #41-1049) and β-$Pb_{0.33}V_2O_5$ (JCPDS # 41-1426); F) Raman spectra of dispersed Cys-CdS QDs and SILAR-derived heterostructures acquired with 514.5 nm excitation from an Ar-ion laser.

within pyramidal gold substrates.[209] Raman spectra of aqueous dispersions of Cys-CdS

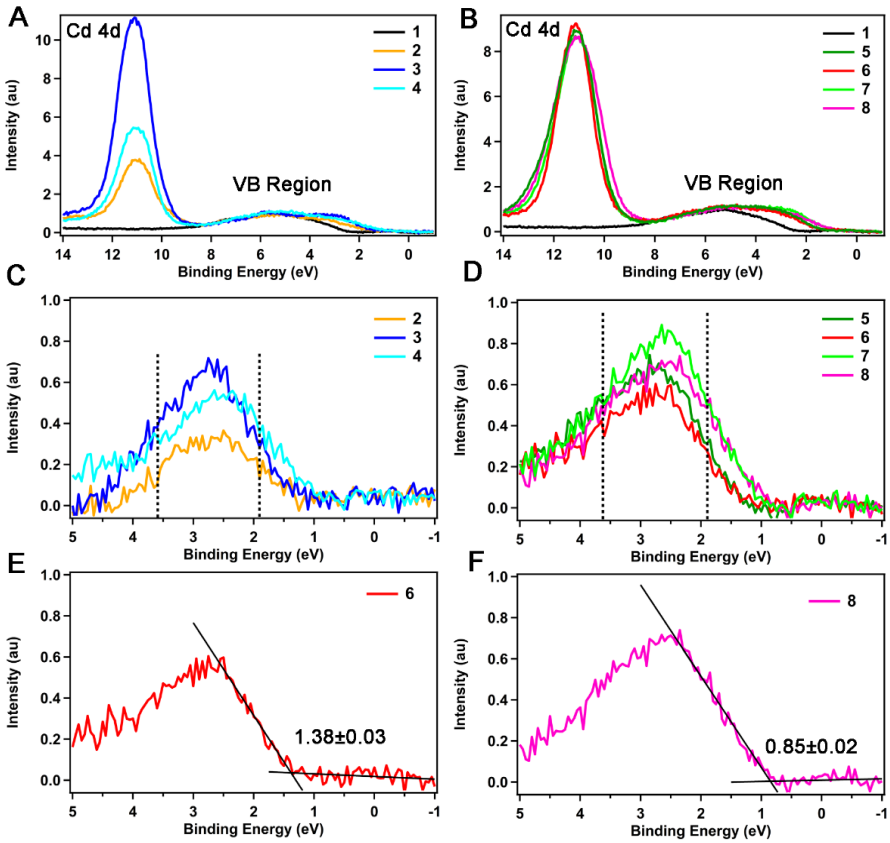

Figure VI. 2 Legend: 1. β-$Pb_{0.33}V_2O_5$ 2. 1× SILAR CdS/β-$Pb_{0.33}V_2O_5$ 3. 3× SILAR CdS/β-$Pb_{0.33}V_2O_5$ 4. 3× SILAR CdSe/β-$Pb_{0.33}V_2O_5$ 5. Cys-CdS(lg)/β-$Pb_{0.33}V_2O_5$ 6. Cys-CdS(sm)/β-$Pb_{0.33}V_2O_5$ 7. Cys-CdSe(lg)/β-$Pb_{0.33}V_2O_5$ 8. Cys-CdSe(sm)/β-$Pb_{0.33}V_2O_5$ A) Valence band spectra of QD/β-$Pb_{0.33}V_2O_5$ SILAR heterostructures; B) Valence band spectra of QD/β-$Pb_{0.33}V_2O_5$ LAA heterostructures; C) Difference spectra of SILAR heterostructures; D) Difference spectra of LAA heterostructures; E) Difference spectra of Cys-CdS(sm)/β-$Pb_{0.33}V_2O_5$ with linear fits and valence band edge value; F) Difference spectra of Cys-CdSe(sm)/β-$Pb_{0.33}V_2O_5$ with linear fits and valence band edge value.

QDs exhibit a sharp, intense band at 300 cm^{-1} and a broader, less intense band at 600 cm^{-1}, which are assigned to the bulk longitudinal optical (LO) and second-order longitudinal optical (2LO) modes, respectively, of wurtzite CdS.[210] Raman spectra of SILAR-prepared CdS/β-$Pb_{0.33}V_2O_5$ heterostructures reveal the emergence of both the LO and

2LO modes of wurtzite CdS on top of the characteristic modes of bare β-$Pb_{0.33}V_2O_5$ NWs, which have been assigned previously.[46] The CdS phonon modes are increased in intensity for the 3× SILAR-derived heterostructures as compared to the 1× SILAR-derived heterostructures, suggesting an increased thickness of the CdS QD overlayer with multiple SILAR iterations.[46]

In order to measure the energetic offsets between the valence band edges of the QDs and the mid-gap states of β-$Pb_{0.33}V_2O_5$, XPS measurements were performed as a function of the composition of QDs and their mode of attachment to the NWs. The valence band spectra of SILAR- and LAA-derived QD/NW heterostructures (overlaid with the spectrum of bare β-$Pb_{0.33}V_2O_5$ NWs) are shown in Figure VI. 2A and B, respectively. The valence band spectrum of β-$Pb_{0.33}V_2O_5$ NWs is characterized by a broad peak between 2 and 9 eV, which is derived primarily from O 2p non-bonding states.[46,48,49] The lower photoelectron cross-section of Pb 6s compared to O 2p at Al Kα energies precludes direct observation of mid-gap states in valence band XPS spectra. However, hard X-ray photoemission spectroscopy (HAXPES) measurements indicate a feature in the 1.8—3.6 eV range corresponding to Pb 6s—O 2p anti-bonding interactions that give rise to the mid-gap state.[49] The energy dispersion of these states is denoted in Figure VI. 2C and D by dashed vertical lines. To highlight changes in the electronic structure upon interfacing β-$Pb_{0.33}V_2O_5$ NWs with CdS QDs and to correct for Fermi level shifts, all valence band spectra were baseline-corrected, aligned, and normalized to the intensity of the O 2p nonbonding state at ca. 5 eV below an effective Fermi level (0 eV). Such an alignment enables the calculation of difference spectra and provides a

gauge of the change in ionization potential since the primary O 2p feature is considered to be constant at a fixed ionization potential of ca. 8 eV below the vacuum level. We note that using this methodology, the Cd 4d semi-core level features for the coated samples in Figure VI. 2 are at the same energy, which is consistent with the idea of a fixed ionization potential. For both LAA and SILAR-coated heterostructures, distinctive features emerge in close proximity of the energy levels demarcated as $Pb_{0.33}V_2O_5$ mid-gap states as a result of S 3p and Se 4p contributions from the CdS and CdSe QDs, respectively. The Se 4p and S 3p features are much more clearly discernible at Al Kα energies in contrast to HAXPES due to their orbital cross-section variations between these photon energies.[49,211] Difference spectra were obtained by subtracting the valence band spectrum of bare β-$Pb_{0.33}V_2O_5$ NWs from the spectrum of each QD/β-$Pb_{0.33}V_2O_5$ heterostructure. Such spectra are plotted in Figure VI. 2C and D for SILAR- and LAA-prepared heterostructures, respectively, and allow for easier visualization of relative shifts in energetic offsets.

For the LAA samples that have approximately monolayer or sub-monolayer coverage of QDs, the Cd 4d levels are of comparable intensity for all of the samples (Figure VI. 2B). The specific mode of attachment, which requires Cys to function as a bifunctional linker, limits the formation of thicker shells. In contrast, for the SILAR samples, the relatively greater thickness of the 3× samples as compared to the 1× samples is reflected in the stronger Cd 4d core level feature observed in Figure VI. 2A. The 3× SILAR CdSe/β-$Pb_{0.33}V_2O_5$ heterostructures have a coating thickness intermediate between the 1× and 3× CdS/β-$Pb_{0.33}V_2O_5$ analogs. Numerical values of the

valence band onsets were determined from intercepts of linear fits to the baseline and the low-energy part of the difference spectra as depicted in Figure VI. 2E and F for LAA-prepared heterostructures comprising β-$Pb_{0.33}V_2O_5$ NWs interfaced with CdS(sm) and

Table VI. 1. Experimentally determined valence band onsets for CdSe and CdS/β-$Pb_{0.33}V_2O_5$ heterostructures

Sample	Valence Band Edge (eV)
Cys-CdS/β-$Pb_{0.33}V_2O_5$	1.33±0.03
SILAR CdS/β-$Pb_{0.33}V_2O_5$	1.32±0.03
Cys-CdSe/β-$Pb_{0.33}V_2O_5$	0.92±0.02
SILAR CdSe/β-$Pb_{0.33}V_2O_5$	0.94±0.02

CdSe(sm) QDs, respectively.[212] Figure A. 19 shows fits obtained for LAA-prepared heterostructures comprising larger QDs as well as heterostructures prepared by SILAR. Since the differences in valence band onsets as a function of size are much smaller relative to the differences induced by changing the QD composition from CdSe to CdS (quantum confinement affects the conduction band edge to a much greater extent than the valence band edge), the valence band onsets have been averaged for the LAA and SILAR heterostructures in each case.[213,214] Table VI. 1 summarizes these valence band edge values. Several findings are immediately apparent from analysis of the valence band spectra. First, both the difference spectra (Figure VI. 2B, C) and the extrapolated onset values (Table VI. 1) indicate that the valence band onset of CdS QDs (1.33±0.03

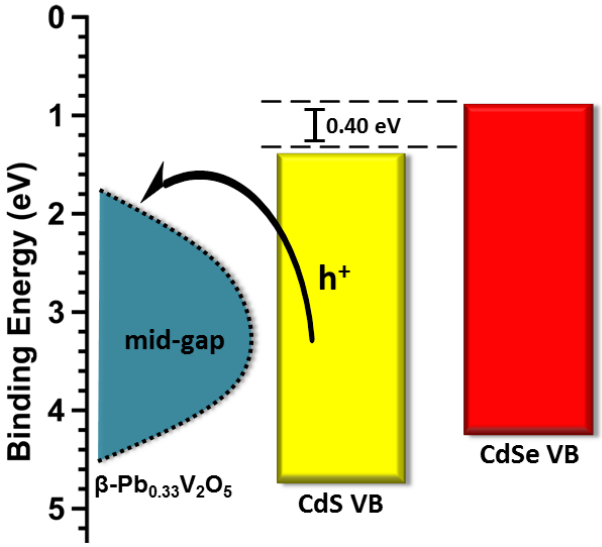

Figure VI. 3 Schematic of the valence band edge shift of Cys-CdSe *versus* Cys-CdS and hole transfer into the mid-gap states of β-$Pb_{0.33}V_2O_5$.

eV) is shifted to higher binding energies relative to CdSe QDs for LAA-prepared heterostructures (0.92±0.02). The observed increase in binding energy onset implies a more strongly bound state and can be directly correlated to the valence band edge of CdS (primarily S 3p in origin) being positioned at a relatively lower energy as compared to CdSe (primarily Se 4p in origin) on an energy scale where occupied states are negative and unoccupied states are positive with respect to a Fermi level of 0 eV. The relatively deeper valence band of CdS is a direct result of the higher electronegativity of sulfur, which further yields a more ionic lattice with relatively less hybridization of S and Cd-derived states. A very similar trend is also noted for the SILAR CdS (1.32±0.03 eV) and SILAR CdSe (0.94±0.02) samples. As evident in Figure VI. 2C and D, an immediate consequence of the shift of the valence band to higher energies for CdS is a much improved overlap with the mid-gap states of β-$Pb_{0.33}V_2O_5$.

Taking the intercept as a close approximation to the valence band onset, the valence band edge of Cys-CdS is shifted ca. 0.41 eV lower in energy than the Cys-CdSe valence band edge. Similarly, for SILAR-prepared heterostructures, there is a ca. 0.38 eV decrease in the valence band edge of CdS relative to CdSe. These experimentally determined differences in valence band edge energies of CdS and CdSe, for both SILAR- and LAA-prepared heterostructures, are in reasonable agreement with reported energy differences (ca. 0.5 eV) for the band edges of bulk CdS and CdSe.[207,208]

The above discussion clearly indicates that the valence band edge of CdS QDs is lower in energy compared to CdSe QDs, suggesting a decrease in the thermodynamic barrier to hole injection from the valence band edge of the QDs into the mid-gap states of β-$Pb_{0.33}V_2O_5$ as shown in Figure VI. 3. The thermodynamic barrier for hole injection from QDs to the mid-gap states of β-$Pb_{0.33}V_2O_5$ is estimated from the energy difference between the valence band edge of the QDs and the onset of the mid-gap states at ca. 1.8 eV. Thermodynamic barriers of ca. 0.47 eV and ca. 0.88 eV were estimated for hole injection from the band edges of Cys-CdS and Cys-CdSe QDs, respectively, suggesting a 0.40 eV decrease in the barrier for hole injection from CdS. Importantly, the shift of the valence band of CdS to lower energy than that of CdSe renders hole transfer to mid-gap states of β-$Pb_{0.33}V_2O_5$ NWs thermodynamically favorable from a much greater fraction of states within the valence band.

VI.4 Conclusion

In summary, we have synthesized CdS/β-$Pb_{0.33}V_2O_5$ heterostructures through both SILAR and LAA methods. TEM and SEM images revealed a continuous shell of CdS QDs on the surface of β-$Pb_{0.33}V_2O_5$ NWs. SAED and Raman spectroscopy confirmed the wurtzite crystal structure of the CdS. XPS valence band measurements on CdS/β-$Pb_{0.33}V_2O_5$ and CdSe/β-$Pb_{0.33}V_2O_5$ have demonstrated that the valence band edge of CdS QDs is lower in energy relative to CdSe QDs, suggesting a ca. 40 eV decrease in the thermodynamic barrier for hole injection from the valence band edge of the QDs and a significant increase of the fraction of valence band states that can inject holes into the NWs. The approach demonstrated here suggests that the tunability of the electronic structure of semiconductor QDs provides an important adjustable parameter for improving charge separation across interfaces.

CHAPTER VII

CONCLUSION

In this dissertation, the modification of vanadium oxides for energy saving applications was explored. Chapter II explores the interfacing of vanadium dioxide nanowires to glass substrates through a modified Stöber method for potential application as thermochromic films. First, amorphous silica shells were formed on hydrothermally grown VO_2 nanowires. These shells provided protection from oxidation, while not impeding the positive properties of VO_2, mainly the MIT which includes a change from infrared transparent to infrared reflective as a result of temperature. The $VO_2@SiO_2$ particles were investigated using TEM, SEM, Raman spectroscopy, and DSC. Upon successful shell deposition, the method was modified further to allow for deposition onto glass slides. ASTM standardized testing as well as SEM imaging showed that the modified Stöber method used successfully adhered VO_2 nanowires to glass substrates using a silica matrix.

Expanding on this research, Chapter III investigates the effect of size on the visible and NIR transmission of a polymer composite containing $VO_2@SiO_2$ particles. Four different sizes of particles were explored, ranging from wires microns in length with diameters of ca. 300 nm to spherical particles with diameters ca. 10 nm. The nanocrystals were dispersed in an Acrysol polymer solution and cast onto glass slides. Transmission data was collected for three concentrations of films and showed that the largest particles showed good NIR modulation but poor visible transmittance. In

contrast, the ultrasmall particles had excellent NIR modulation while maintaining high visible transmittance. With this work, we show that VO_2 nanocrystals could be used as thermochromic films, with optimization of particle size and film formation.

In future endeavors, further studies will be performed on the optimization of the polymeric formulation films, with focus on the ultra-small VO_2 particles. More films with varying concentrations will be made and their thermochromic properties tested. Through these experiments, a correlation curve can be produced showing the effects concentration has on the visible transmission, near-infrared modulation, and the onset of this modulation.

Once an optimum concentration has been reached, a variety of tests will be performed on the films. These tests will focus on the long term stability of the films, thus determining their viability for application to windows. Long term stability tests include film adhesion, effects of humidity, as well as long-term thermal cycling.

In addition to vanadium dioxide, heterostructures of vanadium oxide bronzes paired with quantum dots were studied for energy conversion applications. Chapter IV begins this research by integrating CdSe quantum dots with β-$Pb_xV_2O_5$ nanowires. Two synthetic methods were used to synthesize these heterostructures: linker-assisted assembly and successive ionic layer adsorption and reaction. Heterostructures were characterized by a variety of methods including TEM, SEM, EDX, and Raman spectroscopy to confirm the formation of a quantum dot shell on the nanowires. Following confirmation of the quantum dot growth, HAXPES studies were performed to determine the overlap of the valence band of the QDs and the mid-gap of the nanowires.

It was found that heterostructures grown through both methods were shown to have good overlap with the mid-gap of β-$Pb_xV_2O_5$. In addition, spectroelectrochemical experiments showed that the CdSe/β-$Pb_xV_2O_5$ heterostructures had longer lifetimes than CdSe/V_2O_5 heterostructures, which do not possess a mid-gap state.

To confirm the transfer of holes from quantum dots to the mid-gap of the nanowires, extensive transient absorption studies were performed. Chapter V explores the experiments performed. Significant evidence of hole transfer from the valence bands of the excited quantum dots to the mid-gap states of the nanowires was seen. To confirm that the presence of the mid-gap state is essential for hole transfer, QD/V_2O_5 heterostructures were characterized as well and no hole transfer was evidenced in these heterostructures. The transfer of electrons to the conduction bands of both nanowires was seen, however, ultrafast measurements showed that holes were transferred more rapidly than the electrons in the β-$Pb_xV_2O_5$. These results show that the hole transfer from QDs to the nanowires competes with other charge recombinations and these heterostructures could be used for photoelectrochemical cells.

As a final study, CdS/β-$Pb_xV_2O_5$ heterostructures were synthesized using both LAA and SILAR methods. These heterostructures showed that the synthesis can be modified to optimize the hole transfer. Again, TEM, SEM, and Raman spectroscopy were used to characterize the structures, which showed successful synthesis of CdS QDs on the surface of the nanowires. XPS studies showed that the valence band of CdS was better aligned with the mid-gap state of β-$Pb_xV_2O_5$ than the valence band of CdSe. This shows that holes can more efficiently be transferred from the QD valence band to the

mid-gap state of β-$Pb_xV_2O_5$. Through this work, we designed a platform that can be easily modified for effective hole transfer.

In the future, we plan to study the CdS/ β-$Pb_xV_2O_5$ heterostructures using transient absorption spectroscopy. In this way, we can compare the two heterostructures for the rate of hole and electron transfer to determine which heterostructure should be studied further. Further studies will include oxygen evolution experiments, a more simplified variation of a photocatalytic cell, and, if positive results are seen, attempts at making a photocatalytic cell will be pursued.

When looking at what new heterostructures should be synthesized, new β-$M_xV_2O_5$ (where M=Tl and Sn) bronzes are being studied to determine experimentally if they too possess mid-gap states. Once the energy of the mid-gap states (if they exist) are determined, the nanowires will be paired with suitable quantum dots and the heterostructures studied through TEM, SEM, Raman spectroscopy, HAXPES, and transient absorption spectroscopy.

REFERENCES

1 J. Galy, *J. Solid State Chem.*, 1992, **100**, 229–245.

2 Y. Ueda, M. Isobe and T. Yamauchi, *J. Phys. Chem. Solids*, 2002, **63**, 951–955.

3 P. M. Marley, G. A. Horrocks, K. E. Pelcher and S. Banerjee, *Chem. Commun.*, 2015, **51**, 5181–5198.

4 C. Wu, F. Feng and Y. Xie, *Chem. Soc. Rev.*, 2013, **42**, 5157–83.

5 Y. Zhou and S. Ramanathan, *Crit. Rev. Solid State Mater. Sci.*, 2013, **38**, 286–317.

6 C. J. Patridge, T.-L. Wu, C. Jaye, B. Ravel, E. S. Takeuchi, D. A. Fischer, G. Sambandamurthy and S. Banerjee, *Nano Lett.*, 2010, **10**, 2448–53.

7 Z. Yang, C. Ko and S. Ramanathan, *Annu. Rev. Mater. Res.*, 2011, **41**, 337–367.

8 J. Sun, X. Li, Q. Zhao, J. Ke and D. Zhang, *J. Phys. Chem. C*, 2014, **118**, 10113–10121.

9 R. Baddour-Hadjean, J. P. Pereira-Ramos, C. Navone and M. Smirnov, *Chem. Mater.*, 2008, **20**, 1916–1923.

10 Y. Gao, S. Wang, H. Luo, L. Dai, C. Cao, Y. Liu, Z. Chen and M. Kanehira, *Energy Environ. Sci.*, 2012, **5**, 6104.

11 A. L. Pergament, G. B. Stefanovich and A. A. Velichko, *J. Sel. Top. Nano Electron. Comput.*, 2013, **1**, 24–43.

12 F. J. Morin, *Phys. Rev. Lett.*, 1959, **3**, 34–36.

13 L. Whittaker, C. J. Patridge and S. Banerjee, *J. Phys. Chem. Lett.*, 2011, **2**, 745–758.

14 A. Zylbersztejn and N. F. Mott, *Phys. Rev. B*, 1975, **11**, 4383–4394.

15 N. F. Mott, *Metal-Insulator Transitions*, CRC Press, Boca Raton, FL, 2nd edn., 1990.

16 M. Imada, A. Fujimori and Y. Tokura, *Rev. Mod. Phys.*, 1998, **70**, 1039–1263.

17 W.-T. Liu, J. Cao, W. Fan, Z. Hao, M. C. Martin, Y. R. Shen, J. Wu and F. Wang, *Nano Lett.*, 2011, **11**, 466–70.

18 L. Whittaker, H. Zhang and S. Banerjee, *J. Mater. Chem.*, 2009, **19**, 2968.

19 V. Eyert, *Ann. Phys.*, 2002, **11**, 650–702.

20 C. Kübler, H. Ehrke, R. Huber, R. Lopez, A. Halabica, R. Haglund and A. Leitenstorfer, *Phys. Rev. Lett.*, 2007, **99**, 116401.

21 R. M. Wentzcovitch, W. W. Schulz and P. B. Allen, *Phys. Rev. Lett.*, 1994, **72**, 3389–3392.

22 J. M. Booth and P. S. Casey, *ACS Appl. Mater. Interfaces*, 2009, **1**, 1899–905.

23 L. Whittaker, T.-L. Wu, C. J. Patridge, G. Sambandamurthy and S. Banerjee, *J. Mater. Chem.*, 2011, **21**, 5580.

24 S. Zhang, J. Y. Chou and L. J. Lauhon, *Nano Lett.*, 2009, **9**, 4527–32.

25 I. Karakurt, J. Boneberg, P. Leiderer, R. Lopez, A. Halabica and R. F. Haglund, *Appl. Phys. Lett.*, 2007, **91**, 091907.

26 S. S. Kanu and R. Binions, *Proc. R. Soc. A Math. Phys. Eng. Sci.*, 2010, **466**, 19–44.

27 C. Granqvist, *Thin Solid Films*, 1990, **193-194**, 730–741.

28 T. D. Manning, I. P. Parkin, M. E. Pemble, D. Sheel and D. Vernardou, *Chem.*

Mater., 2004, **16**, 744–749.

29 I. P. Parkin and T. D. Manning, *J. Chem. Educ.*, 2006, **83**, 393–400.

30 P. Baum, D.-S. Yang and A. H. Zewail, *Science (80-.).*, 2007, **318**, 788–792.

31 N. A. Charipar, H. Kim, E. Breckenfeld, K. M. Charipar, S. A. Mathews and A. Pique, *Appl. Phys. A Mater. Sci. Process.*, 2016, **122**.

32 X. Chen, Q. Lv and X. Yi, *Opt. - Int. J. Light Electron Opt.*, 2012, **123**, 1187–1189.

33 S. Y. Li, G. A. Niklasson and C. G. Granqvist, *J. Appl. Phys.*, 2010, **108**, 1–9.

34 J. Barber and P. D. Tran, *J. R. Soc. Interface*, 2013, **10**, 20120984–20120984.

35 P. V. Kamat, *J. Phys. Chem. C*, 2008, **112**, 18737–18753.

36 M. Gratzel, *Nature*, 2001, **414**, 338–344.

37 D. G. Nocera, *Acc. Chem. Res.*, 2012, **45**, 767–76.

38 A. J. Nozik, *Ann. Rev. Phys. Chem.*, 1978, **29**, 189–222.

39 R. S. Selinsky, Q. Ding, M. S. Faber, J. C. Wright and S. Jin, *Chem. Soc. Rev.*, 2013, **42**, 2963–85.

40 M. C. Scharber, D. Mühlbacher, M. Koppe, P. Denk, C. Waldauf, A. J. Heeger and C. J. Brabec, *Adv. Mater.*, 2006, **18**, 789–794.

41 M. W. Kanan, Y. Surendranath and D. G. Nocera, *Chem. Soc. Rev.*, 2009, **38**, 109–14.

42 D. Gust, T. A. Moore and A. L. Moore, *Faraday Discuss.*, 2012, **155**, 9.

43 J. Sun, D. K. Zhong and D. R. Gamelin, *Energy Environ. Sci.*, 2010, **3**, 1252.

44 N. S. Lewis and D. G. Nocera, *Proc. Natl. Acad. Sci. U. S. A.*, 2006, **103**, 15729–

35.

45 A. J. Bard and M. A. Fox, *Acc Chem Res*, 1995, **28**, 141–145.

46 K. E. Pelcher, C. C. Milleville, L. Wangoh, S. Chauhan, M. R. Crawley, P. M. Marley, L. F. J. Piper, D. F. Watson and S. Banerjee, *Chem. Mater.*, 2015, **27**, 2468–2479.

47 C. C. Milleville, K. E. Pelcher, M. Y. Sfeir, S. Banerjee and D. F. Watson, *J. Phys. Chem. C*, 2016, **120**, 5221–5232.

48 P. M. Marley, A. A. Stabile, C. P. Kwan, S. Singh, P. Zhang, G. Sambandamurthy and S. Banerjee, *Adv. Funct. Mater.*, 2013, **23**, 153–160.

49 L. Wangoh, P. M. Marley, N. F. Quackenbush, S. Sallis, D. A. Fischer, J. C. Woicik, S. Banerjee and L. F. J. Piper, *Appl. Phys. Lett.*, 2014, **104**, 182108.

50 P. M. Marley and S. Banerjee, *Inorg. Chem.*, 2012, **51**, 5264–9.

51 T. Yamauchi, M. Isobe and Y. Ueda, *Solid State Sci.*, 2005, **7**, 874–881.

52 T. Yamauchi, H. Ueda, Y. Ueda and J. Kikuchi, *Phys. C Supercond.*, 2007, **460-462**, 532–533.

53 T. Yamauchi and Y. Ueda, *Phys. Rev. B*, 2008, **77**, 104529.

54 C. J. Patridge, T.-L. Wu, G. Sambandamurthy and S. Banerjee, *Chem. Commun.*, 2011, **47**, 4484–6.

55 A. D. Wadsley, *Acta Crystallogr.*, 1955, **8**, 695–701.

56 R. L. Withers, P. Millet and Y. Tabira, *Zeitschrift für Krist.*, 2000, **215**, 357–363.

57 N. A. Chernova, M. Roppolo, A. C. Dillon and M. S. Whittingham, *J. Mater. Chem.*, 2009, **19**, 2526.

58 C. Ma, H. X. Yang, Z. A. Li, Y. Ueda and J. Q. Li, *Solid State Commun.*, 2008, **146**, 30–34.

59 T.-L. Wu, A. A. Stabile, C. J. Patridge, S. Banerjee and G. Sambandamurthy, *Appl. Phys. Lett.*, 2012, **101**, 163502.

60 P. M. Marley, S. Singh, T. A. Abtew, C. Jaye, D. A. Fischer, Z. Peihong, G. Sambandamurthy and S. Banerjee, *J. Phys. Chem. C*, 2014, **118**, 21235–21243.

61 O. Mentre, M. Huve and F. Abraham, *J. Solid State Chem.*, 1999, **145**, 186–196.

62 J. Yamaura, T. Yamauchi, E. Ninomiya, H. Sawa, M. Isobe, H. Yamada and Y. Ueda, *J. Magn. Magn. Mater.*, 2004, **272-276**, 438–439.

63 P. Nagpal and V. I. Klimov, *Nat. Commun.*, 2011, **2**, 486.

64 F. Alharbi, J. D. Bass, A. Salhi, A. Alyamani, H.-C. Kim and R. D. Miller, *Renew. Energy*, 2011, **36**, 2753–2758.

65 J. S. Baker, J. S. Nevins, K. M. Coughlin, L. A. Colon and D. F. Watson, *Chem. Mater.*, 2011, **23**, 3546–3555.

66 V. Chikan, *J. Phys. Chem. Lett.*, 2011, **2**, 2783–2789.

67 I. L. Medintz, H. T. Uyeda, E. R. Goldman and H. Mattoussi, *Nat. Mater.*, 2005, **4**, 435–46.

68 A. J. Nozik, *Phys. E Low-dimensional Syst. Nanostructures*, 2002, **14**, 115–120.

69 T. Trindade, P. O'Brien and N. L. Pickett, *Chem. Mater.*, 2001, **13**, 3843–3858.

70 M. B. Wilker, K. J. Schnitzenbaumer and G. Dukovic, *Isr. J. Chem.*, 2012, **52**, 1002–1015.

71 M. W. Kanan and D. G. Nocera, *Science (80-.).*, 2008, **321**, 1072–1075.

72 R. Ortega-Borges and D. Lincot, *J. Electrochem. Soc.*, 1993, **140**, 3464–3473.

73 M. Ristov, G. Sinadinovski and I. Grozdanov, *Thin Solid Films*, 1985, **123**, 63–67.

74 P. K. Nair, M. T. S. Nair, V. M. Garcı, O. L. Arenas, Y. Pen, J. Campos, H. Hu, R. Sua and M. E. Rinco, *Sol. Energy Mater. Sol. Cells*, 1998, **52**, 313–344.

75 M. Zirak, O. Moradlou, M. R. Bayati, Y. T. Nien and A. Z. Moshfegh, *Appl. Surf. Sci.*, 2013, **273**, 391–398.

76 J. Wei, H. Ji, W. Guo, A. H. Nevidomskyy and D. Natelson, *Nat. Nanotechnol.*, 2012, **7**, 357–362.

77 L. Whittaker, J. M. Velazquez and S. Banerjee, *CrystEngComm*, 2011, **13**, 5328.

78 T.-L. Wu, L. Whittaker, S. Banerjee and G. Sambandamurthy, *Phys. Rev. B*, 2011, **83**, 1–4.

79 L. Whittaker, C. Jaye, Z. Fu, D. A. Fischer and S. Banerjee, *J. Am. Chem. Soc.*, 2009, **131**, 8884–94.

80 I. A. M. Ibrahim, A. A. F. Zikry and M. A. Sharaf, *J. Am. Sci.*, 2010, **6**, 985–989.

81 J. Song, S. Wu and Y. Zhao, *Mater. Res. Bull.*, 2013, **48**, 1530–1535.

82 W. Stober, A. Fink and E. Bohn, *J. Colloid Interface Sci.*, 1968, **69**, 62–69.

83 J. Cheng, X. Ni, H. Zheng, B. Li, X. Zhang and D. Zhang, *Mater. Res. Bull.*, 2006, **41**, 1424–1429.

84 A. Jaroenworaluck, W. Sunsaneeyametha, N. Kosachan and R. Stevens, *Surf. Interface Anal.*, 2006, **38**, 473–477.

85 Y. Zhang, P. Rao, M. Lü, D. Zeng and J. Wu, *J. Am. Ceram. Soc.*, 2009, **92**,

1877–1880.

86 Y. Wang, Z. Tang, X. Liang, L. M. Liz-Marzán and N. A. Kotov, *Nano Lett.*, 2004, **4**, 225–231.

87 L. Cong, M. Takeda, Y. Hamanaka, K. Gonda, M. Watanabe, M. Kumasaka, Y. Kobayashi, M. Kobayashi and N. Ohuchi, *PLoS One*, 2010, **5**, e13167.

88 C. Hui, C. Shen, J. Tian, L. Bao, H. Ding, C. Li, Y. Tian, X. Shi and H.-J. Gao, *Nanoscale*, 2011, **3**, 701–5.

89 J. Wang, T. Tsuzuki, L. Sun and X. Wang, *J. Am. Ceram. Soc.*, 2009, **92**, 2083–2088.

90 L. Whittaker, T. Wu, A. Stabile, G. Sambandamurthy and S. Banerjee, *ACS Nano*, 2011, **5**, 8861–8867.

91 A. C. Jones, S. Berweger, J. Wei, D. Cobden and M. B. Raschke, *Nano Lett.*, 2010, **10**, 1574–81.

92 A. Alessi, S. Agnello, G. Buscarino and F. M. Gelardi, *J. Non. Cryst. Solids*, 2013, **362**, 20–24.

93 C. N. Berglund and H. J. Guggenheim, *Phys. Rev.*, 1969, **185**, 1022–1033.

94 J. I. Sohn, H. J. Joo, K. S. Kim, H. W. Yang, A.-R. Jang, D. Ahn, H. H. Lee, S. Cha, D. J. Kang, J. M. Kim and M. EWelland, *Nanotechnology*, 2012, **23**, 205707.

95 United Nation Environment Programme, *Buildings and Climate Change: Status, Challenges and Opportunities*, 2007.

96 U.S. Department of Energy, *Energy Efficiency Trends in Residential and*

Commercial Buildings, 2008.

97 American Council for an Energy-Efficient Economy, *Cooling Systems*, 2015.

98 C. G. Granqvist, *Nat. Mater.*, 2006, **5**, 89–90.

99 A. Shehabi, N. DeForest, A. McNeil, E. Masanet, J. Greenblatt, E. S. Lee, G. Masson, B. A. Helms and D. J. Milliron, *Energy Build.*, 2013, **66**, 415–423.

100 A. Llordés, G. Garcia, J. Gazquez and D. J. Milliron, *Nature*, 2013, **500**, 323–326.

101 V. Costanzo, G. Evola and L. Marletta, *Sol. Energy Mater. Sol. Cells*, 2016, **149**, 110–120.

102 S. K. Deb, *Proc. R. Soc. A Math. Phys. Eng. Sci.*, 1968, **304**, 211–231.

103 P. Monceau, *Adv. Phys.*, 2012, **61**, 325–581.

104 P. Edwards, V. Kuznetsov, D. Slocombe and R. Vijayaraghavan, in *Comprehensive Inorganic Chemistry II*, eds. J. Reedijk and K. Poeppelmeier, Elsevier, Oxford, Second Edi., 2013, vol. 4, pp. 153–176.

105 P. P. Edwards and M. J. Sienko, *Phys. Rev. B Solid State*, 1978, **17**, 2575–81.

106 P. P. Edwards, T. V Ramakrishnan and C. N. R. Rao, *J. Phys. Chem.*, 1995, **99**, 5228–5239.

107 D. Adler, *Rev. Mod. Phys.*, 1968, **40**, 714–736.

108 C. Batista, R. M. Ribeiro and V. Teixeira, *Nanoscale Res. Lett.*, 2011, **6**, 301.

109 P. Zhang, M. Li, Q. Deng, J. Zhang, J. Wu, Z. Hu and J. Chu, *Phys. Chem. Chem. Phys.*, 2016, **18**, 6239–6246.

110 D. Louloudakis, D. Vernardou, E. Spanakis, N. Katsarakis and E. Koudoumas, *Phys. Procedia*, 2013, **46**, 137–141.

111 J. Zhou, Y. Gao, Z. Zhang, H. Luo, C. Cao, Z. Chen, L. Dai and X. Liu, *Sci. Rep.*, 2013, **3**, 3029.

112 G. A. Horrocks, S. Singh, M. F. Likely, G. Sambandamurthy and S. Banerjee, *ACS Appl. Mater. Interfaces*, 2014, **6**, 15726–15732.

113 K. E. Pelcher, M. R. Crawley and S. Banerjee, *Mater. Res. Express*, 2014, **1**, 035014.

114 X. Xiao, H. Zhang, G. Chai, Y. Sun, T. Yang, H. Cheng, L. Chen, L. Miao and G. Xu, *Mater. Res. Bull.*, 2014, **51**, 6–12.

115 F. Yue, W. Huang, Q. Shi, D. Li, Y. Hu, Y. Xiao, X. Deng and C. Wang, *J. Sol-Gel Sci. Technol.*, 2014, **72**, 565–570.

116 W. Li, S. Ji, K. Qian and P. Jin, *Ceram. Int.*, 2015, **41**, 5049–5056.

117 J. Zhu, Y. Zhou, B. Wang, J. Zheng, S. Ji, H. Yao, H. Luo and P. Jin, *ACS Appl. Mater. Interfaces*, 2015, **7**, 27796–27803.

118 M. M. Qazilbash, M. Brehm, B.-G. Chae, P.-C. Ho, G. O. Andreev, B.-J. Kim, S. J. Yun, A. V Balatsky, M. B. Maple, F. Keilmann, H.-T. Kim and D. N. Basov, *Science (80-.).*, 2007, **318**, 1750–1753.

119 W. M. Haynes, Ed., in *CRC Handbook of Chemistry and Physics*, Taylor & Francis Group, Boca Raton, FL, 91st edn., 2011, pp. 1–523.

120 Rohm and Haas, *Acrysol™ ASE-60 Alkali-Soluble Anionic Thickener*, 2003.

121 R. E. Bird, R. L. Hulstrom and L. J. Lewis, *Sol. Energy*, 1983, **30**, 563–573.

122 B. J. Schultz, R. V. Dennis, V. Lee and S. Banerjee, *Nanoscale*, 2014, **6**, 3444–66.

123 I. Hod and A. Zaban, *Langmuir*, 2014, **30**, 7264–73.

124 S. W. Cho, L. F. J. Piper, A. DeMasi, A. R. H. Preston, K. E. Smith, K. V Chauhan, P. Sullivan, R. A. Hatton and T. S. Jones, *J. Phys. Chem. C*, 2010, **114**, 1928–1933.

125 G. M. Dalpian and J. R. Chelikowsky, *Phys. Rev. Lett.*, 2006, **96**, 226802.

126 V. Eyert and K.-H. Höck, *Phys. Rev. B*, 1998, **57**, 12727–12737.

127 A. Suli, M. I. Torok and I. Hevesi, *Thin Solid Films*, 1986, **139**, 233–246.

128 Y. Wang, Y. R. Su, L. Qiao, L. X. Liu, Q. Su, C. Q. Zhu and X. Q. Liu, *Nanotechnology*, 2011, **22**, 225702.

129 A. Hagfeldt and M. Gratzel, *Chem. Rev.*, 1995, **95**, 49–68.

130 L. Li, L. Duan, F. Wen, C. Li, M. Wang, A. Hagfeldt and L. Sun, *Chem. Commun.*, 2012, 48, 988.

131 A. Nattestad, A. J. Mozer, M. K. R. Fischer, Y. Cheng, A. Mishra, P. Bäuerle and U. Bach, *Nat. Mater.*, 2009, **9**, 31–35.

132 P. V. Kamat, *J. Phys. Chem. Lett.*, 2013, **4**, 908–918.

133 L. E. Brus, *J. Chem. Phys.*, 1984, **80**, 4403–4409.

134 K. P. Acharya, E. Khon, T. O. Conner, I. Nemitz, A. Klinkova, R. S. Khnayzer, P. Anzenbacher and M. Zamkov, *ACS Nano*, 2011, **5**, 4953–4964.

135 S. B. Block, L. A. Yurs, A. V. Pakoulev, R. S. Selinsky, S. Jin and J. C. Wright, *J. Phys. Chem. Lett.*, 2012, **3**, 2707–2712.

136 I. Robel, V. Subramanian, M. Kuno and P. V Kamat, *J. Am. Chem. Soc.*, 2006, **128**, 2385–2393.

137 Y.-J. Shen and Y.-L. Lee, *Nanotechnology*, 2008, **19**, 045602.

138 D. F. Watson, *J. Phys. Chem. Lett.*, 2010, **1**, 2299–2309.

139 H. Zhang, K. Cheng, Y. M. Hou, Z. Fang, Z. X. Pan, W. J. Wu, J. L. Hua and X. H. Zhong, *Chem. Commun.*, 2012, **48**, 11235.

140 Z. Pan, I. Mora-Seró, Q. Shen, H. Zhang, Y. Li, K. Zhao, J. Wang, X. Zhong and J. Bisquert, *J. Am. Chem. Soc.*, 2014, **136**, 9203–9210.

141 R. Vogel, P. Hoyer and H. Weller, *J. Phys. Chem.*, 1994, **98**, 3183–3188.

142 H. J. Lee, P. Chen, S.-J. Moon, F. Sauvage, K. Sivula, T. Bessho, D. R. Gamelin, P. Comte, S. M. Zakeeruddin, S. Il Seok, M. Grätzel and M. K. Nazeeruddin, *Langmuir*, 2009, **25**, 7602–8.

143 H. M. Pathan and C. D. Lokhande, *Bull. Mater. Sci.*, 2004, **27**, 85–111.

144 G. A. Horrocks, M. F. Likely, J. M. Velazquez and S. Banerjee, *J. Mater. Chem. A*, 2013, **1**, 15265.

145 Y.-S. Park, A. Dmytruk, I. Dmitruk, N. Yasuto, A. Kasuya, M. Takeda and N. Ohuchi, *J. Nanosci. Nanotechnol.*, 2007, **7**, 3750–3753.

146 Y.-S. Park, A. Dmytruk, I. Dmitruk, A. Kasuya, M. Takeda, N. Ohuchi, Y. Okamoto, N. Kaji, M. Tokeshi and Y. Baba, *ACS Nano*, 2010, **4**, 121–128.

147 J. S. Nevins, K. M. Coughlin and D. F. Watson, *ACS Appl. Mater. Interfaces*, 2011, **3**, 4242–4253.

148 H. J. Lee, J. Bang, J. Park, S. Kim and S.-M. Park, *Chem. Mater.*, 2010, **22**, 5636–5643.

149 G. Conti, A. M. Kaiser, A. X. Gray, S. Nemšák, G. K. Pálsson, J. Son, P. Moetakef, A. Janotti, L. Bjaalie, C. S. Conlon, D. Eiteneer, A. A. Greer, A. Keqi,

A. Rattanachata, A. Y. Saw, A. Bostwick, W. C. Stolte, A. Gloskovskii, W. Drube, S. Ueda, M. Kobata, K. Kobayashi, C. G. Van de Walle, S. Stemmer, C. M. Schneider and C. S. Fadley, *J. Appl. Phys.*, 2013, **113**, 143704.

150 K. M. Coughlin, J. S. Nevins and D. F. Watson, *ACS Appl. Mater. Interfaces*, 2013, **5**, 8649–8654.

151 C. B. Murray, D. J. Norris and M. G. Bawendi, *J. Am. Chem. Soc.*, 1993, **115**, 8706–8715.

152 W. W. Yu, L. Qu, W. Guo and X. Peng, *Chem. Mater.*, 2003, **15**, 2854–2860.

153 W. M. Haynes, Ed., *CRC Handbook of Chemistry and Physics*, CRC Press, Boca Raton, FL, 94th edn., 2013.

154 J. P. Koo, Y.-K. Kim and J. S. Ha, *Appl. Surf. Sci.*, 2006, **253**, 1528–1533.

155 Y.-K. Kim, S. J. Park, J. P. Koo, G. T. Kim, S. Hong and J. S. Ha, *Nanotechnology*, 2007, **18**, 015304.

156 S. Myung, K. Heo, M. Lee, Y.-H. Choi, S.-H. Hong and S. Hong, *Nanotechnology*, 2007, **18**, 205304.

157 Z. V. Popovi, M. J. Konstantinovi, V. V. Moshchalkov, M. Isobe and Y. Ueda, *J. Phys. Condens. Matter*, 2003, **15**, L139–L145.

158 A. P. Alivistatos, T. D. Harris, P. J. Carroll, M. L. Steigerwald and L. E. Brus, *J. Chem. Phys.*, 1989, **90**, 3463–3468.

159 S. Banerjee, S. Jia, D. I. Kim, R. D. Robinson, J. W. Kysar, J. Bevk and I. P. Herman, *Nano Lett.*, 2006, **6**, 175–80.

160 R. S. Dibbell and D. F. Watson, *J. Phys. Chem. C*, 2009, **113**, 3139–3149.

161 R. S. Dibbell, D. G. Youker and D. F. Watson, *J. Phys. Chem. C*, 2009, **25**, 18643–18651.

162 I. Robel, M. Kuno and P. V. Kamat, *J. Am. Chem. Soc.*, 2007, **129**, 4136–4137.

163 B.-R. Hyun, Y.-W. Zhong, A. C. Bartnik, L. Sun, H. D. Abruña, F. W. Wise, J. D. Goodreau, J. R. Matthews, T. M. Leslie and N. F. Borrelli, *ACS Nano*, 2008, **2**, 2206–2212.

164 M. J. Bowers II, J. R. McBride and S. J. Rosenthal, *J. Am. Chem. Soc.*, 2005, **127**, 15378–15379.

165 D. R. Baker and P. V. Kamat, *Langmuir*, 2010, **26**, 11272–11276.

166 J. J. Ramsden and M. Gratzel, *J. Chem. Soc. Faraday Trans. 1*, 1984, **80**, 919.

167 C. F. Landes, M. Braun and M. A. El-Sayed, *J. Phys. Chem. B*, 2001, **105**, 10554–10558.

168 N. A. Hill and K. B. Whaley, *J. Chem. Phys.*, 1994, **100**, 2831–2837.

169 N. Chestnoy, T. D. Harris, R. Hull and L. E. Brus, *J. Phys. Chem.*, 1986, **90**, 3393–3399.

170 M. O'Neil, J. Marohn and G. McLendon, *J. Phys. Chem.*, 1990, **94**, 4356–4363.

171 J. R. Lakowicz, I. Gryczynski, Z. Gryczynski and C. J. Murphy, *J. Phys. Chem. B*, 1999, **103**, 7613–7620.

172 J. Z. Zhang, *J. Phys. Chem. B*, 2000, **104**, 7239–7253.

173 K. Tvrdy, P. A. Frantsuzov and P. V. Kamat, *Proc. Natl. Acad. Sci.*, 2011, **108**, 29–34.

174 Z. Wang, A. Shakya, J. Gu, S. Lian and S. Maldonado, *J. Am. Chem. Soc.*, 2013,

135, 9275–9278.

175 K. Zheng, K. Žídek, M. Abdellah, W. Zhang, P. Chábera, N. Lenngren, A. Yartsev and T. Pullerits, *J. Phys. Chem. C*, 2014, **118**, 18462–18471.

176 O. E. Semonin, J. M. Luther and M. C. Beard, *Mater. Today*, 2012, **15**, 508–515.

177 V. L. Bridewell, R. Alam, C. J. Karwacki and P. V. Kamat, *Chem. Mater.*, 2015, **27**, 5064–5071.

178 P. V. Kamat, *Acc. Chem. Res.*, 2012, **45**, 1906–1915.

179 A. Pandey and P. Guyot-Sionnest, *Sci. (Washington, DC, U. S.)*, 2008, **322**, 929–932.

180 S. M. Goodman, V. Singh, J. C. Ribot, A. Chatterjee and P. Nagpal, *J. Phys. Chem. Lett.*, 2014, **5**, 3909–3913.

181 F. Hetsch, X. Xu, H. Wang, S. V. Kershaw and A. L. Rogach, *J. Phys. Chem. Lett.*, 2011, **2**, 1879–1887.

182 M. Ghorbani-Asl, A. N. Enyashin, A. Kuc, G. Seifert and T. Heine, *Phys. Rev. B*, 2013, **88**, 245440.

183 B. S. Pujari and D. G. Kanhere, *J. Phys. Chem. C*, 2009, **113**, 21063–21067.

184 M. C. Beard, J. M. Luther and A. J. Nozik, *Nat. Nanotechnol.*, 2014, **9**, 951–954.

185 I. Grigioni, K. G. Stamplecoskie, E. Selli and P. V Kamat, *J. Phys. Chem. C*, 2015, **119**, 20792–20800.

186 A. Luque, A. Martí and C. Stanley, *Nat. Photonics*, 2012, **6**, 146–152.

187 J. P. Kim, J. A. Christians, H. Choi, S. Krishnamurthy and P. V. Kamat, *J. Phys. Chem. Lett.*, 2014, **5**, 1103–1109.

188 P. M. Marley, T. A. Abtew, K. E. Farley, G. A. Horrocks, R. V. Dennis, P. Zhang and S. Banerjee, *Chem. Sci.*, 2015, **6**, 1712–1718.

189 H. J. Lee, M. Wang, P. Chen, D. R. Gamelin, S. M. Zakeeruddin, M. Gratzel and M. K. Nazeeruddin, *Nano Lett.*, 2009, **9**, 4221–4227.

190 O. Stenzel, *The Physics of Thin Film Optical Spectra: An Introduction*, Springer, Berlin, Germany, 2005.

191 A. A. Mane, V. V. Ganbavle, M. A. Gaikwad, S. S. Nikam, K. Y. Rajpure and A. V. Moholkar, *J. Anal. Appl. Pyrolysis*, 2015, **115**, 57–65.

192 E. Burstein, *Phys. Rev.*, 1954, **93**, 632–633.

193 B. O'Regan, M. Graetzel and D. Fitzmaurice, *J. Phys. Chem.*, 1991, **95**, 10525–10528.

194 B. O'Regan, M. Graetzel and D. Fitzmaurice, *Chem. Phys. Lett.*, 1991, **183**, 89–93.

195 G. Rothenberger, D. Fitzmaurice and M. Graetzel, *J. Phys. Chem.*, 1992, **96**, 5983–5986.

196 G. Redmond, D. Fitzmaurice and M. Graetzel, *J. Phys. Chem.*, 1993, **97**, 6951–6954.

197 A. Othonos, C. Christofides and M. Zervos, *Appl. Phys. Lett.*, 2013, **103**, 133112/1–133112/4.

198 D. Maganas, M. Roemelt, M. Haevecker, A. Trunschke, A. Knop-Gericke, R. Schloegl and F. Neese, *Phys. Chem. Chem. Phys.*, 2013, **15**, 7260–7276.

199 J. M. Velazquez, C. Jaye, D. A. Fischer and S. Banerjee, *J. Phys. Chem. C*, 2009,

113, 7639–7645.

200 M. G. Bawendi, W. L. Wilson, L. Rothberg, P. J. Carroll, T. M. Jedju, M. L. Steigerwald and L. E. Brus, *Phys. Rev. Lett.*, 1990, **65**, 1623–1626.

201 S. Logunov, T. Green, S. Marguet and M. A. El-Sayed, *J. Phys. Chem. A*, 1998, **102**, 5652–5658.

202 C. Burda, T. C. Green, S. Link and M. A. El-Sayed, *J. Phys. Chem. B*, 1999, **103**, 1783–1788.

203 J. G. Radich, N. R. Peeples, P. K. Santra and P. V. Kamat, *J. Phys. Chem. C*, 2014, **118**, 16463–16471.

204 X. Li, J. Yu, J. Low, Y. Fang, J. Xiao and X. Chen, *J. Mater. Chem. A*, 2015, **3**, 2485–2534.

205 F. E. Osterloh, *Chem. Soc. Rev.*, 2013, **42**, 2294–2320.

206 W. Li and X. Zhong, *J. Phys. Chem. Lett.*, 2015, **6**, 796–806.

207 J. Tian and G. Cao, *J. Phys. Chem. Lett.*, 2015, **6**, 1859–1869.

208 Y. Xu and M. A. A. Schoonen, *Am. Mineral.*, 2000, **85**, 543–556.

209 P. Y. Hung, T. E. O'Loughlin, A. Lewis, R. Dechter, M. Samavoa, S. Banerjee, E. L. Wood and A. Hight R. Hight, *SPIE Adv. Lithogr. Pages*, 2015, **9424**, 94241S–1 – 94241S–13 .

210 K. Han, W. Bin Im, J. Heo and W. J. Chung, *Chem. Commun. (Cambridge, U. K.)*, 2016, **52**, 3564–3567.

211 J. H. Scofield, *Report*, 1973, **UCRL-51326**, 376.

212 J. Wong, F. W. Lytle, R. P. Messmer and D. H. Maylotte, *Phys. Rev. B Condens.*

Matter, 1984, **30**, 5596–5610.

213 J. Jasieniak, M. Califano and S. E. Watkins, *ACS Nano*, 2011, **5**, 5888–5902.

214 J. R. I. Lee, R. W. Meulenberg, K. M. Hanif, H. Mattoussi, J. E. Klepeis, L. J. Terminello and T. Van Buuren, *Phys. Rev. Lett.*, 2007, **98**, 146803/1–146803/4.

APPENDIX A

SUPPLEMENTARY FIGURES AND TABLES

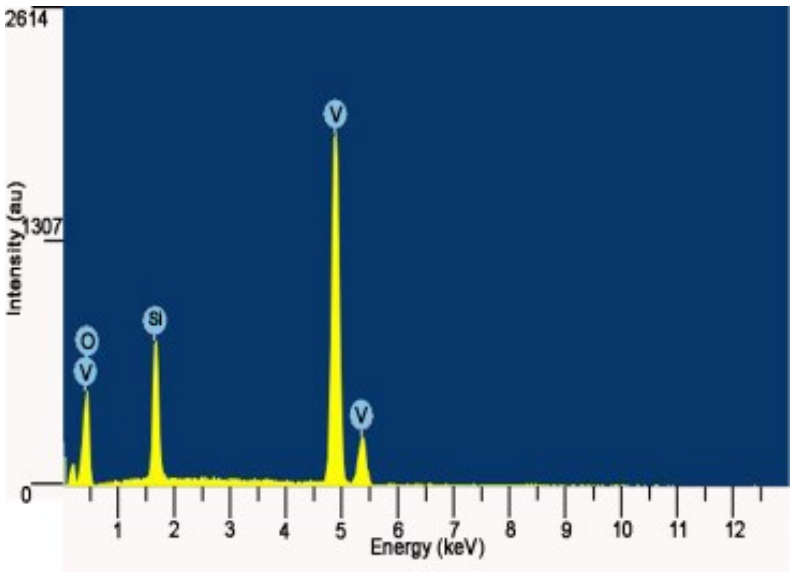

Figure A. 1 EDX spectrum of VO_2 nanowires reacted with TEOS solution for 30 min.

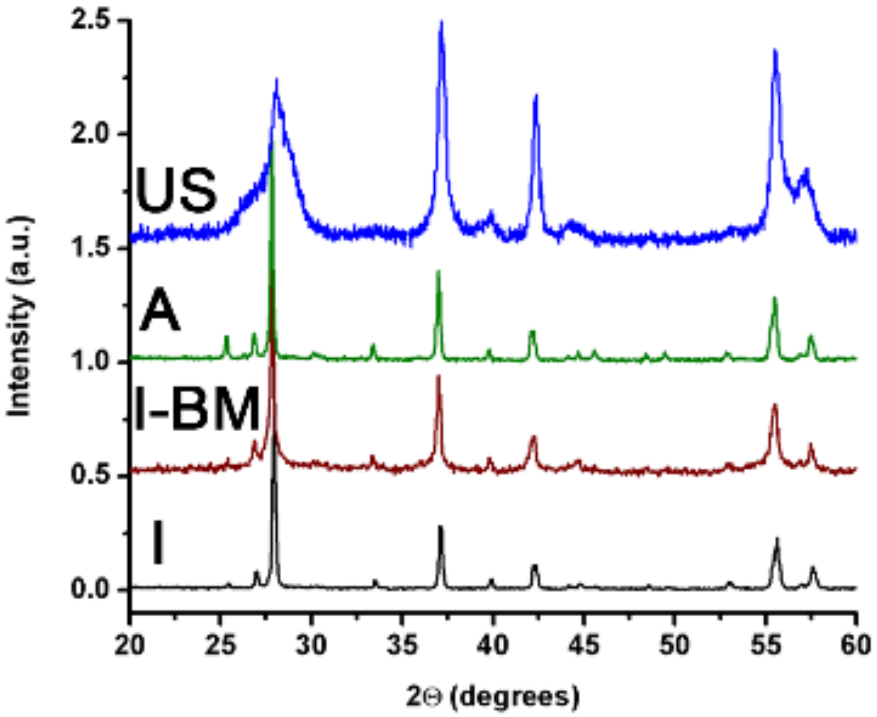

Figure A. 2 X-ray diffraction patterns of VO_2 nanocrystals.

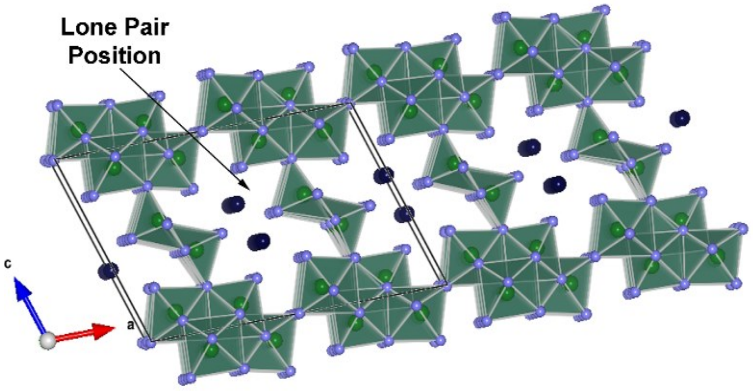

Figure A. 3 Crystal structure of β-$Pb_xV_2O_5$.

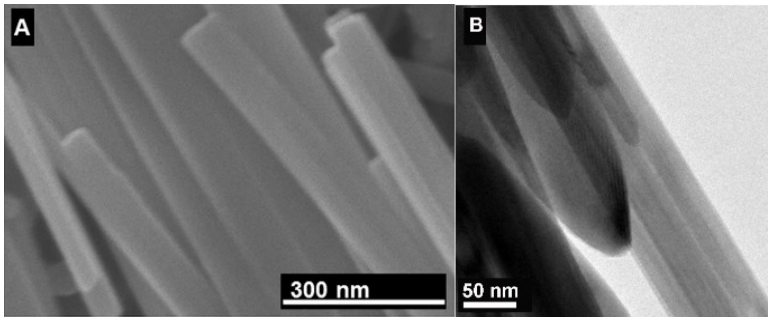

Figure A. 4 SEM image (A) and TEM image (B) of β-$Pb_xV_2O_5$ nanowires mixed with MP-CdSe QDs.

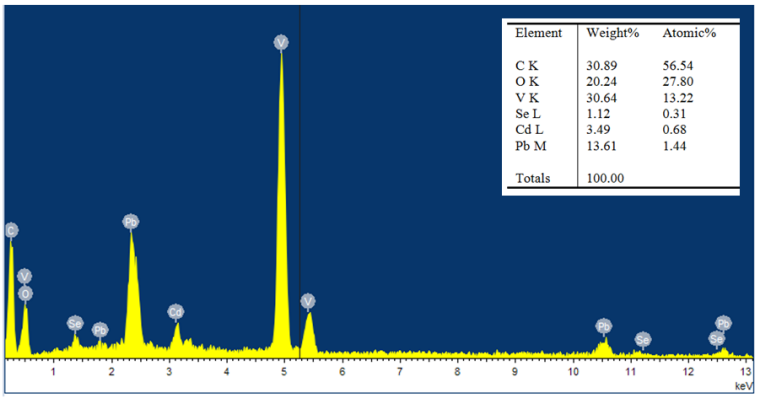

Figure A. 5 Representative EDS spectrum of β-$Pb_xV_2O_5$ nanowires mixed with Cys-CdSe QDs.

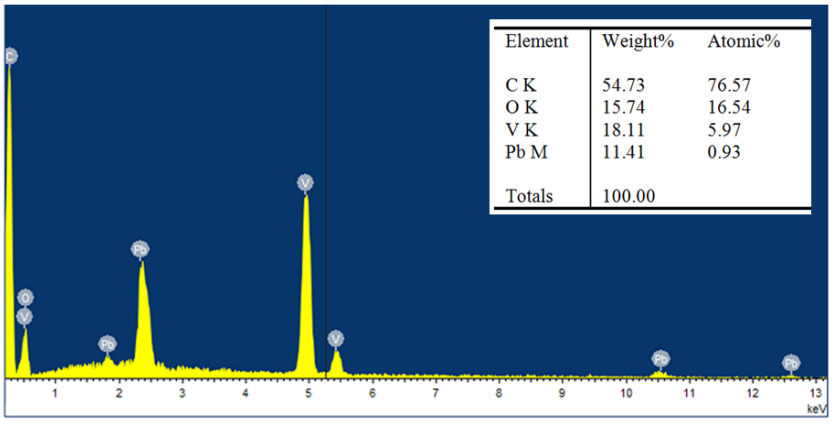

Figure A. 6 Representative EDS spectrum of β-$Pb_xV_2O_5$ nanowires mixed with MP-CdSe QDs.

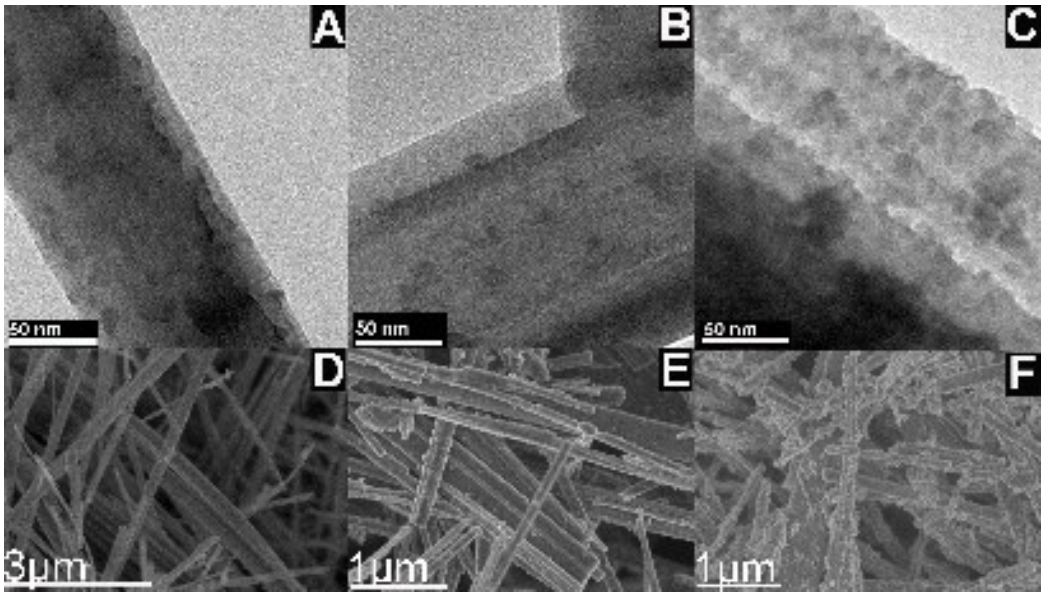

Figure A. 7 TEM (top) and SEM (bottom) images of β-$Pb_xV_2O_5$ nanowires treated *via* one SILAR cycle (A and D), two SILAR cycles (B and E), and four SILAR cycles (C and F).

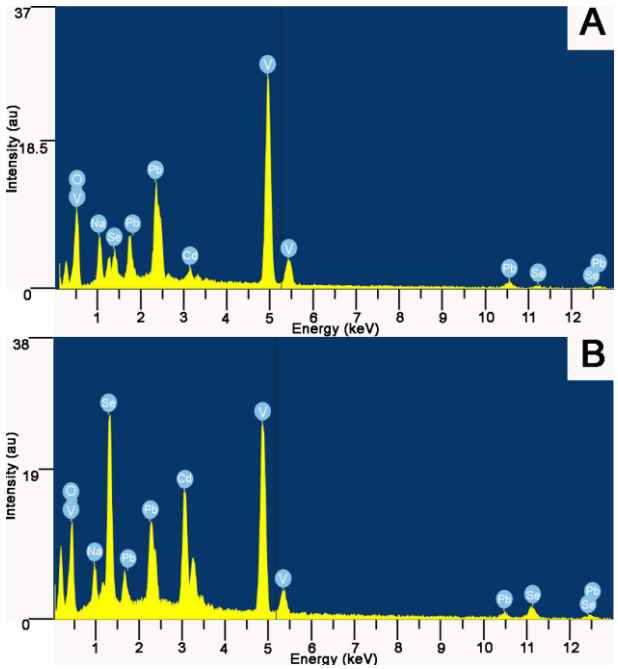

Figure A. 8 Representative ensemble EDS spectra for β-$Pb_xV_2O_5$ nanowires after A) one SILAR cycle and B) five SILAR cycles.

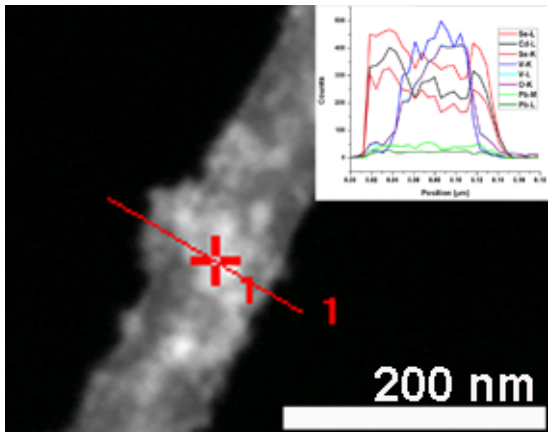

Figure A. 9 TEM image and corresponding EDS line scan acquired for β-$Pb_xV_2O_5$ nanowires coated with CdSe QDS *via* five SILAR cycles.

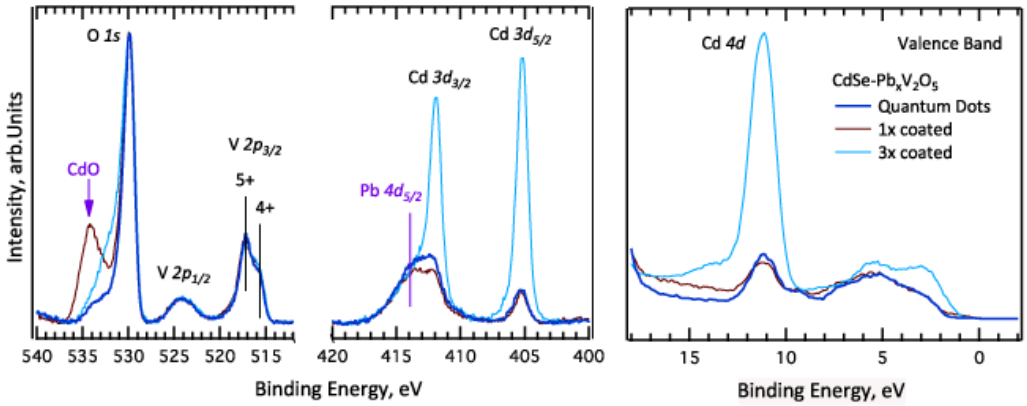

Figure A. 10 HAXPES spectra for β-$Pb_xV_2O_5$ nanowires functionalized with Cys-CdSe QDs displaying equivalent coverage and modification of the electronic structure as for one SILAR cycle.

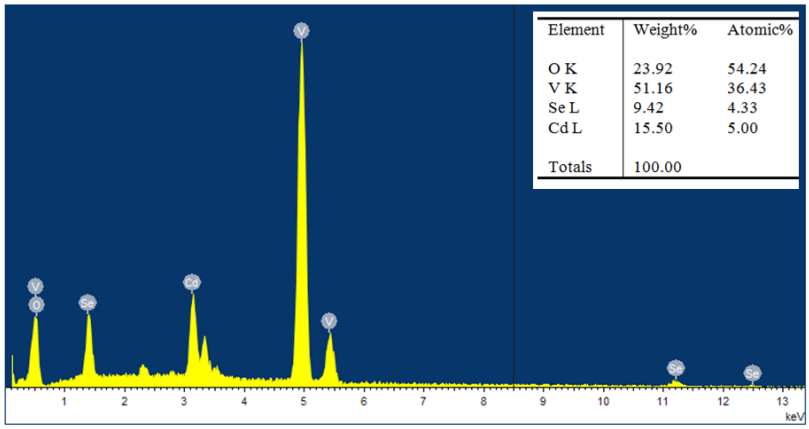

Figure A. 11 Representative EDS spectrum of V_2O_5 nanowires mixed with Cys-CdSe QDs.

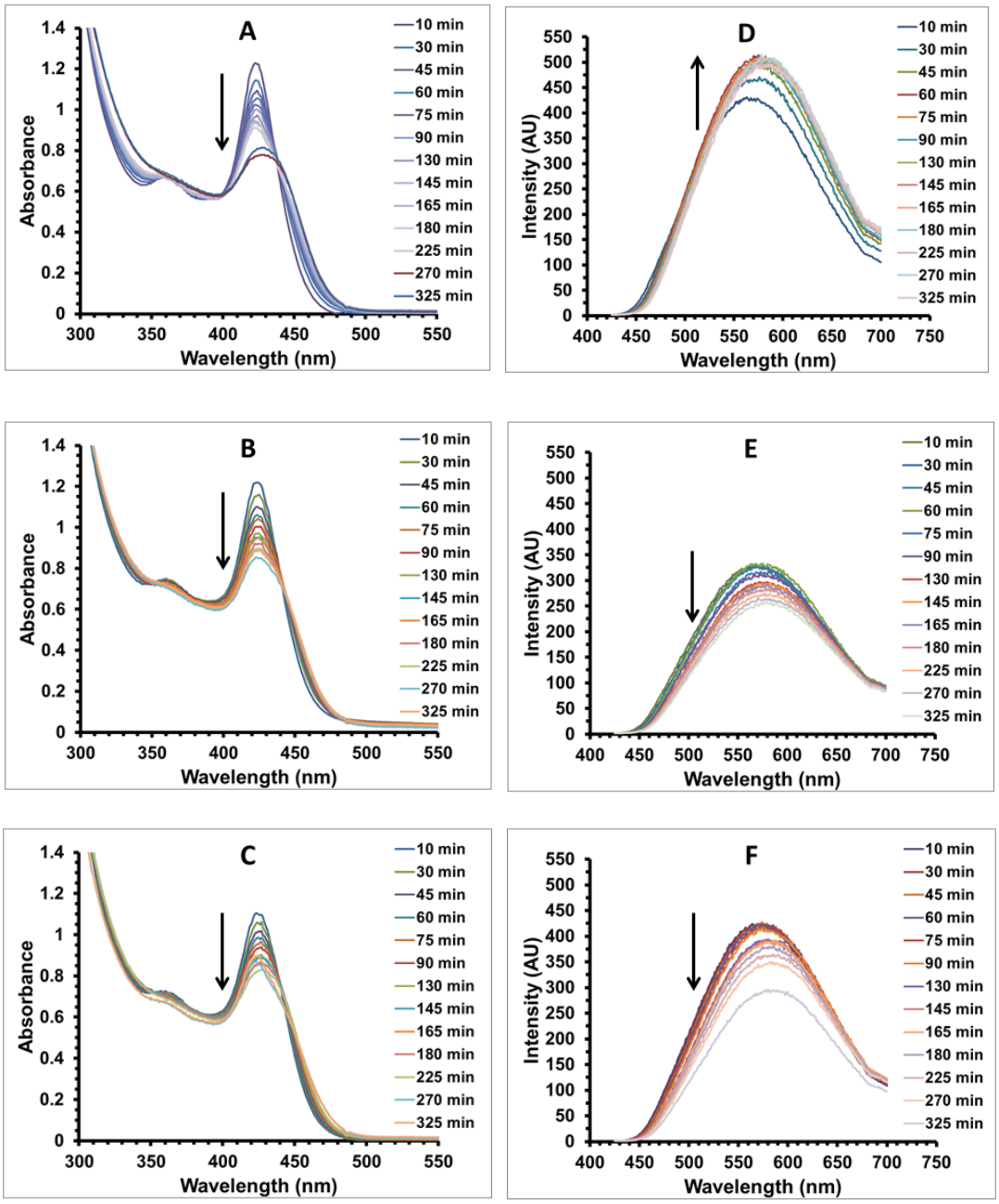

Figure A. 12 UV-Vis absorption (A, B, C) and steady-state emission (D, E, F) spectra of Cys-CdSe QDs as a function of elapsed time after sample preparation. The top spectra (A and D) correspond to free Cys-CdSe QDs with no nanowires added. The middle spectra (B and E) and bottom spectra (C and F) correspond to Cys-CdSe QDs mixed with β-$Pb_xV_2O_5$ and V_2O_5 nanowires, respectively.

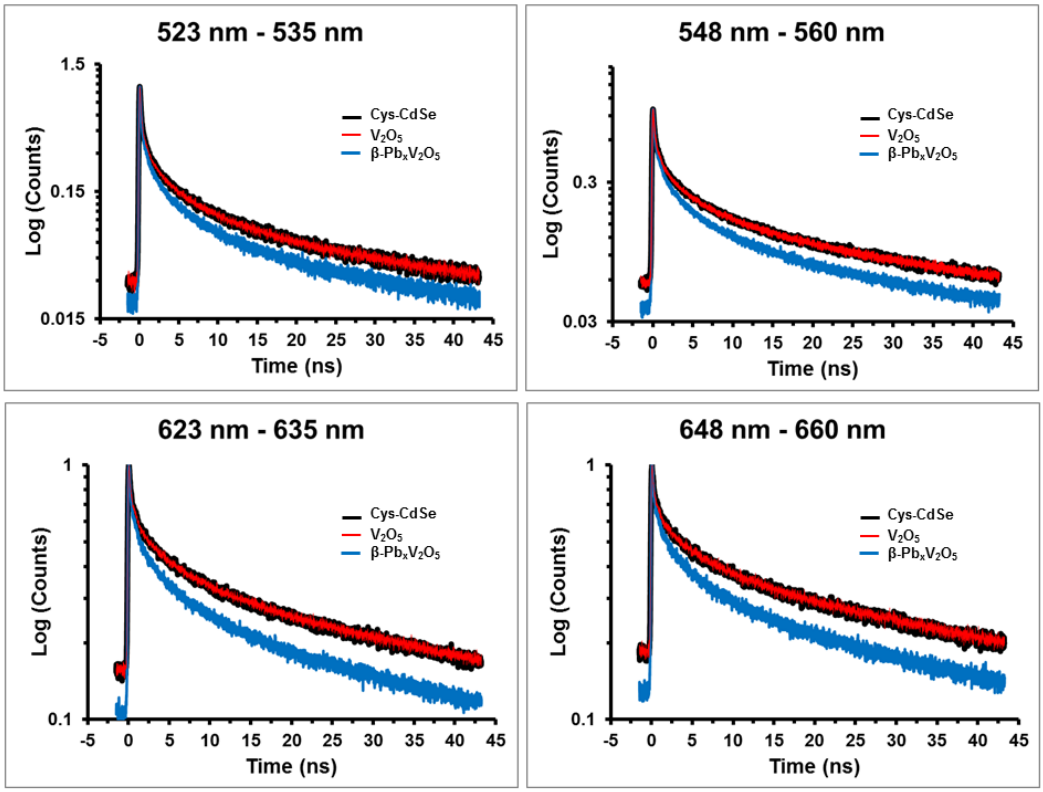

Figure A. 13 Representative time-resolved emission decay traces at various wavelengths within the steady-state emission band. All decay traces shown were acquired 75 min after samples were prepared.

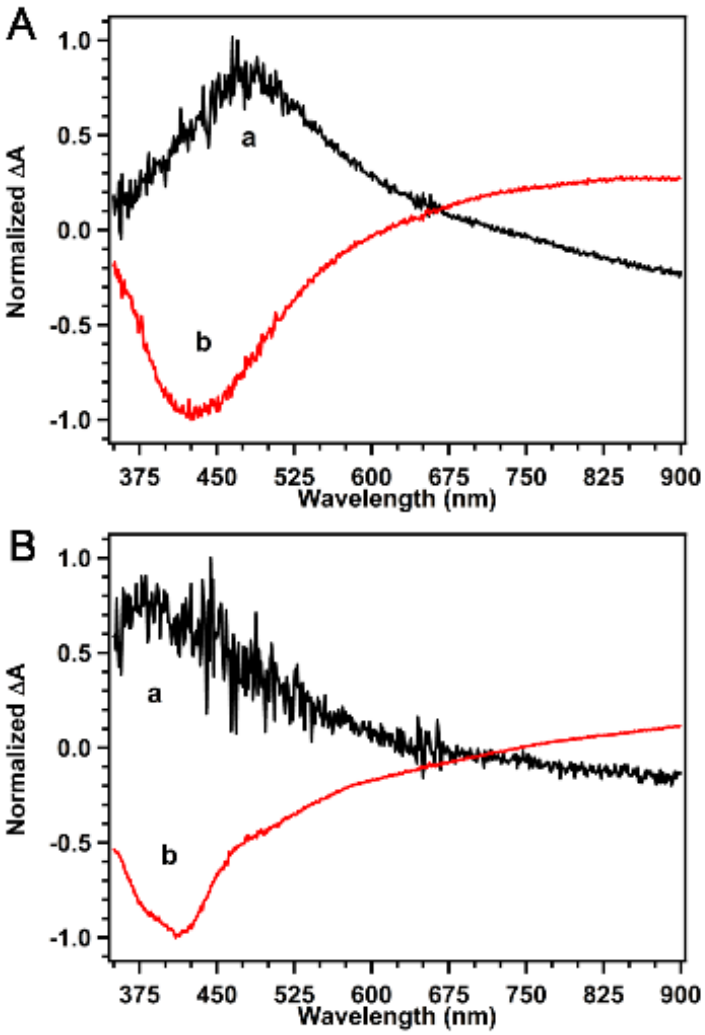

Figure A. 14 Spectroelectrochemical difference spectra for (A) β-$Pb_{0.33}V_2O_5$ and (B) V_2O_5 nanowire thin films. In each panel, (a) = oxidized – neutral and (b) = reduced – neutral.

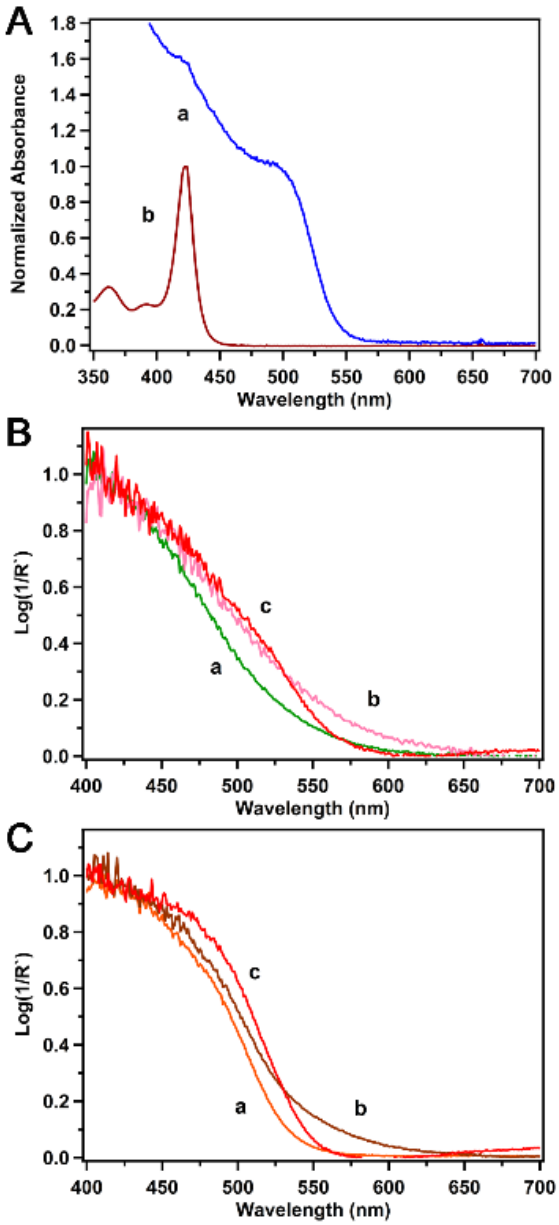

Figure A. 15 (A) Ground state absorption spectra of dispersed colloidal solutions of (a) Cys-CdSe (lg) and (b) Cys-CdSe (sm). (B) Diffuse reflectance absorption spectra of (a) β-$Pb_{0.33}V_2O_5$, (b) 3x SILAR CdSe/β-$Pb_{0.33}V_2O_5$, and(c) Cys-CdSe(lg)/β-$Pb_{0.33}V_2O_5$. (C) Diffuse reflectance absorption spectra of (a) V_2O_5, (b)5x SILAR CdSe/V_2O_5, and(c) Cys-CdSe(lg)/V_2O_5.

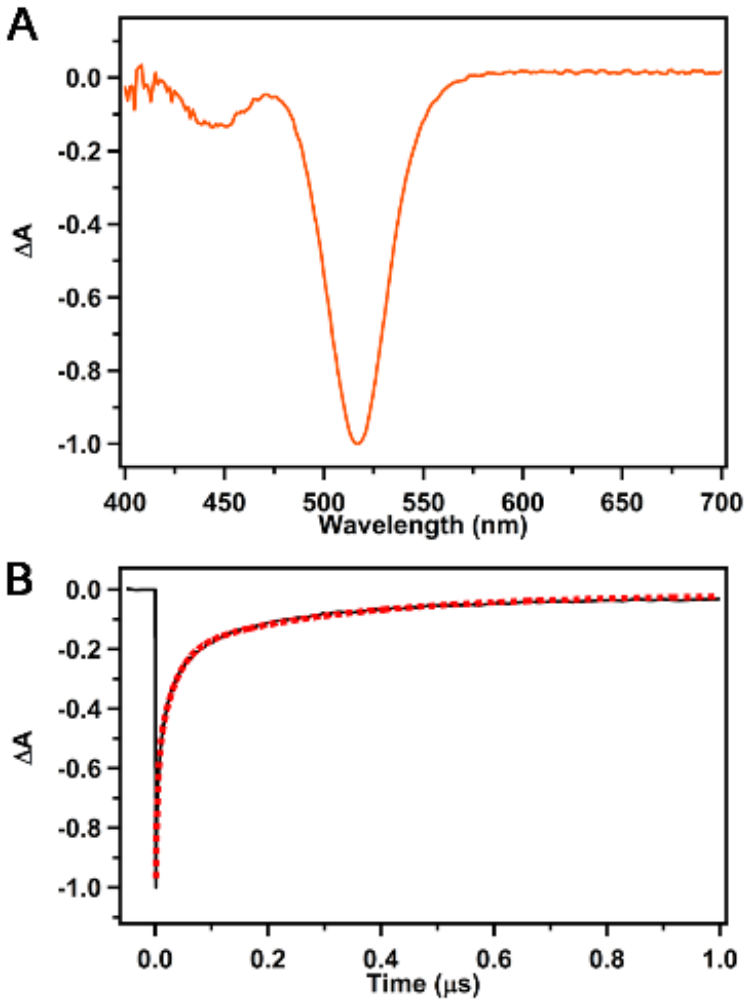

Figure A. 16 TA spectra (A) and kinetic decay/fit (B) of dispersed Cys-CdSe (lg), λ_{pump} = 425 nm. The decay profile is fitted to a triexponential decay with average lifetime of (5.9±0.2)x10^{-8}s.

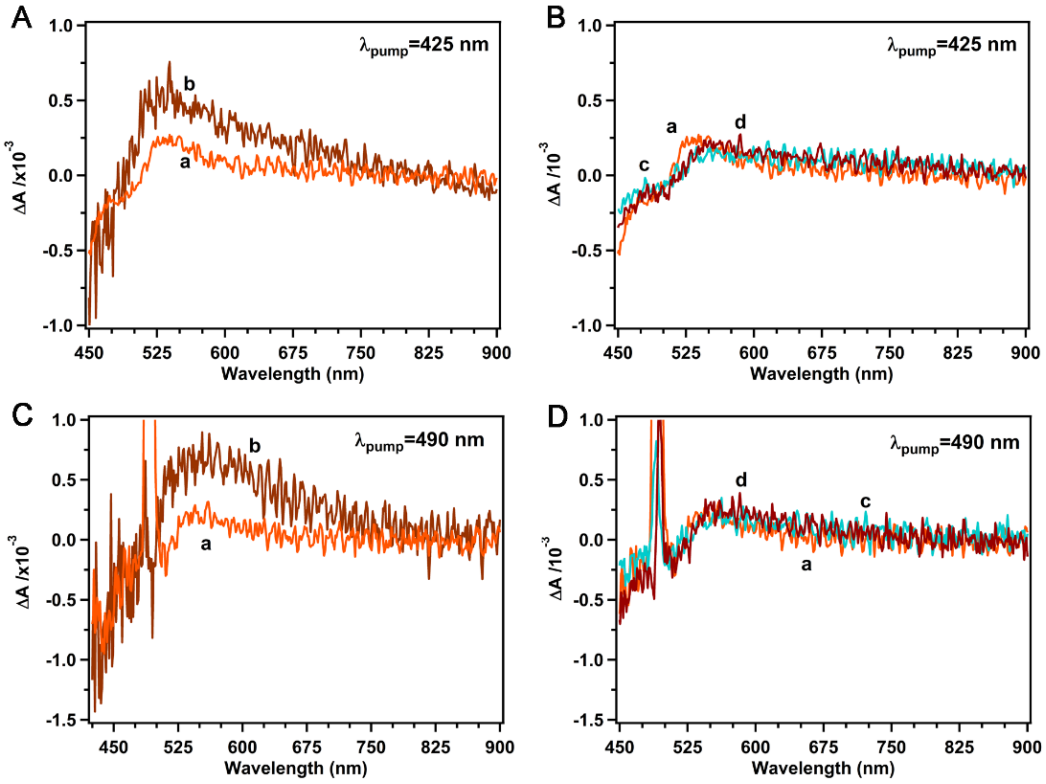

Figure A. 17 TA spectra of (a) V_2O_5 nanowires, (b) 5x SILAR CdSe/V_2O_5, (c) Cys-CdSe(sm)/ V_2O_5, and (d) Cys-CdSe(lg)/ β-V_2O_5. The pump wavelength is noted in each case.

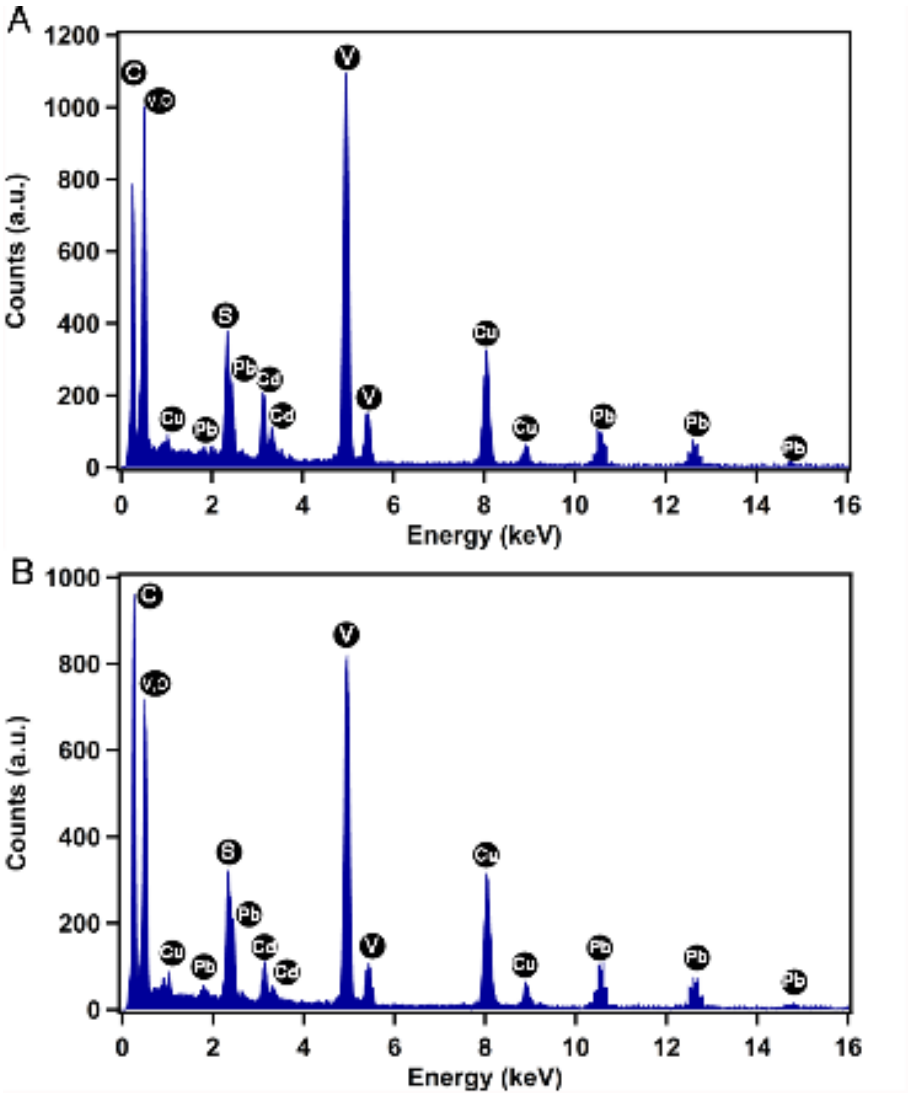

Figure A. 18 EDS spectra of A) Cys-CdS(lg)/β-$Pb_{0.33}V_2O_5$ and B) 3× SILAR CdS/β-$Pb_{0.33}V_2O_5$. Spectra were obtained on TEM sample grids, thus accounting for the presence of carbon and copper.

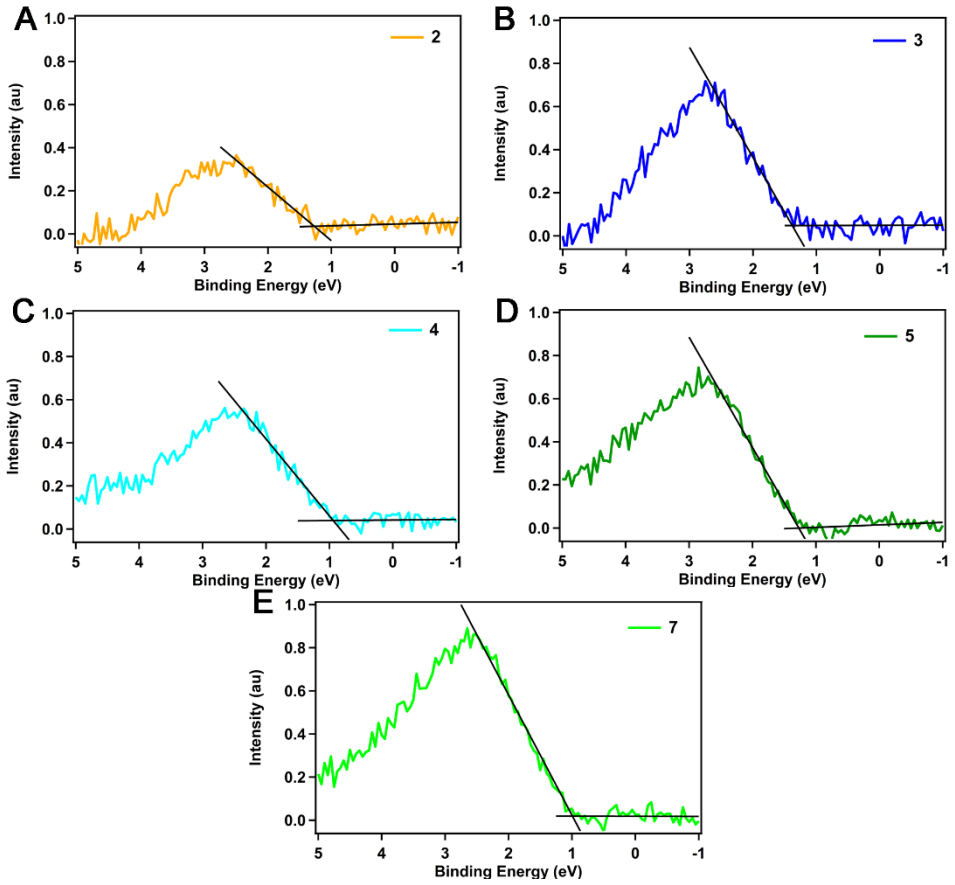

Figure A. 19 XPS difference spectra and fits for QD/β-$Pb_{0.33}V_2O_5$ heterostructures. Legend: 2. 1× SILAR CdS/β-$Pb_{0.33}V_2O_5$ 3. 3× SILAR CdS/β-$Pb_{0.33}V_2O_5$ 4. 3× SILAR CdSe/β-$Pb_{0.33}V_2O_5$ 5. Cys-CdS(lg)/β-$Pb_{0.33}V_2O_5$ 7. Cys-CdSe(lg)/β-$Pb_{0.33}V_2O_5$.

Table A. 1 Calculated elemental concentrations of β-$Pb_xV_2O_5$ nanowires with increasing number of SILAR cycles. All concentrations are expressed as ratios of atomic concentrations.

	One cycle	Two cycles	Three cycles	Four cycles	Five cycles
Cd:Se	0.59:1	0.89:1	0.60:1	0.78:1	0.68:1
Cd:Se:V	0.078:0.17:2	0.18:0.15:2	0.16:0.26:2	0.70:0.90:2	0.76:1.14:2

Table A. 2 Fitting parameters from global analysis of time-resolved emission decay data at all reaction times for free Cys-CdSe QDs (A), Cys-CdSe QDs combined with V_2O_5 nanowires (B), and Cys-CdSe QDs combined with β-$Pb_xV_2O_5$ nanowires (C).

A) Free Cys-CdSe QDs

Elapsed Time (min)	$\langle\tau\rangle_{ave}$ (ns)	τ_1 (ns)	f_1 (%)	τ_2 (ns)	f_2 (%)	τ_3 (ns)	f_3 (%)	χ^2
60	20.7	0.51±0.04	3.3	3.8±0.1	15.9	24.8±0.2	80.9	1.089
75	20.8	0.49±0.04	3.2	3.7±0.1	15.7	24.9±0.2	81.1	1.098
90	21.1	0.49±0.04	3.1	3.7±0.1	15.1	25.1±0.2	81.8	1.094
130	21.2	0.49±0.04	3.1	3.7±0.1	15.3	25.3±0.2	81.6	1.087
145	22.2	0.52±0.04	3.1	3.9±0.1	15.3	26.5±0.2	81.6	1.081
165	22.2	0.50±0.04	3.1	3.8±0.1	15.1	26.4±0.2	84.0	1.089
180	22.3	0.52±0.04	3.1	3.9±0.1	15.1	26.6±0.2	81.0	1.072
225	22.6	0.51±0.04	3.0	3.9±0.1	14.9	26.9±0.2	82.1	1.073
270	23.5	0.52±0.05	3.0	3.3±0.1	14.8	27.8±0.2	82.2	1.051
325	23.0	0.51±0.05	3.0	3.8±0.1	14.4	27.2±0.2	82.6	1.074

B) Cys-CdSe QDs combined with V_2O_5 nanowires

Elapsed Time (min)	$\langle\tau\rangle_{ave}$ (ns)	τ_1 (ns)	f_1 (%)	τ_2 (ns)	f_2 (%)	τ_3 (ns)	f_3 (%)	χ^2
60	19.6	0.48±0.04	3.8	3.6±0.1	16.3	23.8±0.2	80.0	1.087
75	21.3	0.51±0.04	3.2	3.8±0.1	15.5	25.5±0.2	81.3	1.073
90	19.6	0.48±0.04	3.8	3.6±0.1	16.2	23.7±0.2	80.1	1.081
130	19.5	0.47±0.04	3.7	3.5±0.1	16.0	23.5±0.2	80.3	1.083
145	19.8	0.48±0.04	3.8	3.6±0.1	16.2	24.0±0.2	80.0	1.077
165	19.2	0.46±0.04	3.9	3.5±0.1	15.2	23.3±0.2	80.0	1.075
180	19.5	0.48±0.04	4.0	3.5±0.1	16.4	23.8±0.2	80.0	1.071
225	19.1	0.47±0.04	4.0	3.5±0.1	16.6	23.3±0.2	79.3	1.067
270	18.1	0.46±0.04	4.3	3.3±0.1	16.8	22.2±0.2	78.9	1.007
325	16.0	0.46±0.04	5.0	3.2±0.1	19.1	20.2±0.3	75.8	1.018

C) Cys-CdSe QDs combined with β-$Pb_xV_2O_5$ nanowires

Elapsed Time (min)	$\langle\tau\rangle_{ave}$ (ns)	τ_1 (ns)	f_1 (%)	τ_2 (ns)	f_2 (%)	τ_3 (ns)	f_3 (%)	χ^2
60	16.6	0.48±0.04	4.4	3.4±0.1	18.2	20.7±0.2	77.4	1.083
75	16.5	0.47±0.04	4.4	3.3±0.1	18.4	20.6±0.2	77.2	1.088
90	16.8	0.48±0.04	4.4	3.4±0.1	18.4	20.9±0.2	77.2	1.086
130	16.8	0.46±0.04	4.5	3.4±0.1	18.5	21.0±0.2	76.9	1.085
145	16.6	0.47±0.04	4.6	3.3±0.1	18.3	20.8±0.2	77.2	1.093
165	16.8	0.48±0.04	4.7	3.4±0.1	18.3	21.0±0.2	77.0	1.067
180	16.8	0.48±0.04	4.6	3.4±0.1	18.7	21.1±0.2	76.7	1.049
225	16.6	0.48±0.04	4.5	3.3±0.1	18.7	20.8±0.2	76.7	1.066
270	16.6	0.47±0.04	4.6	3.3±0.1	18.6	20.8±0.2	76.8	1.010
325	16.0	0.45±0.04	4.8	3.2±0.1	18.4	20.0±0.2	76.8	1.025

Table A. 3 Kinetic fitting parameters and calculated average lifetimes for TA decay traces of β-$Pb_{0.33}V_2O_5$ and CdSe/β-$Pb_{0.33}V_2O_5$ at all pump wavelength (λ_{probe}=510 nm). The increase in excited-state lifetime with increasing excitation wavelength observed for β-$Pb_{0.33}V_2O_5$ can be attributed to a deceleration of the electron-hole recombination with the decreased initial excited-state population in β-$Pb_{0.33}V_2O_5$ nanowires consistent with the absorbances depicted in Figure V. 2A.

Sample	λ_{pump}	ΔA_0	A_1	τ_1 (μs)	A_2	τ_2 (μs)	A_3	τ_3 (μs)	$<\tau>$ (μs)	χ^2
β-$Pb_{0.33}V_2O_5$	360 nm	0.018± 0.003	0.19± 0.01	0.009± 0.001	0.43± 0.01	0.075± 0.005	0.38± 0.03	0.53± 0.03	0.23± 0.01	0.019 9
Cys-CdSe (sm)/ β-$Pb_{0.33}V_2O_5$	360 nm	0.028± 0.004	0.14± 0.01	0.034± 0.005	0.43± 0.04	0.41± 0.04	0.35± 0.04	1.8± 0.2	0.9± 0.1	0.120
Cys-CdSe (lg)/ β-$Pb_{0.33}V_2O_5$	360 nm	0.047± 0.005	0.29± 0.03	0.41± 0.05	0.083 ±0.01	0.01± 0.01	0.55± 0.03	2.3± 0.1	1.5± 0.1	0.136
3x SILAR CdSe/β-$Pb_{0.33}V_2O_5$	360 nm	0.055± 0.011	0.11± 0.05	0.023± 0.01	0.3± 0.04	0.14± 0.04	0.52± 0.03	1.1± 0.12	0.65± 0.07	0.317
1x SILAR CdSe/β-$Pb_{0.33}V_2O_5$	360 nm	0.047± 0.007	0.87± 0.02	0.018± 0.008	0.32± 0.03	0.16± 0.03	0.53± 0.03	1.05± 0.09	0.66± 0.09	0.163
β-$Pb_{0.33}V_2O_5$	425 nm	0.01± 0.002	0.19± 0.02	0.009± 0.002	0.41± 0.02	0.097± 0.009	0.4± 0.02	0.67± 0.04	0.34± 0.02	0.138
Cys-CdSe (sm)/ β-$Pb_{0.33}V_2O_5$	425 nm	0.02± 0.003	0.18± 0.01	0.018± 0.003	0.38± 0.02	0.21± 0.02	04.± 0.03	1.17± 0.08	0.57± 0.05	0.135
Cys-CdSe (lg)/ β-$Pb_{0.33}V_2O_5$	425 nm	0.018± 0.008	0.15± 0.02	0.015± 0.005	0.28± 0.05	0.6± 0.1	0.48± 0.05	4± 0.5	2.3± 0.4	1.10
3x SILAR CdSe/β-$Pb_{0.33}V_2O_5$	425 nm	0.0009 ±0.012	0.15± 0.04	0.009± 0.005	0.31± 0.06	0.13± 0.04	0.56± 0.07	0.78± 0.12	0.5± 0.1	0.844
1x SILAR CdSe/β-$Pb_{0.33}V_2O_5$	425 nm	0.014± 0.02	0.6± 0.64	0.004± 0.002	0.36± 0.07	0.23± 0.05	0.46± 0.06	1.39± 0.36	0.5± 0.3	0.700
β-$Pb_{0.33}V_2O_5$	490 nm	0.17± 0.02	0.033 ± 0.007	0.52± 0.05	0.52± 0.05	0.337± 0.05	0.3± 0.05	1.8± 0.3	0.9± 0.2	0.186
Cys-CdSe (sm)/ β-$Pb_{0.33}V_2O_5$	490 nm	0.017± 0.006	0.14± 0.01	0.033± 0.007	0.45± 0.06	0.53± 0.08	0.34± 0.07	2.3± 0.4	0.95± 0.05	0.209
Cys-CdSe (lg)/ β-$Pb_{0.33}V_2O_5$	490 nm	0.06± 0.008	0.12± 0.02	0.15± 0.04	0.7± 0.02	2.6± 0.1	X	X	2.2± 0.1	0.489
3x SILAR CdSe/β-$Pb_{0.33}V_2O_5$	490 nm	-0.007 ±0.03	0.13± 0.04	0.027± 0.015	0.33± 0.07	0.23± 0.09	0.51± 0.07	1.44± 0.39	0.8± 0.3	0.399
1x SILAR CdSe/β-$Pb_{0.33}V_2O_5$	490 nm	-0.05 2±0.04	0.15± 0.06	0.17± 0.10	0.73± 0.05	1.54± 0.31	X	X	1.3± 0.3	0.999
β-$Pb_{0.33}V_2O_5$	600 nm	0.016± 0.008	0.18± 0.04	0.04± 0.02	0.56± 0.06	0.35± 0.08	0.13± 0.07	2± 1	0.6± 0.3	0.646
Cys-CdSe (lg)/ β-$Pb_{0.33}V_2O_5$	600 nm	0.06± 0.2	0.5± 0.1	1.5± 0.3	0.4± 0.1	6± 2	X	X	3± 2	0.416
3x SILAR CdSe/β-$Pb_{0.33}V_2O_5$	600 nm	0.05± 0.02	0.15± 0.05	0.067± 0.046	0.71± 0.05	0.73± 0.09	X	X	0.7± 0.3	1.21
1x SILAR CdSe/β-$Pb_{0.33}V_2O_5$	600 nm	0.068± 0.036	0.77± 0.67	0.005± 0.002	0.67± 0.03	1.44± 0.19	X	X	0.6± 0.1	2.09

Table A. 4 Kinetic fitting parameters and calculated average lifetimes for TA decay traces of β-$Pb_{0.33}V_2O_5$ and CdSe/β-$Pb_{0.33}V_2O_5$ at all pump wavelengths (λ_{probe}= 750 nm).

Sample	λ_{pump}	ΔA_0	A_1	τ_1 (μs)	A_2	τ_2 (μs)	$<\tau>$ (μs)	χ^2
β-$Pb_{0.33}V_2O_5$	360 nm	0.05±0.01	0.3±0.03	0.12±0.02	0.54±0.03	0.88±0.07	0.59±0.07	0.152
Cys-CdSe (sm)/ β-$Pb_{0.33}V_2O_5$	360 nm	0.03±0.03	0.5±0.2	1.3±0.3	0.3±0.1	5±2	3±1	0.339
Cys-CdSe (lg)/ β-$Pb_{0.33}V_2O_5$	360 nm	0.08±0.02	0.2±0.1	0.9±0.5	0.7±0.1	3.7±0.7	3±1	0.250
3x SILAR CdSe/β-$Pb_{0.33}V_2O_5$	360 nm	0.003± 0.007	0.42±0.053	1.4±0.18	0.48±0.05	6.8±0.8	2.8±0.4	0.341
1x SILAR CdSe/β-$Pb_{0.33}V_2O_5$	360 nm	-0.008 ±0.005	0.48±0.05	0.94±0.10	0.47±0.05	4.6±0.5	4.3±0.7	0.429
β-$Pb_{0.33}V_2O_5$	425 nm	0.029± 0.007	0.3±0.5	0.23±0.04	0.52±0.05	1.4±0.2	0.9±0.6	0.875
Cys-CdSe (sm)/ β-$Pb_{0.33}V_2O_5$	425 nm	0.033± 0.007	0.27±0.03	0.26±0.04	0.56±0.03	2±0.2	1.5±0.2	0.637
Cys-CdSe (lg)/ β-$Pb_{0.33}V_2O_5$	425 nm	0.06±0.04	0.1±0.1	0.9±0.7	0.6±0.1	4±2	4±2	1.04
3x SILAR CdSe/β-$Pb_{0.33}V_2O_5$	425 nm	-0.016 ±0.008	0.3±0.04	0.57±0.12	0.57±0.04	4.3±0.44	3±0.4	1.07
1x SILAR CdSe/β-$Pb_{0.33}V_2O_5$	425 nm	-0.06±0.03	0.45±0.07	1.1±0.2	0.46±0.06	6.8±1.8	4±1	0.785
β-$Pb_{0.33}V_2O_5$	490 nm	0.02±0.02	0.4±0.2	0.5±0.2	0.3±0.2	2±1	1±1	1.52
Cys-CdSe (sm)/ β-$Pb_{0.33}V_2O_5$	490 nm	0.06±0.01	0.16±0.03	0.021±0.008	0.7±0.02	1.7±0.1	1.4±0.1	1.42
Cys-CdSe (lg)/ β-$Pb_{0.33}V_2O_5$	490 nm	0.08±0.01	0.15±0.04	0.015±0.006	0.71±0.01	3.1±0.2	2.6±0.2	0.993
3x SILAR CdSe/β-$Pb_{0.33}V_2O_5$	490 nm	0.03±0.02	0.15±0.05	0.16±0.011	0.71±0.03	3±0.3	2.5±0.3	1.64
1x SILAR CdSe/β-$Pb_{0.33}V_2O_5$	490 nm	0.08±0.02	0.12±0.35	0.067±0.14	0.7±0.02	2.4±0.2	2.1±0.9	1.27
β-$Pb_{0.33}V_2O_5$	600 nm	0.05±0.03	0.24±0.07	0.1±0.07	0.6±0.07	1±0.2	0.7±0.2	1.84
Cys-CdSe (lg)/ β-$Pb_{0.33}V_2O_5$	600 nm	0.07±0.01	0.08±0.02	0.2±0.2	0.69±0.02	3.7±0.3	3.4±0.3	0.885
3x SILAR CdSe/β-$Pb_{0.33}V_2O_5$	600 nm	0.003±0.02	0.44±0.08	0.87±0.19	0.44±0.07	5.5±1.5	4±2	0.792
1x SILAR CdSe/β-$Pb_{0.33}V_2O_5$	600 nm	-0.004±0.03	0.38±0.15	1.4±0.4	0.5±0.12	6.6±2.5	3±1	0.891

Table A. 5 Kinetic fitting parameters and calculated average lifetimes for TA decay traces of V_2O_5 and CdSe/V_2O_5 at all pump and probe wavelengths.

Sample	λ_{pump}	λ_{probe}	ΔA_0	A_1	τ_1 (μs)	A_2	τ_2 (μs)	$<\tau>$ (μs)	χ^2
V_2O_5	360 nm	535 nm	-0.05 ±0.01	0.2±0.1	0.02±0.01	0.8±0.1	0.09±0.01	0.07±0.02	0.628
Cys-CdSe (sm)/ V_2O_5	360 nm	535 nm	0.003 ±0.02	0.3±0.3	0.04±0.03	0.7±0.03	0.14±0.05	0.11±0.07	1.14
Cys-CdSe (lg)/ V_2O_5	360 nm	535 nm	-0.07 ±0.01	0.34±0.05	0.02±0.007	0.72±0.06	0.2±0.02	0.14±0.02	0.525
5x SILAR CdSe/V_2O_5	360 nm	535 nm	0.06 ±0.01	0.26±0.03	0.03±0.007	0.65±0.03	0.31±0.03	0.23±0.03	0.296
Cys-CdSe (sm)/ V_2O_5	360 nm	700 nm	0.06 ±0.02	0.6±0.3	0.02±0.01	0.62±0.07	0.33±0.07	0.17±0.06	1.54
Cys-CdSe (lg)/ V_2O_5	360 nm	700 nm	-0.05 ±0.02	0.19±0.08	0.03±0.03	0.69±0.08	0.33±0.06	0.27±.07	1.49
5x SILAR CdSe/V_2O_5	360 nm	700 nm	-0.007 ±0.08	0.36±0.18	0.26±0.12	0.46±0.13	1.65±1.22	1.0±0.8	1.29
V_2O_5	360 nm	430 nm	-0.02 ±0.01	-0.33±0.03	0.03±0.01	-0.46±0.03	0.48±0.07	0.29±0.05	0.656
Cys-CdSe (sm)/ V_2O_5	360 nm	430 nm	-0.02 ±0.01	-0.35±0.05	0.007±0.002	-0.43±0.03	0.36±0.06	0.2±0.04	1.69
Cys-CdSe (lg)/ V_2O_5	360 nm	430 nm	-0.06 ±0.02	-0.27±0.03	0.021±0.005	-0.52±0.02	0.65±0.08	0.43±0.06	0.837
5x SILAR CdSe/V_2O_5	360 nm	430 nm	-0.09 ±0.02	-0.23±0.06	0.07±0.03	-0.47±0.06	0.61±0.14	0.43±0.07	1.04
V_2O_5	425 nm	535 nm	-0.02 ±0.02	0.5±2	0.014±0.009	0.7±0.1	0.09±0.02	0.06±0.02	2.19
Cys-CdSe (sm)/ V_2O_5	425 nm	535 nm	-0.05 ±0.03	0.6±4	0.004±0.01	0.6±0.05	0.1±0.03	0.1±0.2	5.05
Cys-CdSe (lg)/ V_2O_5	425 nm	535 nm	-0.15 ±0.04	3±5	0.003±0.02	0.78±0.04	0.19±0.03	0.04±0.05	4.86
5x SILAR CdSe/V_2O_5	425 nm	535 nm	-0.02 ±0.03	0.19±0.10	0.04±0.04	0.61±0.10	0.31±0.09	0.25±0.09	4.28
V_2O_5	490 nm	535 nm	0.04 ±0.02	0.9±0.2	0.07±0.02	0.73±0.07	0.2±0.4	0.07±1472	4.68
Cys-CdSe (sm)/ V_2O_5	490 nm	535 nm	0.09 ±0.03	0.4±2	0.009±0.01	0.73±0.04	0.2±0.4	0.1±0.7	4.34
Cys-CdSe (lg)/ V_2O_5	490 nm	535 nm	-0.09 ±0.03	10±46	0.07±0.2	0.4±2	0.26±0.05	0.03±0.1	3.29
5x SILAR CdSe/V_2O_5	490 nm	535 nm	0.08 ±0.02	0.24±0.03	0.03±0.009	0.63±0.03	0.41±0.05	0.3±0.04	0.818